

AD-A078 590

WISCONSIN UNIV-MADISON DEPT OF METEOROLOGY

LIDAR MEASUREMENT OF BOUNDARY LAYER WINDS AND CONVECTIVE STRUCT--ETC(U)

AUG 79 E W ELORANTA

DAA629-76-G-0156

F/6 4/2

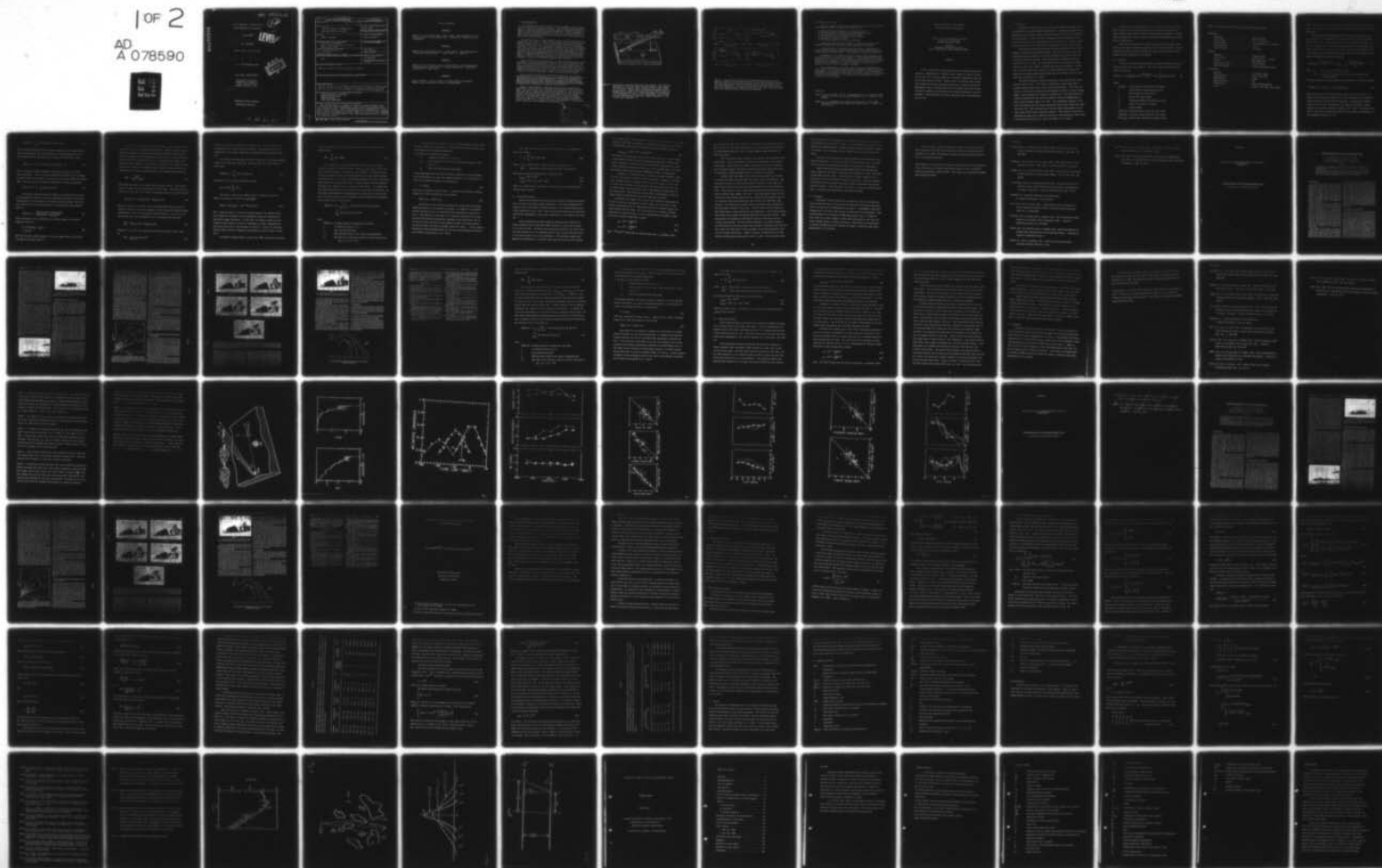
NL

ARO-13535.2-65

UNCLASSIFIED

1 OF 2

AD
A 078590



ADA 078590

18 ARO 13535.2-AS

19
12

6 LIDAR MEASUREMENT OF BOUNDARY LAYER
WINDS AND CONVECTIVE STRUCTURE.

9 FINAL REPORT
1 Mar 76 - 30 Jun 79

LEVEL

10 Edwin E. W. ELORANTA

March 1, 1976 - June 30, 1979

11 20 Aug 79 12 172

U. S. ARMY RESEARCH OFFICE

DDC
RAPID
DEC 27 1979
RESERVED
E

Grant Number DAA29-76-0156

University of Wisconsin
Department of Meteorology
1225 W. Dayton Street
Madison, Wisconsin 53706

15 ✓ DAA29-76-0156

APPROVED FOR PUBLIC RELEASE;

DISTRIBUTION UNLIMITED.

380160
79 12 27 228

SECURITY CLASSIFICATION OF THIS PAGE (When Data Entered)

REPORT DOCUMENTATION PAGE		READ INSTRUCTIONS BEFORE COMPLETING FORM
1. REPORT NUMBER	2. GOVT ACCESSION NO.	3. RECIPIENT'S CATALOG NUMBER
4. TITLE (and Subtitle) LIDAR MEASUREMENT OF BOUNDARY LAYER WINDS AND CONVECTIVE STRUCTURE		5. TYPE OF REPORT & PERIOD COVERED Final Report March 1, 1976 - June 30, 1979
7. AUTHOR(s) EDWIN W. ELORANTA		6. PERFORMING ORG. REPORT NUMBER
9. PERFORMING ORGANIZATION NAME AND ADDRESS University of Wisconsin Dept. of Meteorology, 1225 W. Dayton St. Madison, Wis. 53706		8. CONTRACT OR GRANT NUMBER(s) DAA29-76-G0156 ^{NEW}
11. CONTROLLING OFFICE NAME AND ADDRESS U. S. Army Research Office P. O. Box 12211 Research Triangle Park, NC 27709		10. PROGRAM ELEMENT, PROJECT, TASK AREA & WORK UNIT NUMBERS
14. MONITORING AGENCY NAME & ADDRESS (if different from Controlling Office) Same		12. REPORT DATE Aug. 20, 1979
		13. NUMBER OF PAGES
		15. SECURITY CLASS. (of this report) Unclassified Unclassified
		15a. DECLASSIFICATION/DOWNGRADING SCHEDULE
16. DISTRIBUTION STATEMENT (of this Report) Approved for public release; distribution unlimited.		
17. DISTRIBUTION STATEMENT (of the abstract entered in Block 20, if different from Report)		
18. SUPPLEMENTARY NOTES The view, opinions, and/or findings contained in this report are those of the author(s) and should not be construed as an official Department of the Army position, policy, or decision, unless so designated by other documentation.		
19. KEY WORDS (Continue on reverse side if necessary and identify by block number) PLANETARY BOUNDARY LAYER WINDS REMOTE SENSING OF WINDS CONVECTIVE PLUMES LIDAR WIND MEASUREMENTS		
20. ABSTRACT (Continue on reverse side if necessary and identify by block number) The following report is a summary of studies on planetary boundary layer visualization and remote determination of wind profiles and turbulence quantities by means of a lidar. These investigations rely on inhomogeneities in the natural aerosol distribution to delineate eddies in the boundary layer. Measurement of the rate of displacement of these eddies yield horizontal wind components. Observations of the daytime growth of the convective boundary layer are compared to a theoretical model.		

DD FORM 1 JAN 73 1473 EDITION OF 1 NOV 65 IS OBSOLETE

Unclassified

SECURITY CLASSIFICATION OF THIS PAGE (When Data Entered)

LIST OF APPENDIXES

APPENDIX A

Sroga, J.T., E.W. Eloranta and T. Barber (1979). Lidar Measurement of Wind Velocity Profiles in the Boundary Layer. (Submitted to Journal of Applied Meteorology.)

APPENDIX B

Kunkel, K.E., E.W. Eloranta and S.T. Shipley (1977). Lidar Observations of the Convective Boundary Layer. J. Appl. Meteor. 12, 1306-1311.

APPENDIX C

Kunkel, K.E., E.W. Eloranta and J.A. Weinman (1979). Remote Determination of Boundary Layer Characteristics from Lidar Measurements. (Accepted for publication by J. Atmos. Sci.)

APPENDIX D

Boers, R. (1979). The use of Lidar in Testing Inversion Rise Models. Masters Thesis, University of Utrecht, the Netherlands.

Lidar signals backscattered from the planetary boundary layer are dominated by scattering from aerosol particles. The naturally occurring aerosol content of the lower atmosphere fluctuates under the continuous influence of particle sources and particle deposition mechanisms. These fluctuations in aerosol content are easily detected with lidar. By observing the drift of these spatial inhomogeneities in aerosol content, lidar can be used to determine wind velocities remotely.

Along with profiles of the mean wind, the three angle azimuth scan, shown in Figure 1, allows a measurement of turbulent velocity fluctuations in the wind. Wind fluctuations which take place on a time scale shorter than the averaging time used for the lidar wind profile measurement make the cross correlations determined from the outside angles of the scan smaller than those computed from the adjacent angles. Appendix A describes how this effect can be used to estimate the amplitude of small scale velocity fluctuations.

Figure 2, which presents a comparison between lidar and balloon wind measurements, illustrates one of the important advantages of the lidar technique. The lidar results allow consistent measurement of both the vertical wind shear and the temporal variation of mean wind speed. Gust induced fluctuations make similar measurements extremely difficult with the balloon soundings. The smoothness of the lidar profiles is a result of averaging over a time interval of 5 minutes and over a volume extending 50 meters in altitude and 480 meters in length (the cross path dimension of the averaging volume varies with range between ~20 and 200 meters).

Approved For	_____
File Class	_____
DOC TAB	_____
Unannounced	_____
Justification	_____
By	_____
Dist. Inquiries	_____
Availability Codes	_____
Available/for Special	_____
Dist	_____

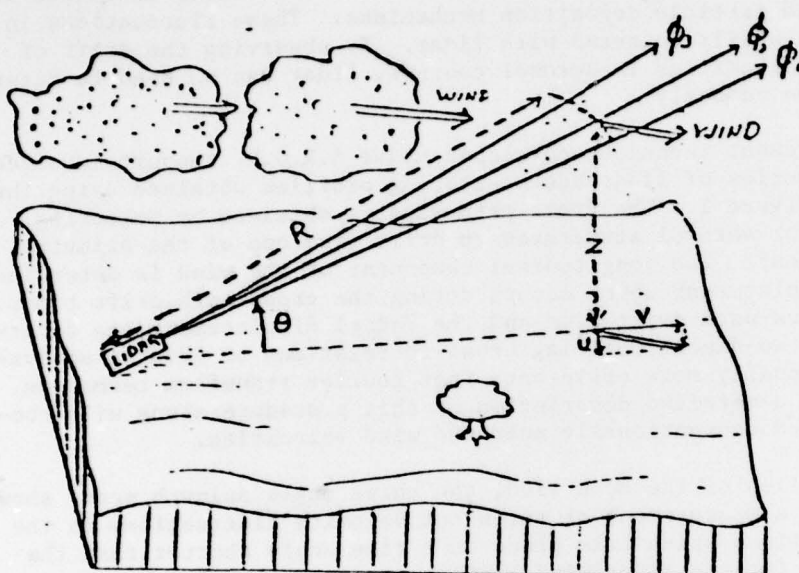


Figure 1. The geometry used for lidar wind measurements. The lidar is operated at a constant small elevation angle θ and scanned back and forth between three closely spaced azimuth angles ϕ_1 , ϕ_2 and ϕ_3 . Range resolved profiles of backscattered intensity are recorded at ~ 1 second intervals for a period of 2 to 5 minutes to produce a wind measurement. Wind velocities are calculated in terms of a radial component, v , and a cross path component, u .

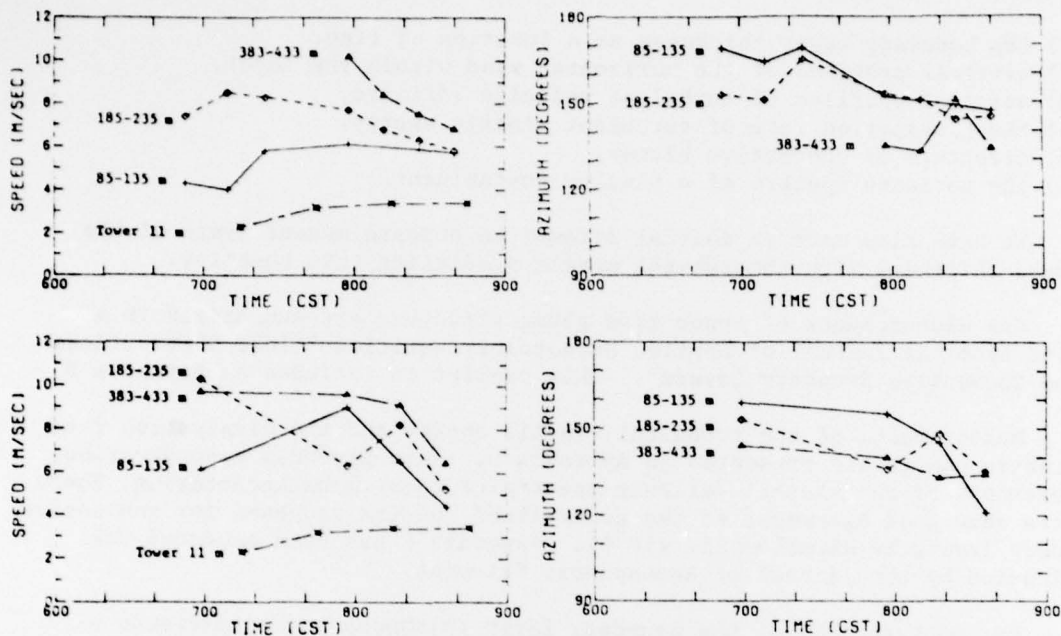


Figure 2. Time histories of wind speed and direction measured with lidar and pilot balloons. Measurements are from June 23, 1978 at Argonne, Illinois. The pilot balloon winds have been averaged over the same vertical interval as the lidar measurements. Notice that because the lidar observations are the result of averaging over ~ 5 minutes and 480 meters in range, lidar wind speeds show more consistent behavior than the pilot balloons.

B. Boundary Layer Studies

During the course of this study Lidar has been used to make the following measurements within the convective boundary layer.

- 1) the boundary layer thickness as a function of time,
- 2) vertical profiles of the horizontal wind within the layer,
- 3) vertical profiles of turbulent velocity variance,
- 4) the dissipation rate of turbulent kinetic energy,
- 5) structure of convective plumes,
- 6) the variance spectra of a passive contaminant.

We have also made an initial attempt to compare measurements of the boundary thickness with theoretical models predicting this quantity.

Our measurements of convective plume structure are summarized in a reprint from the Journal of Applied Meteorology entitled "Lidar Observations of the Convective Boundary Layers". This reprint is included as Appendix B.

Measurements of the turbulent kinetic energy and the dissipation rate of kinetic energy are presented in Appendix C. This appendix also describes measurements of the spatial variance spectra of aerosol backscattering. These spectra show good agreement to the generalized spectra proposed for convective boundary layers by Kaimal et al. (1976). Appendix C has been accepted for publication by the Journal of Atmospheric Sciences.

Our measurements of the boundary layer thickness and comparisons of these values to the model developed by Zeman and Tennekes (1977) are presented in Appendix D. This appendix titled "The use of Lidar in Testing Inversion Rise Models" was presented by Rienout Boers as masters thesis to the University of Utrecht, the Netherlands. It is shown that lidar measurements provide a critical test for such models.

References:

- Zeman, O., and H. Tennekes, (1977). Parameterization of the turbulent energy budget at the top of the convective boundary layer. J. Atmos. Sc. 34, 111-123.
- Kaimal, J.C., J.C. Wyngaard, D.A. Haugen, O.R. Cote, and Y. Isumi (1976). Turbulence Structure in the Convective Boundary Layer. J. Atmos. Sci. 33, 7152-2169.

Lidar Measurement of Wind Velocity
Profiles in the Boundary Layer

Jeffery T. Sroga and Edwin W. Eloranta
University of Wisconsin
Madison, Wisconsin 53706

Ted Barber
Atmospheric Sciences Laboratory
White Sands Missile Range, New Mexico 88002

ABSTRACT

A lidar technique for measuring wind in the atmospheric boundary is presented. Inhomogeneties in ambient aerosol content are used as tracers of the wind. This technique yields both horizontal components of the wind and the wind velocity variance. These results are achieved using a model which assumes an isotropic gaussian distribution of turbulent velocities. Experimental results comparing lidar wind measurements with winds derived from radar tracked pilot balloons and tower mounted anemometers show good agreement. Wind measurements have been obtained at slant range distances up to 6.5 km.

1. Introduction

Knowledge of the wind structure in the earth's planetary boundary layer is essential for many meteorological applications. Aviation, air pollution and boundary layer meteorology require spatial and temporal resolution in wind velocity measurements. Remote sounding techniques offer the possibility of measuring wind velocities in large volumes of the atmosphere on a continuous basis. These measurements are not influenced by the physical presence of the sensor.

Lidar signals backscattered from the planetary boundary layer are dominated by scattering from aerosol particles. The aerosol content of the lower atmosphere fluctuates under the continuous influence of particle sources and particle deposition mechanisms. These fluctuations in aerosol content are easily detected with lidar. By observing the drift of these spatial inhomogeneities, lidar can be used to determine wind velocities remotely. Correlation techniques using lidar profiles of aerosol backscatter intensity have been used to remotely measure winds by Derr and Little (1970), Eloranta et al. (1975) and Armstrong et al. (1976).

The wind measurement technique described in this study uses the lidar geometry shown in Fig. 1. The lidar is elevated by a small angle and is rapidly scanned between three closely spaced azimuth angles. Lidar data consists of a time series of lidar profiles obtained at each of the three azimuth angles. The horizontal wind component perpendicular to the lidar beam is obtained by measuring the time interval needed for aerosol inhomogeneities to drift from one azimuth angle to the next. The longitudinal component of the wind is determined from the radial displacement which occurs during this cross path drift time. The cross path drift time and radial displacement are measured using a Fast Fourier Transform technique. This method is equivalent to measuring the space time correlation function of lidar profiles to infer winds as was done by Eloranta et al. (1975) and Kunkel et al. (1979).

Because of spatial and temporal fluctuations in velocity, the maximum value of the aerosol correlation function between profiles obtained at different azimuth angles decreases with increasing angular separation. A simple model describing this effect is used to measure the magnitude of the turbulent velocity fluctuations.

Lidar wind measurements are derived from the drift of aerosol inhomogeneities with spatial dimensions ranging between ~15 and 500 meters. Typical measurements involve spatial averaging over range intervals of 250 to 1000 meters and time averages of 2 to 5 minutes.

II. Procedure

Profiles of aerosol backscattering are obtained with the University of Wisconsin lidar system (see Table 1). The return power measured with this system is given by:

$$P(\phi, R, t_n) = E_n \frac{c}{2} \frac{A_r}{R^2} \beta_s(\phi, R, t_n) \frac{IP'(\phi, R, t_n)}{4\pi} \exp[-2 \int_0^R \beta_e(\phi, R', t_n) dR'] \quad (1)$$

where:

$P(\phi, R, t_n)$	instantaneous received power from Range R
R	radial distance along propagation path
ϕ	azimuth angle of lidar profile
t_n	time of n^{th} lidar profile
E_n	transmitted energy of the n^{th} laser pulse
A_r	area of the receiver telescope
c	speed of light
$\beta_s(\phi, R, t_n)$	scattering cross section per unit volume
$\beta_e(\phi, R, t_n)$	extinction cross section per unit volume
$IP'(\phi, R, t_n)$	aerosol phase function for backscattering

Table 1. University of Wisconsin Lidar System Parameters (1978)

Transmitter

Wavelength	694.3nm (ruby)
Output Energy	1.0 - 1.5 J/pulse
Pulse Duration	20ns (Pockels cell Q-switched)
Beam Divergence	1 mrad
Repetition Rate	1 Hz (max)

Receiver

Telescope31m Newtonian
Field of View	Adjustable (1.5 - 7 mrad)
Detector	RCA C70042K PMT
Quantum Efficiency	6.8% @ 694.3nm
Spectral Bandpass	1.0nm (Interference filter)

Data Logging

Amplifier	Logarithmic (80db)
A/D Conversion	10 bit resolution
Sampling Rate	10 MHz
Range Resolution	15m
Preprocessing	PDP 11/40 Minicomputer
Output	Magnetic Tape, Real time display

This lidar return signal is logarithmically amplified to compress the dynamic range and digitized into 10 bit words at a 10 MHz rate, yielding a 15 m range resolution.

The sequential three angle azimuth scan shown in Fig. 1 ($\phi = \phi_1, \phi_2, \phi_3, \phi_2, \phi_1, \phi_2, \dots$) yields three separate time series of lidar profiles, $P(\phi, R_\ell, t_n)$. Time varying inhomogeneities are separated from the mean structure by removing a time centered running mean profile at each azimuth angle. These profiles are corrected for the inverse range squared dependence of the lidar equation and normalized by the transmitted laser pulse energy to yield aerosol inhomogeneity profiles, $Y(\phi, R_\ell, t_n)$:

$$Y(\phi, R_\ell, t_n) = \left[\frac{R_\ell^2 P(\phi, R_\ell, t_n)}{E_n} \right] - \frac{1}{2m+1} \sum_{i=-m}^m \left[\frac{R_\ell^2 P(\phi, R_\ell, t_{n+i})}{E_{n+i}} \right] \quad (2)$$

where: R_ℓ the range to the ℓ^{th} data point

$2m+1$ number of lidar profiles used in calculating the mean aerosol structure

The range averaged mean value within each data segment is removed as follows:

$$Y'(\phi, R_\ell, t_n) = Y(\phi, R_\ell, t_n) - \frac{1}{N} \sum_{i=a}^b Y(\phi, R_i, t_n) \quad (3)$$

where the data segment extends from data point $\ell = a$ to $\ell = b$ and $N = b - a$.

These aerosol inhomogeneity profiles are then transformed into spatial wave number space using the Fast Fourier Transform. A cosine taper on 10% of each end of the aerosol inhomogeneity data segment is applied to reduce leakage in the spectral estimates (Bingham et al., 1967). The Fourier transform of the aerosol inhomogeneity profile from the spatial coordinate R_ℓ to the wavenumber coordinate, k , is:

$$F(\phi, k, t_n) = \sum_{\ell=a}^b Y'(\phi, R_\ell, t_n) \exp(-2\pi i \sqrt{-1} k R_\ell) \quad (4)$$

These transformed profiles are then used to compute raw cross spectral estimates between profiles for all combinations of angles (ϕ_i, ϕ_j) and for all time separations (Δt) corresponding to possible cross path drift times:

$$S(\phi_i, \phi_j, k, t_n, \Delta t) = F^*(\phi_i, k, t_n) F(\phi_j, k, t_n + \Delta t) \quad (5)$$

where $*$ denotes the complex conjugate and $S(\phi_i, \phi_j, k, t_n, \Delta t)$ is the cross spectral estimate. Smooth spectral estimates are obtained by time averaging the spatial spectral estimates to increase the statistical significance (Welsh, 1967). The cross spectral estimate averaged over J profiles is given by:

$$\bar{S}(\phi_i, \phi_j, k, \Delta t) = \frac{1}{J} \sum_{n=1}^J S(\phi_i, \phi_j, k, t_n, \Delta t) \quad (6)$$

The coherence which measures the degree of correlation as a function of the spatial wave number, k , is used to determine the time for the aerosol inhomogeneities to drift between the different azimuthal angles. The coherence calculated from the smoothed spectral estimates (Otness and Enochson, 1972) is:

$$\text{coh}(k, \Delta x, \Delta t) = \frac{\bar{S}^*(\phi_i, \phi_j, k, \Delta t) \bar{S}(\phi_i, \phi_j, k, \Delta t)}{\bar{S}(\phi_i, \phi_i, k, 0) \bar{S}(\phi_j, \phi_j, k, 0)} \quad (7)$$

where the average lateral separation, Δx , and mean height, Z , of a data segment are given by:

$$\begin{aligned} \Delta x &= 2 \bar{R} \sin[(\phi_i - \phi_j)/2] \\ Z &= \bar{R} \sin \theta \end{aligned} \quad (8)$$

where \bar{R} is the mean radial distance of the data segment and θ is the elevation angle of the lidar (Fig. 1).

Because of noise in lidar measurements, each spectral component does not contain the same information on wind motion. Spatial filtering of lidar profiles is required to enhance the signal characteristics of the aerosol density inhomogeneities over the background noise level. A filter which suppresses noise while minimizing the error in reproducing this signal can be calculated from knowledge of the spectral characteristics of signal and noise contributions (Wainstein and Zubakov, 1962). When the signal and noise are uncorrelated, the Fourier transform, $H(k)$, of the optimal linear filter is:

$$H(k) = \frac{\tilde{S}_S(k)}{\tilde{S}_S(k) + \tilde{S}_N(k)} \quad (9)$$

where $\tilde{S}_S(k)$ and $\tilde{S}_N(k)$ are the signal and noise power spectra. This optimal transfer function can be estimated from the lidar data. Lidar power spectral estimates are the sum of the aerosol inhomogeneity spectrum and noise spectrum:

$$\tilde{S}(\phi_i, \phi_i, k, 0) = \tilde{S}_S(\phi_i, \phi_i, k, 0) + \tilde{S}_N(\phi_i, \phi_i, k, 0) \quad (10)$$

Because the noise in one profile is not correlated with the noise in other profiles, smooth cross spectral estimates of lidar measurements suppress noise contributions. For the cross spectral estimates with $\phi_i = \phi_j$, (i.e. $\Delta x = 0$) the limiting value as Δt approaches zero is the signal power spectrum:

$$\lim_{\Delta t \rightarrow 0} \tilde{S}(\phi_i, \phi_i, k, \Delta t) = \tilde{S}_S(\phi_i, \phi_i, k, 0) \quad (11)$$

Using Eqs. 7, 9 and 11, the transfer function of the optimal linear filter is:

$$H(k) = [\lim_{\Delta t \rightarrow 0} \text{coh}(k, 0, \Delta t)]^{1/2} \quad (12)$$

In order to extrapolate coherence measurements to $\Delta t = 0$, the coherence decrease with time is approximated by a Gaussian. This extrapolation is performed with a least squares regression to a Gaussian for each spectral component.

The transfer function, $H(K)$, provides a method for calculating a weighted average of the coherence, $\overline{\text{coh}}(\Delta x, \Delta t)$, which optimizes the overall signal to noise ratio:

$$\overline{\text{coh}}(\Delta x, \Delta t) = \frac{\sum_{k=k_1}^{k_m} W(k) \text{coh}(k, \Delta x, \Delta t)}{\sum_{k=k_1}^{k_m} W(k)} \quad (13)$$

where $w(k)$ is the normalized weighting function:

$$W(k) = H^2(k) / \sum_{k=k_1}^{k_m} H^2(k) \quad (14)$$

The signal to noise ratio, $\text{SNR}(k)$, can be estimated for each wave number by solving Eqs. 9 and 12 for $\tilde{S}_S(k)/\tilde{S}_N(k)$:

$$\text{SNR}(k) = \tilde{S}_S(k)/\tilde{S}_N(k) = [\text{coh}^{-1/2}(k, 0, 0) - 1]^{-1} \quad (15)$$

Fig. 2 shows the signal to noise ratio and the square of the optimal filter as a function of wavenumber for data obtained on January 19, 1978 at White Sand Missile Range, New Mexico. In this case, the signal to noise ratio decreases by approximately two orders of magnitude as aerosol inhomogeneities vary from a scale size of one kilometer to 30 meters. Clearly the weighting function, $W(k)$, provides a substantial improvement in overall signal to noise ratio.

A wavenumber averaged signal to noise ratio, $\overline{\text{SNR}}$, can be used to provide

an objective criteria for rejecting wind determinations derived from noise dominated data.

$$\overline{\text{SNR}} = \sum_{k=k_1}^{k_m} W(k) \text{SNR}(k) \quad (16)$$

If the wind were constant in space and time, the mean cross path velocity, \bar{u} , could be determined from $\bar{u} = \Delta x / \Delta t_{\text{max}}$: where Δt_{max} is the time lag at which the weighted coherence, Eq. 13, is largest. In practice, wind velocity fluctuations cause the coherence maximum to decrease with increases in either Δx or Δt . As a result, the coherence maximum occurs at a time delay shorter than the cross path drift time. A model similar to the one employed by Kunkel et al. (1979) is used to correct for this effect. It assumes that the spatial distribution of the aerosol density is Gaussian and isotropic, and that these three-dimensional inhomogeneities are advected by a mean velocity plus a turbulent velocity with an isotropic Gaussian probability distribution. The functional form of this model is:

$$\overline{\text{coh}}(\Delta x, \Delta t) = A \left[\frac{2 \sigma_a^2}{2 \sigma_a^2 + \sigma_s^2 \Delta t} \right] \exp[-(\Delta x - \bar{u} \Delta t)^2 / (2 \sigma_a^2 + \sigma_s^2 \Delta t^2)] \cdot \sum_{k=k_1}^{k_m} W(k) \exp(-4\pi^2 k^2 \sigma_s^2 \Delta t^2) \quad (17)$$

where

$\overline{\text{coh}}(\Delta x, \Delta t)$ weighted coherence averaged over wavenumber

A an amplitude factor ($A \leq 1$)

\bar{u} mean lateral wind speed

σ_a RMS horizontal width of the aerosol inhomogeneities

σ_s RMS width of the isotropic Gaussian velocity distribution

$$(\sigma_s^2 = u'^2 = v'^2 = w'^2)$$

A non-linear regression of Eq. 17 to measured weighted coherence values is used to estimate A , \bar{u} , σ_a and σ_s . Initial values of these parameters must be estimated for the regression algorithm:

A , σ_a and σ_s are estimated as follows:

- A weighted coherence at $\Delta x = 0$, $\Delta t = 0$
- σ_a least squares fit to Eq. 17 for data points near $\Delta t = 0$ and
for $\Delta x = 0$
- σ_s 25% of the estimated mean wind speed.

A first approximation to the lateral velocity component, \bar{u} , can be obtained from the time delay, Δt_e , when the weighted coherence at zero separation is equal to the weighted coherence at separation Δx :

$$\bar{u} = \Delta x / 2\Delta t_e \quad (18)$$

where Δt_e is obtained as shown in Fig. 3. Equation 18 is derived, following Briggs et al. 1950, from Equation 17 by setting:

$$\overline{\text{coh}}(0, \Delta t_e) = \overline{\text{coh}}(\Delta x, \Delta t_e) \quad (19)$$

Data points for the regression analysis are chosen about the maximum weighted coherence for each lateral separation. An example of the measured weighted coherence and the fit provided by this regression is presented in Fig. 3. The inability of this model to fit the data exactly is due to limitations in the Gaussian approximations employed in the derivation of Eq. 17. This model is used, despite its shortcomings, because it is easily applied and has been shown to provide reasonable values for \bar{u} and σ_s . (A more complete discussion of this modelling problem in the case of grid generated turbulence can be found in Comte-Bellot et al., 1971.)

The radial velocity is obtained from the phase of the smoothed cross spectra as follows:

$$\bar{v} = \frac{1}{m} \sum_{k=k_1}^{k_m} W(k) v_r(k) \cos\theta \quad (20)$$

where: $v_r(k) = \Delta\psi(k)/(2\pi k\Delta t)$ radial velocity of wavenumber, k
 $\Delta\psi(k)$ phase shift in the smoothed aerosol cross spectrum.

The mean wind speed and direction are calculated from:

$$v_{\text{lidar}} = (\bar{u}^2 + \bar{v}^2)^{1/2} \quad (21)$$

$$\phi_{\text{lidar}} = 180^\circ + \phi_2 + \tan^{-1} (\bar{u}/\bar{v}) \quad (22)$$

where ϕ_2 is shown in Fig. 1 and where \bar{v} is the horizontal projection of the average radial velocity.

IV. Experimental Results

Remote wind measurement experiments were conducted in Madison, Wisconsin and at the White Sand Missile Range, New Mexico. All lidar measurements were obtained using a three angle azimuthal scan with a 1.0° azimuth separation and a laser repetition rate of .9 Hz. Each lidar wind determination was calculated from aerosol inhomogeneity cross spectra smoothed over a five minute time interval.

Lidar measurements obtained in Madison, Wisconsin were compared to a bivane anemometer (R.M. Young model 21002) mounted on a radio tower located 2.7 km from the lidar. The lidar beam pattern was centered on the tower, with the lidar operated at a 2.3° elevation angle in order to place the lidar beam at the same altitude (77 m) as the anemometer. The anemometer signals were digitized and recorded at a 1 Hz rate; wind speed and direction were obtained

by averaging radial and cross beam components of the wind over the five minute periods of the lidar measurements. Anemometer measurements of σ_s were calculated from the rms mean of the turbulent velocity components u , v and w :

$$\sigma_{s(\text{tower})} = ((\overline{u'^2} + \overline{v'^2} + \overline{w'^2})/3)^{1/2} \quad (23)$$

All Madison wind comparisons were made on clear sunny days. Figure 4 shows a time history of lidar and tower measured winds obtained on June 20, 1977. Figure 5 presents a comparison of lidar and anemometer measurements of wind speed, direction and rms fluctuations, σ_s , for six separate days. All lidar measurements made on these days with $\overline{\text{SNR}}$ greater than .5 are presented.

Although it is rather difficult to estimate reliable confidence limits for lidar measurements, error bars have been plotted in Figure 5. The lidar error estimates show the combined effects of a plus or minus 1.1 sec error (one laser shot interval) in measuring the cross path drift time and a plus or minus 15 meter (one data point) error in determining the phase shift of the cross spectra. The error bars for the lidar σ measurements are 95% confidence limits provided by the non-linear regression procedure.

We believe that largest error source in the anemometer measurement is not due to intrinsic instrumented error but rather the uncertainty of comparing a measurement made at a single point with the 1 kilometer spatial average obtained with the lidar. The error bars for the anemometer derived winds show the expected errors, Δu , Δv , in determining the ensemble average wind from a 5 minute single point average:

$$\Delta u = (\overline{u'^2} \cdot \frac{5 \text{ min}}{\tau_E})^{1/2} \quad (24)$$

$$\Delta v = (\overline{v'^2} \cdot \frac{5 \text{ min}}{\tau_E})^{1/2} \quad (25)$$

where: $\overline{u'^2}$ and $\overline{v'^2}$ along with the Eulerian time scale, τ_E (Csanady, 1973),

-12-

are measured from tower data segments of approximately one half hour duration. The error bars for the tower measurements of σ_s are given by the fluctuations of sigma values measured in 5 or 6, 5 minute segments near the time of the tower measurement.

Lidar measurements made in Madison are consistent with concurrent tower measurements. The rms differences in speed and azimuth were 1.0 m/s and 10° respectively. These errors are roughly consistent with the errors expected due to discrete temporal and spatial sampling of the lidar along with errors in estimating a volume averaged wind with a single point sampling.

At White Sands, New Mexico, wind velocity measurements as a function of altitude were made with both lidar and radar tracked pilot balloons. Measurements on January 19, 1978 occurred under conditions of very light snow. These data are characterized by large fluctuations in the observed lidar profiles. They provide a test of lidar wind measurement algorithms without the need to separate small signals from noise. Wind measurements within vertical intervals of approximately 100 meters were obtained by operating the lidar at a 6° elevation angle and dividing the lidar profiles into 960 meter range intervals. For comparison the pilot balloon measurements were averaged over the same height intervals as the lidar. Figure 6 shows one such comparison. This figure shows a common feature of such comparisons: pilot balloon derived wind profiles show larger fluctuations than the lidar derived profiles. Lidar measurements are averaged over 960 meters along the lidar beam and over a 5 minute time interval. The pilot balloon provides a one point estimate of the wind during the time the balloon rises through the 100 meter slab (~ 30 sec). As a result, the lidar gives a better estimate of the mean wind profile than do pilot balloon observations. Figure 7 presents a comparison of all lidar and pilot balloon measurements made on Jan. 19, 1978. Error estimates shown

for the pilot balloon measurements are based on uncertainties in determining pilot balloon positions with the radar. Error estimates for the lidar are the same as for the Madison data. Because all error estimates for data of Figure 7 are similar, just the largest and the smallest set of error estimates are shown.

The lidar wind measurements show good agreement with simultaneous pilot balloon observations. For all data taken on at White Sands on Jan. 19, 1978 the rms errors in speed and direction were 1.1 m/sec and 7° respectively.

Figure 9 shows nocturnal wind observations made with both lidar and radar tracked pilot balloons. These data were obtained on a clear, cold night at White Sands missile range. A low level jet is clearly evident, as is a directional shear of nearly 90° at the top of the layer. Lidar data segments of 480 meters (32 data points), were used to obtain measurements in 50 meter vertical intervals. Above 330 meters the signal to noise ratio, $\overline{\text{SNR}}$ decreased below .5 and lidar wind measurements could not be obtained.

V. Conclusion

Experimental results demonstrate the ability of lidar to remotely measure the mean wind speed, direction and rms wind speed fluctuation using naturally occurring aerosol inhomogeneities as tracers. Inhomogeneity scale sizes ranging from 15 m to 500 m were found to contain useful wind information. Lidar wind measurements were possible for $\overline{\text{SNR}}$ values greater than .5. Signal to noise ratios are usually adequate to make wind measurements in the clear convective boundary layer at Madison, Wisconsin. Improvement in instrumentation to increase the $\overline{\text{SNR}}$ values will increase the range of conditions under which measurements can be obtained.

The fast Fourier transform technique presented in this paper provides wind measurements with much less computer time than the procedure described by Kunkel et al., 1979. The present technique is between 10 and 20 times as fast as the previous procedure.

Acknowledgments. We would like to express our appreciation to the Atmospheric Science Laboratory at the White Sands Missile Range for their cooperation during the experiments conducted there. This research was supported by USAROD grant DAA-C29-76-C-0156.

References

- Armstrong, R.L., J.B. Mason and T. Barber, 1976: Detection of Atmospheric Aerosol Flow using a Transit Time Lidar Velocimeter. *Appl. Opt.*, 15, 2891-2895.
- Bingham, C., M.D. Godfrey and J.W. Tukey, 1967: Modern Techniques of Power Spectrum Estimation. *IEEE Trans. on Audio and Electac.*, 15, 56-66.
- Briggs, B.H., G.J. Phillips and D.H. Shin, 1950: The Analysis of observations on Spaced Receivers of Fading Radio Signals. *Proc. of Phy. Soc.*, 62, 106-121.
- Comte-Bellot, Genevieve and Stanely Corsin, 1971: Simple Eulerian time correlation of full- and narrow-band velocity signals in grid-generated 'isotropic' turbulence. *Journal of Fluid Mechanics*, 48, 273-337.
- Csanady, C.T.: *Turbulent Diffusion in the Environment*.
D. Reidel Publishing Co., Boston, 248 pp.
- Derr, V.E., and C.G. Little, 1970: A Comparison of Remote Sensing of the Clear Atmosphere by Optical, Radio, and Acoustic Radar Techniques. *Appl. Opt.*, 9, 1982-1983.
- Eloranta, E.W., J.M. King and J.A. Weinman, 1975: The Determination of Wind Speeds in the Boundary Layer by Monostatic Lidar. *Journal of Applied Meteorology*, 14, 1485-1489.
- Kunkel, K.E., E.W. Eloranta and J.A. Weinman, 1979: Remote Determination of Boundary Layer Characteristics from Lidar Measurements. Submitted to *Journal of Atmospheric Science*.
- Otness, R.K. and L.D. Enochson, 1972: *Digital Times Series Analysis*.
John Wiley and Sons, New York, 476 pp.

Wainstein, L.A. and V.P. Zubakov, 1962: Extraction of Signals from Noise.

Dover Publications, Inc., New York, 382 pp.

Welsh, P.D., 1967: The use of Fast Fourier Transforms for Estimation of Power Spectra: A Method Based on Time Averaging over Short, Modified Periodograms. IEEE, 15, 70-73.

APPENDIX B

Reprinted from JOURNAL OF APPLIED METEOROLOGY, Vol. 16, No. 12, December 1977
American Meteorological Society
Printed in U. S. A.

Lidar Observations of the Convective Boundary Layer

K. E. KUNKEL, E. W. ELORANTA AND S. T. SHIPLEY

Lidar Observations of the Convective Boundary Layer

K. E. KUNKEL, E. W. ELORANTA AND S. T. SHIPLEY

Department of Meteorology, University of Wisconsin, Madison 53706

(Manuscript received 16 May 1977, in revised form 20 September 1977)

ABSTRACT

A scanning lidar system has been used to observe convection in the atmospheric boundary layer. In particular, cell sizes and geometry have been determined and circulation patterns in and around the cells have been measured.

The lidar data show that the preferred form of convective cells are plumes with roots near the surface. The majority of these plumes have aspect ratios between 0.5 and 1.5. The measurements of circulation patterns show the strongest rising motion on the upwind side of the cell with sinking motion on the downwind side. These observations show that lidar is a powerful tool for observing convection.

1. Introduction

Clear air convective plumes are both too large and too short-lived to be easily observed with conventional meteorological instrumentation. Typical cells have altitudes on the order of 1 km and lifetimes of much less than 1 h. The most successful studies have used instrumented aircraft to observe a field of cells (Lenschow, 1970; Warner and Telford, 1963, 1964, 1967) and/or very high power radars to map plumes by observing the changes in radio refractive index which occur at cell boundaries (Konrad, 1970; Konrad and Robinson, 1972, 1973; Hardy and Ottersten, 1969; Rowland, 1973, 1976).

This paper shows how lidar, the optical equivalent of radar, can be used to make detailed observations of developing convective cells. In the atmospheric boundary layer, the principal scattering sources for the lidar signal are aerosols and air molecules. Aerosol particulates are introduced into the atmosphere from a variety of sources, including windblown dust and man-made pollution sources. Most of these sources are at or near the earth's surface. Particulate matter which is injected into the air during the night is usually trapped in a thin layer near the ground. After sunrise, solar heating produces convective cells which transport these aerosols aloft. Lidar is able to give a two-dimensional picture of relative aerosol concentration, and the convective cells can therefore be identified by their higher aerosol concentration.

Lidar possesses several advantages in observing the convective field over other methods. Unlike airplane and tower measurements, lidar is able to give essentially instantaneous two-dimensional pictures of convection. This capability is also possessed by radar. According to Konrad (1970), however, radar apparently can observe

cells only at the top of the convective field where they have negative buoyancy and are cool and moist compared to the environment. In light wind situations, lidar is frequently able to observe cells nearly to the surface. Mechanical turbulence appears to mix surface layer dust under windy conditions, and convective structures can no longer be observed near the ground with the current instrumentation. Under these conditions, however, cells can still be observed some distance above the surface. The data presented here were collected from the Meteorology and Space Science Building at the University of Wisconsin with the lidar pointing west over a primarily residential area of Madison. It should therefore be kept in mind that the results may include effects due to the inhomogeneous nature of the urban terrain.

2. Instrumentation and method

The observations presented in this paper were made with a computer controlled scanning ruby lidar system. The system has a maximum repetition rate of 1 Hz at a pulse energy of 1.5 J and a range resolution of 15 m.

In a typical observation period the lidar system is scanned under computer control through a sequence of elevation angles (RHI scan) or of azimuth angles (PPI scan) (see Kunkel *et al.*, 1975). Individual lidar profiles are logarithmically amplified, digitized at a 10 MHz rate, and transferred to an on-line computer for processing. Each lidar profile consists of 512 digital values of the range and energy corrected signal specified at 15 m range intervals. Each value is proportional to the logarithm of the product $\beta_{180}(r) \exp[-2\tau(r)]$, where $\beta_{180}(r)$ is the volume backscatter cross section at range r and $\tau(r)$ is the optical thickness between the laser and the scattering volume. Aerosol carried within convec-

tive plumes increases the value of β'_{180} with respect to a background level and thus the plume becomes visible to lidar probing. To produce the pictures shown in this paper, the digital values from a sequence of lidar profiles comprising one angular scan are used to specify intensities at each point in a 500×672 picture array. Since the sequence of lidar profiles consist of an angular scan with individual profiles separated by typical angles of 0.5° , not all elements of the picture array have corresponding values in the profiles. The intermediate points in the picture array are therefore generated by a linear interpolation between the nearest lidar data points. A background level which was taken to be the signal level above the inversion is subtracted from all data points to enhance the contrast. When appreciable attenuation is present, a background level which decreases linearly with range is used to approximately correct for attenuation. On the clear blue sky days considered in this study, however, the optical thickness τ was small and attenuation effects could usually be neglected.

The enhanced picture arrays were then stored on a 9-track digital magnetic tape in a format suitable for display on the McIDAS (Smith, 1975) image display and processing system. McIDAS allows video display of the lidar picture array while providing flexible operator control over grey scale enhancements, picture magnification and false color enhancements as well as sequential display of frames to produce motion pictures. Fig. 1 is an example of an RHI picture as shown on the McIDAS video display. These data were collected on 28 September 1976 and show a variety of convective structures. The contrast here between the convective structures and the surrounding environment is large. Fig. 2 shows an RHI scan taken on 22 October 1976. In this case convection is occurring under a strong capping inversion at a height of 0.8 km. Here the contrast is much smaller. The dip in the inversion at a range of 3.7 km is caused by the plume at a range of 4.0 km.

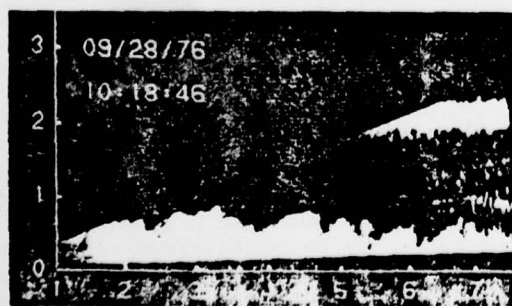


FIG. 1. RHI scan taken at Madison, Wisconsin, 28 September 1976 at 1010 CDT.

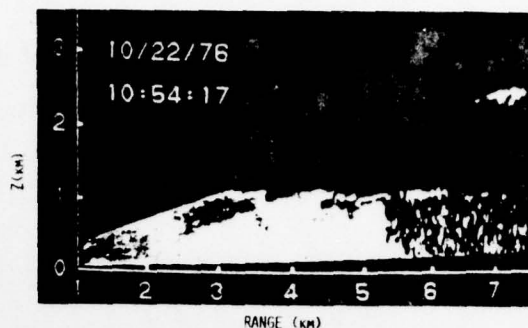


FIG. 2. RHI scan taken on 22 October 1976 which shows dips in the inversion at a range of 3.7 km due to plume at 4.0 km. Mean wind is to the left at 6.5 m s^{-1} .

3. General features of convective field

Controversy exists as to whether the individual convective elements are plume structures or bubbles. Airplane measurements by Warner and Telford (1963, 1967) and acoustic sounder observations by Hall (1972), among others, support a plume model. In contrast, radar observations by Hardy and Ottersten (1969), Konrad (1970) and Rowland (1976) show dome-like structures which Rowland interprets as bubbles.

In the lower part of the boundary layer, lidar RHI scans indicate that the most frequently occurring convective structure is a plume which has roots at or near the surface. These plumes on occasion have been observed to reach heights of 1500 m and still maintain their plume structure. The vertical velocity of the top of the plume is generally of the order of 1 m s^{-1} or more. We conclude from these observations that the plume structures are the primary mechanism for the vertical transport of heat near the surface. We also observe dome-like structures near the inversion top in the mature convective boundary layer. These structures probably correspond to the radar observed "bubbles." However, we hesitate to identify these structures with bubble convection models such as that of Scorer and Ludlam (1953).

The size of these convective elements as measured in other investigations is quite variable ranging from 100 m observed by Vulfson (1961) to as large as 2 km according to Konrad (1970). The lidar observations were used to measure the horizontal dimensions of the convective elements. Only convective elements with distinct boundaries and a coherent structure extending at least 150 m in the vertical were considered. The vertical dimension of these structures was always measured from the surface, and the diameter was measured at the point of largest horizontal extent. In some cases these plumes could be identified as distinct entities nearly to the surface. In other cases where the boundary layer was

well mixed, the plumes could only be seen where they intruded into the clear air above the inversion.

There are certain biases which may be present in the resulting measurements. Since the lidar sees a vertical slice through the plume, it will in general underestimate the size. For random vertical slices through a circular plume, the measured horizontal dimension will be greater than 50% of the actual diameter 87% of the time just from geometric considerations. However, since the lidar can usually make several vertical scans through the same plume and the largest diameter is taken, the actual measurements probably have less than a 10% error. Plumes are most visible to the lidar during mid and late morning when the inversion is rising most rapidly. The layer below the inversion becomes well mixed once a strong capping inversion is reached. Therefore, the great majority of plume sizes were measured at heights below 1 km and during a time when the boundary layer was rapidly evolving.

The lidar observations reveal a wide range of sizes with the following features. The observed dome-like structures exhibit diameters of 600–1500 m. This is in agreement with radar studies (e.g., Konrad, 1970). The plume structures are considerably smaller in diameter with a range of 100–800 m with the majority in the 200–500 m interval. Fig. 3 shows a probability distribution of plume top height z_p plotted as a function of plume diameter D . This plot was generated from measurements on 16 days distributed throughout the year. A total of 464 plumes were measured. We find that the diameter does not change significantly with

height for any given plume. However, Fig. 3 shows that the average diameter increases as the tops of the plumes, determined largely by the inversion height, get higher. These two facts are in qualitative agreement with the plume model of Telford (1966, 1970, 1972, 1975). Plume merging may be responsible for the increase in average plume size with inversion rise. We have observed several instances when this occurred. The lidar observations of cell size shown on the graph encompass the entire range which has been reported by other investigators. This suggests that the differences in reported plume sizes may be due to spatial and/or temporal sampling limitations.

The observed aspect ratio $A = D/Z_p$ of the majority of plumes is between 0.5 and 1.5 with an average value slightly less than 1.0. Willis and Deardorff (1976) found an average aspect ratio of 1.3 in a tank study. This falls within the range of the lidar measurements although it is slightly larger. In this tank study, the convective layer was allowed to reach a quasi-steady state. In contrast, the bulk of the lidar measurements were taken during periods of rapid growth in the boundary layer. This may account for the small difference in average aspect ratio.

Fig. 3 also shows that along a line of constant aspect ratio the probability of occurrence of plumes decreases above a height of about 250 m. This is a reflection of the average height of the capping inversion when the data were collected.

In order to see whether the urban nature of the surface affected the measured aspect ratios, lidar measurements were taken over Lake Mendota during Canadian cold air outbreaks in the late fall of 1976. Lake Mendota is located on the northwest side of Madison and is 5–7 km in diameter. The lake provided a flat and approximately isothermal heat source for convection. Measurements of aspect ratio taken on three separate days show essentially the same behavior as indicated in Fig. 2.

5. Measurement of convective circulation patterns: Case studies

Fig. 4 shows a time sequence of five RHI pictures taken on 29 April 1976 near 1045 CDT over urban terrain. The interval between frames was 80 s and the mean wind was less than 2 m s^{-1} . At the start of the sequence, skies were mostly clear and a few small cumulus clouds were beginning to form. These pictures clearly show two convective cells located approximately 3.5 and 6 km from the lidar. A small cumulus begins to form on the top of the cell at 6 km in frame 4b. This cumulus is responsible for the dark area in the upper left-hand corner of this and subsequent frames since the lidar cannot penetrate clouds.

The McIDAS system was used to map the circulation pattern in the layer by measuring the displacements of individual features in these frames. Fig. 5 shows frame 4a with these wind vectors superimposed. The base of

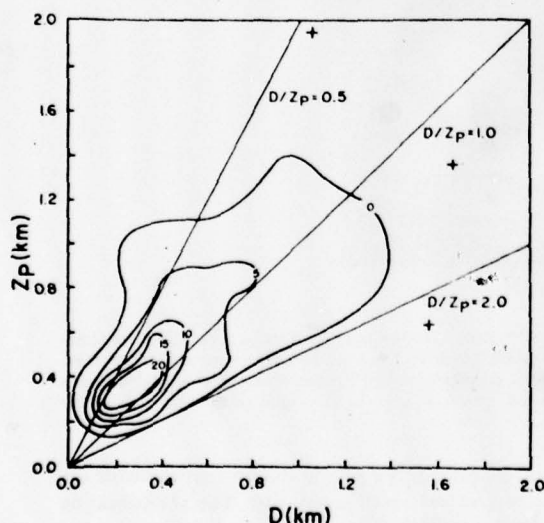


FIG. 3. Plume size versus plume height for lidar observations of convection over land. Contours show the number of plumes observed with height z_p and diameter D in $100 \text{ m} \times 100 \text{ m}$ size intervals. Crosses give location of individual plumes observed outside the zero probability contour.

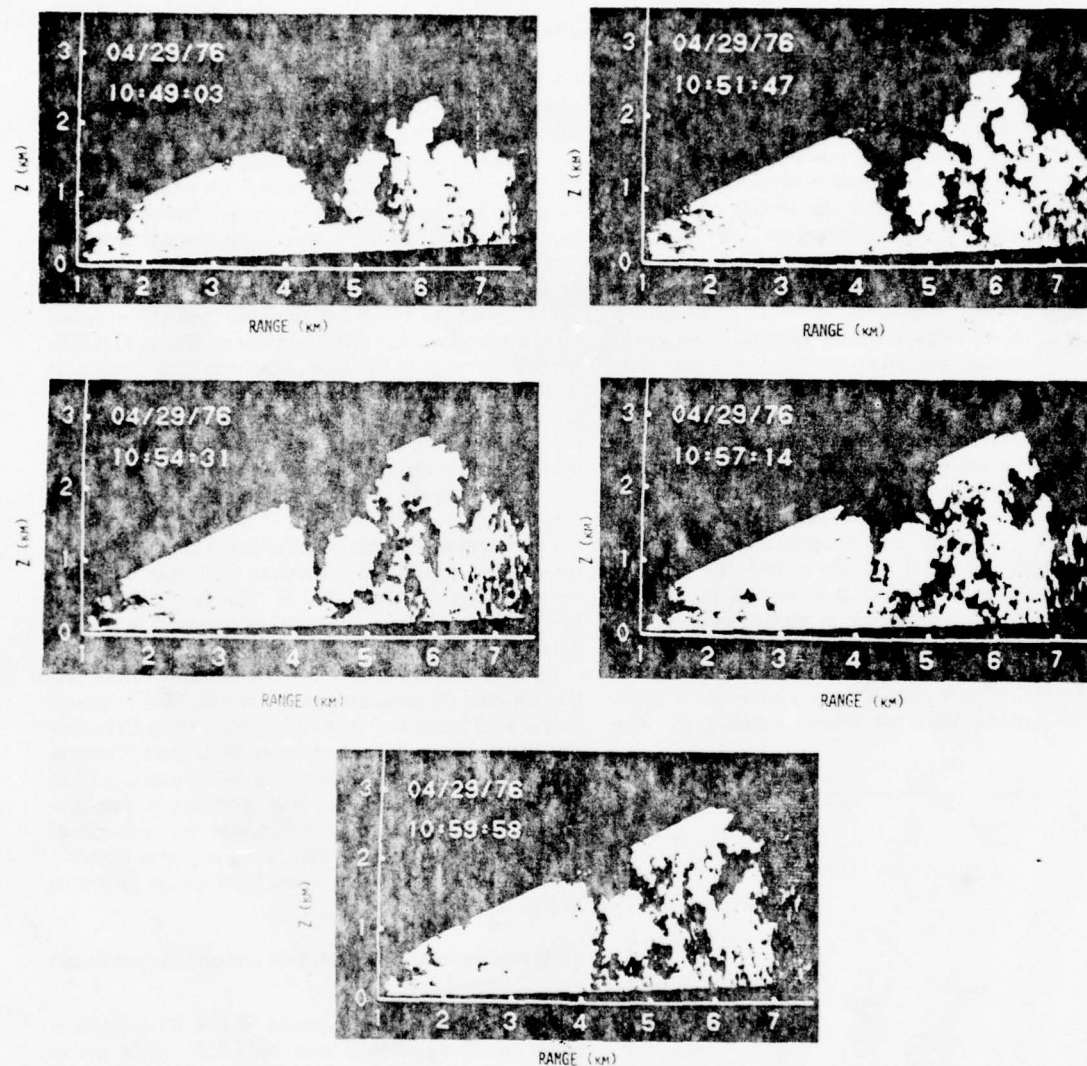


FIG. 4. Photographs of lidar range versus height displays showing the development of convective structure in a visually clear atmosphere on 29 April 1976. The white areas are those where aerosol density is somewhat greater than the ambient background. Observation times are shown in the figures. Notice the rapid development of the plume at a range of 6 km. Frames 4b–4e show a small cumulus cloud which has developed at the top of this plume in the time interval between frames 4a and 4b. The cloud quickly extinguishes the laser pulse causing a dark shadow at the upper right.

each vector is located at the position where the velocity was measured. These vectors indicate that most features are being advected slowly to the right in Fig. 5.

An interesting feature of the velocity field in Fig. 5 is that the strongest rising motion occurs on the upwind side of the cells. Aircraft and tower observations by Warner and Telford (1964, 1967), Lenschow (1970) and Kaimal and Businger (1970) indicate that the hottest part of a convective plume is on the upwind side. This is compatible with the present lidar observation. Since

the hottest part of the plume should coincide with the region of greatest vertical velocity. The compensating downdraft for both cells is considerably weaker and seems to occur preferentially on the downwind side of the cell. A model of a convective cell with rising motion upwind and sinking motion downwind is shown schematically in Fig. 6. This circulation has a sense of rotation about a horizontal axis perpendicular to the mean flow, suggesting that the rotational part of the circulation is dynamically driven by the shear flow.



FIG. 5. Wind vectors obtained from the displacement of plume structure in the 160 s time interval between frames 4a and 4b.

This type of circulation pattern has been observed by others in cumulus clouds (e.g., Byers, 1965, p. 178). The lidar data shows that this pattern exists before cloud formation has begun.

The observations of Fig. 4 also have implications for the parameterizations of vertical fluxes in convective boundary layers. Both cells shown in Fig. 4a have circulations which encompass nearly the entire depth of the boundary layer. The appropriate length scale of these vertical mixing processes must therefore be comparable to the inversion height z_i . Previous studies, e.g., Deardorff (1972) and Kaimal *et al.* (1976), have indicated that z_i is an important parameter in convective situations. The lidar depiction of convection gives visual support for this hypothesis.

Since typical vertical velocities in a convective field are around $0.1\text{--}1\text{ m s}^{-1}$, the vertical mixing of heat, momentum, water vapor, etc., is very rapid. In fact, vertical fluxes are probably entirely determined by the transport processes occurring in the viscous and surface

layers and by the rate of entrainment at the inversion. This is compatible with measurements of vertical profiles of wind and temperature which show that vertical gradients are weak or nonexistent in convective layers except near the top or bottom of the layer (see Clarke, 1970; Kaimal *et al.*, 1976).

Fig. 4 also visually illustrates the problems of using stationary *in situ* instruments to measure fluxes and other turbulence quantities in light wind convective situations. Over the entire period which these frames cover (~ 10 min), the convective cells have moved horizontally less than 0.5 km. Since the spacing between the two cells is about 3 km, an *in situ* sensor would sample about 1 cell h^{-1} . Any statistical description of the convective layer requires the sampling of many cells. But, during the morning when the boundary layer is evolving rapidly, the statistical description of the layer may change over the time period of 1 h. Obviously, an *in situ* sensor will fail to adequately describe the layer in such a situation.

6. Conclusions

These preliminary results indicate that a high spatial resolution lidar system with scanning capabilities is a powerful tool for the observation of the convective boundary layer. These lidar observations of convective motions show the following:

- 1) Convective plumes have roots near the surface. The lidar data indicate that the preferred form of convective cells are plumes rather than bubbles.
- 2) The observed plumes have a wide range of sizes, the majority having an aspect ratio between 0.5 and 1.5.
- 3) The lidar is able to observe circulation patterns in and around convective structures. These observations indicate that these cells have a maximum rising motion on the upwind side of the cell and sinking motion on the downwind side.

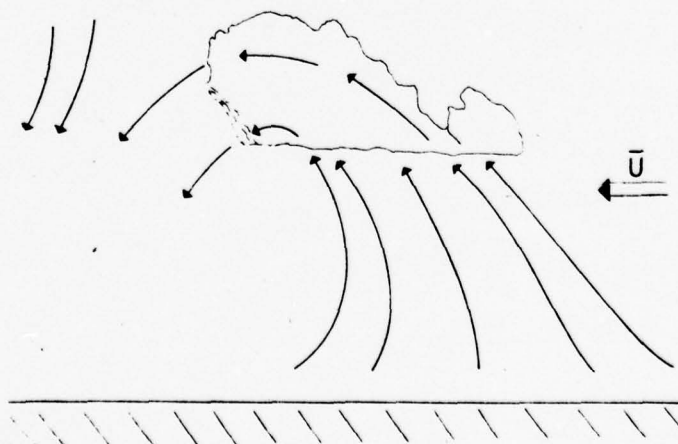


FIG. 6. Schematic view of the flow pattern observed around a developing fair weather cumulus cloud.

Acknowledgments. We would like to thank Professor James Weinman for his suggestions during the course of this work. This work was partially funded by USAROD grant DAAG29-76-C-0156. The senior author (Kunkel) was supported by a National Science Foundation fellowship during part of the work.

REFERENCES

- Byers, H. R., 1965: *Elements of Cloud Physics*. University of Chicago Press, 191 pp.
- Clarke, R. H., 1970: Observational studies in the atmospheric boundary layer. *Quart. J. Roy. Meteor. Soc.*, **96**, 91-114.
- Deardorff, J. W., 1972: Numerical investigations of neutral and unstable planetary boundary layers. *J. Atmos. Sci.*, **29**, 91-115.
- Hall, F. F., 1972: Temperature and wind structure studies by acoustic echo-sounding. *Remote Sensing of the Troposphere*, Govt. Printing Office, Chap. 18.
- Hardy, K. R., and H. Ottersten, 1969: Radar investigations of convective patterns in the clear atmosphere. *J. Atmos. Sci.*, **26**, 666-672.
- Kaimal, J. C., and J. A. Businger, 1970: Case studies of a convective plume and a dust devil. *J. Appl. Meteor.*, **9**, 612-620.
- , J. C. Wyngaard, D. A. Haugen, O. R. Coté, Y. Izumi, S. J. Caughey and C. J. Readings, 1976: Turbulence structure in the convective boundary layer. *J. Atmos. Sci.*, **33**, 2152-2169.
- Konrad, T. G., 1970: The dynamics of the convective process in clear air as seen by radar. *J. Atmos. Sci.*, **27**, 1138-1147.
- , and F. L. Robison, 1972: Simultaneous measurements of radar reflectivity and refractive index spectra in clear air convection. *J. Appl. Meteor.*, **11**, 1114-1119.
- , and —, 1973: Development and characteristics of free convection in the clear air as seen by radar and aircraft. *J. Appl. Meteor.*, **12**, 1284-1294.
- Kunkel, K. E., E. W. Eloranta and J. A. Weinman, 1975: Visualization of eddies in the planetary boundary layer by means of lidar. *Preprints Int. Conf. Environ. Sensing and Assessment*, Las Vegas, Amer. Meteor. Soc.
- Lenschow, D. H., 1970: Airplane measurements of planetary boundary layer structure. *J. Appl. Meteor.*, **9**, 874-884.
- Rowland, J. R., 1973: Intensive probing of a clear air convective field by radar and instrumented drone aircraft. *J. Appl. Meteor.*, **12**, 149-155.
- , 1976: Clear air convective behavior revealed by radar chaff. *J. Appl. Meteor.*, **15**, 521-526.
- Scorer, R. S., and F. H. Ludlam, 1953: Bubble theory of penetrative convection. *Quart. J. Roy. Meteor. Soc.*, **79**, 94-103.
- Smith, E., 1975: The McIDAS system. *IEEE Trans. Geosci. Electron.*, **GE-13**, No. 3.
- Telford, J. W., 1966: The convective mechanism in clear air. *J. Atmos. Sci.*, **23**, 652-666.
- , 1970: Convective plumes in a convective field. *J. Atmos. Sci.*, **27**, 347-358.
- , 1972: A plume theory for the convective field in clear air. *J. Atmos. Sci.*, **29**, 128-134.
- , 1975: The effect of compressibility and dissipation heating on boundary layer plumes. *J. Atmos. Sci.*, **32**, 108-115.
- , and J. Warner, 1964: Fluxes of heat and vapor in the lower atmosphere derived from aircraft observations. *J. Atmos. Sci.*, **21**, 539-548.
- Vulf'son, N. L., 1961: *Convective Motions in a Free Atmosphere*. Moscow, Gidrometerizdat. [English translation from NTIS, Ref. No. OTS64-11017.]
- Warner, J., and J. W. Telford, 1963: Some patterns of convection in the lower atmosphere. *J. Atmos. Sci.*, **20**, 313-318.
- , and —, 1967: Convection below cloud base. *J. Atmos. Sci.*, **24**, 374-382.
- Willis, G. E., and J. W. Deardorff, 1976: Visual observations of horizontal planforms of penetrative convection. *Preprints Third Symp. Atmospheric Turbulence, Diffusion and Air Quality*, Raleigh, Amer. Meteor. Soc., 9-12.

an objective criteria for rejecting wind determinations derived from noise dominated data.

$$\overline{\text{SNR}} = \sum_{k=k_1}^{k_m} W(k) \text{SNR}(k) \quad (16)$$

If the wind were constant in space and time, the mean cross path velocity, \bar{u} , could be determined from $\bar{u} = \Delta x / \Delta t_{\text{max}}$: where Δt_{max} is the time lag at which the weighted coherence, Eq. 13, is largest. In practice, wind velocity fluctuations cause the coherence maximum to decrease with increases in either Δx or Δt . As a result, the coherence maximum occurs at a time delay shorter than the cross path drift time. A model similar to the one employed by Kunkel et al. (1979) is used to correct for this effect. It assumes that the spatial distribution of the aerosol density is Gaussian and isotropic, and that these three-dimensional inhomogeneities are advected by a mean velocity plus a turbulent velocity with an isotropic Gaussian probability distribution. The functional form of this model is:

$$\overline{\text{coh}}(\Delta x, \Delta t) = A \left[\frac{2 \sigma_a^2}{2 \sigma_a^2 + \sigma_s^2 \Delta t} \right] \exp[-(\Delta x - \bar{u} \Delta t)^2 / (2 \sigma_a^2 + \sigma_s^2 \Delta t^2)] \cdot \sum_{k=k_1}^{k_m} W(k) \exp(-4\pi^2 k^2 \sigma_s^2 \Delta t^2) \quad (17)$$

where

$\overline{\text{coh}}(\Delta x, \Delta t)$ weighted coherence averaged over wavenumber

A an amplitude factor ($A \leq 1$)

\bar{u} mean lateral wind speed

σ_a RMS horizontal width of the aerosol inhomogeneities

σ_s RMS width of the isotropic Gaussian velocity distribution

$$(\sigma_s^2 = u'^2 = v'^2 = w'^2)$$

A non-linear regression of Eq. 17 to measured weighted coherence values is used to estimate A , \bar{u} , σ_a and σ_s . Initial values of these parameters must be estimated for the regression algorithm:

A , σ_a and σ_s are estimated as follows:

- A weighted coherence at $\Delta x = 0$, $\Delta t = 0$
- σ_a least squares fit to Eq. 17 for data points near $\Delta t = 0$ and
for $\Delta x = 0$
- σ_s 25% of the estimated mean wind speed.

A first approximation to the lateral velocity component, \bar{u} , can be obtained from the time delay, Δt_e , when the weighted coherence at zero separation is equal to the weighted coherence at separation Δx :

$$\bar{u} = \Delta x / 2\Delta t_e \quad (18)$$

where Δt_e is obtained as shown in Fig. 3. Equation 18 is derived, following Briggs et al. 1950, from Equation 17 by setting:

$$\overline{\text{coh}}(0, \Delta t_e) = \overline{\text{coh}}(\Delta x, \Delta t_e) \quad (19)$$

Data points for the regression analysis are chosen about the maximum weighted coherence for each lateral separation. An example of the measured weighted coherence and the fit provided by this regression is presented in Fig. 3. The inability of this model to fit the data exactly is due to limitations in the Gaussian approximations employed in the derivation of Eq. 17. This model is used, despite its shortcomings, because it is easily applied and has been shown to provide reasonable values for \bar{u} and σ_s . (A more complete discussion of this modelling problem in the case of grid generated turbulence can be found in Comte-Bellot et al., 1971.)

The radial velocity is obtained from the phase of the smoothed cross spectra as follows:

$$\bar{v} = \frac{1}{m} \sum_{k=k_1}^{k_m} W(k) v_r(k) \cos\theta \quad (20)$$

where: $v_r(k) = \Delta\psi(k)/(2\pi k\Delta t)$ radial velocity of wavenumber, k
 $\Delta\psi(k)$ phase shift in the smoothed aerosol cross spectrum.

The mean wind speed and direction are calculated from:

$$v_{\text{lidar}} = (\bar{u}^2 + \bar{v}^2)^{1/2} \quad (21)$$

$$\phi_{\text{lidar}} = 180^\circ + \phi_2 + \tan^{-1} (\bar{u}/\bar{v}) \quad (22)$$

where ϕ_2 is shown in Fig. 1 and where \bar{v} is the horizontal projection of the average radial velocity.

IV. Experimental Results

Remote wind measurement experiments were conducted in Madison, Wisconsin and at the White Sand Missile Range, New Mexico. All lidar measurements were obtained using a three angle azimuthal scan with a 1.0° azimuth separation and a laser repetition rate of .9 Hz. Each lidar wind determination was calculated from aerosol inhomogeneity cross spectra smoothed over a five minute time interval.

Lidar measurements obtained in Madison, Wisconsin were compared to a bivane anemometer (R.M. Young model 21002) mounted on a radio tower located 2.7 km from the lidar. The lidar beam pattern was centered on the tower, with the lidar operated at a 2.3° elevation angle in order to place the lidar beam at the same altitude (77 m) as the anemometer. The anemometer signals were digitized and recorded at a 1 Hz rate; wind speed and direction were obtained

by averaging radial and cross beam components of the wind over the five minute periods of the lidar measurements. Anemometer measurements of σ_s were calculated from the rms mean of the turbulent velocity components u , v and w :

$$\sigma_{s(\text{tower})} = ((\overline{u'^2} + \overline{v'^2} + \overline{w'^2})/3)^{1/2} \quad (23)$$

All Madison wind comparisons were made on clear sunny days. Figure 4 shows a time history of lidar and tower measured winds obtained on June 20, 1977. Figure 5 presents a comparison of lidar and anemometer measurements of wind speed, direction and rms fluctuations, σ_s , for six separate days. All lidar measurements made on these days with $\overline{\text{SNR}}$ greater than .5 are presented.

Although it is rather difficult to estimate reliable confidence limits for lidar measurements, error bars have been plotted in Figure 5. The lidar error estimates show the combined effects of a plus or minus 1.1 sec error (one laser shot interval) in measuring the cross path drift time and a plus or minus 15 meter (one data point) error in determining the phase shift of the cross spectra. The error bars for the lidar σ measurements are 95% confidence limits provided by the non-linear regression procedure.

We believe that largest error source in the anemometer measurement is not due to intrinsic instrumented error but rather the uncertainty of comparing a measurement made at a single point with the 1 kilometer spatial average obtained with the lidar. The error bars for the anemometer derived winds show the expected errors, Δu , Δv , in determining the ensemble average wind from a 5 minute single point average:

$$\Delta u = (\overline{u'^2} \cdot \frac{5 \text{ min}}{\tau_E})^{1/2} \quad (24)$$

$$\Delta v = (\overline{v'^2} \cdot \frac{5 \text{ min}}{\tau_E})^{1/2} \quad (25)$$

where: $\overline{u'^2}$ and $\overline{v'^2}$ along with the Eulerian time scale, τ_E (Csanady, 1973),

are measured from tower data segments of approximately one half hour duration. The error bars for the tower measurements of σ_g are given by the fluctuations of sigma values measured in 5 or 6, 5 minute segments near the time of the tower measurement.

Lidar measurements made in Madison are consistent with concurrent tower measurements. The rms differences in speed and azimuth were 1.0 m/s and 10° respectively. These errors are roughly consistent with the errors expected due to discrete temporal and spatial sampling of the lidar along with errors in estimating a volume averaged wind with a single point sampling.

At White Sands, New Mexico, wind velocity measurements as a function of altitude were made with both lidar and radar tracked pilot balloons. Measurements on January 19, 1978 occurred under conditions of very light snow. These data are characterized by large fluctuations in the observed lidar profiles. They provide a test of lidar wind measurement algorithms without the need to separate small signals from noise. Wind measurements within vertical intervals of approximately 100 meters were obtained by operating the lidar at a 6° elevation angle and dividing the lidar profiles into 960 meter range intervals. For comparison the pilot balloon measurements were averaged over the same height intervals as the lidar. Figure 6 shows one such comparison. This figure shows a common feature of such comparisons: pilot balloon derived wind profiles show larger fluctuations than the lidar derived profiles. Lidar measurements are averaged over 960 meters along the lidar beam and over a 5 minute time interval. The pilot balloon provides a one point estimate of the wind during the time the balloon rises through the 100 meter slab (~ 30 sec). As a result, the lidar gives a better estimate of the mean wind profile than do pilot balloon observations. Figure 7 presents a comparison of all lidar and pilot balloon measurements made on Jan. 19, 1978. Error estimates shown

for the pilot balloon measurements are based on uncertainties in determining pilot balloon positions with the radar. Error estimates for the lidar are the same as for the Madison data. Because all error estimates for data of Figure 7 are similar, just the largest and the smallest set of error estimates are shown.

The lidar wind measurements show good agreement with simultaneous pilot balloon observations. For all data taken on at White Sands on Jan. 19, 1978 the rms errors in speed and direction were 1.1 m/sec and 7° respectively.

Figure 9 shows nocturnal wind observations made with both lidar and radar tracked pilot balloons. These data were obtained on a clear, cold night at White Sands missile range. A low level jet is clearly evident, as is a directional shear of nearly 90° at the top of the layer. Lidar data segments of 480 meters (32 data points), were used to obtain measurements in 50 meter vertical intervals. Above 330 meters the signal to noise ratio, $\overline{\text{SNR}}$ decreased below .5 and lidar wind measurements could not be obtained.

V. Conclusion

Experimental results demonstrate the ability of lidar to remotely measure the mean wind speed, direction and rms wind speed fluctuation using naturally occurring aerosol inhomogeneities as tracers. Inhomogeneity scale sizes ranging from 15 m to 500 m were found to contain useful wind information. Lidar wind measurements were possible for $\overline{\text{SNR}}$ values greater than .5. Signal to noise ratios are usually adequate to make wind measurements in the clear convective boundary layer at Madison, Wisconsin. Improvement in instrumentation to increase the $\overline{\text{SNR}}$ values will increase the range of conditions under which measurements can be obtained.

The fast Fourier transform technique presented in this paper provides wind measurements with much less computer time than the procedure described by Kunkel et al., 1979. The present technique is between 10 and 20 times as fast as the previous procedure.

Acknowledgments. We would like to express our appreciation to the Atmospheric Science Laboratory at the White Sands Missile Range for their cooperation during the experiments conducted there. This research was supported by USAROD grant DAA-C29-76-C-0156.

References

- Armstrong, R.L., J.B. Mason and T. Barber, 1976: Detection of Atmospheric Aerosol Flow using a Transit Time Lidar Velocimeter. *Appl. Opt.*, 15, 2891-2895.
- Bingham, C., M.D. Godfrey and J.W. Tukey, 1967: Modern Techniques of Power Spectrum Estimation. *IEEE Trans. on Audio and Electac.*, 15, 56-66.
- Briggs, B.H., G.J. Phillips and D.H. Shin, 1950: The Analysis of observations on Spaced Receivers of Fading Radio Signals. *Proc. of Phy. Soc.*, 62, 106-121.
- Comte-Bellot, Genevieve and Stanely Corsin, 1971: Simple Eulerian time correlation of full- and narrow-band velocity signals in grid-generated 'isotropic' turbulence. *Journal of Fluid Mechanics*, 48, 273-337.
- Csanady, C.T.: *Turbulent Diffusion in the Environment*.
D. Reidel Publishing Co., Boston, 248 pp.
- Derr, V.E., and C.G. Little, 1970: A Comparison of Remote Sensing of the Clear Atmosphere by Optical, Radio, and Acoustic Radar Techniques. *Appl. Opt.*, 9, 1982-1983.
- Eloranta, E.W., J.M. King and J.A. Weinman, 1975: The Determination of Wind Speeds in the Boundary Layer by Monostatic Lidar. *Journal of Applied Meteorology*, 14, 1485-1489.
- Kunkel, K.E., E.W. Eloranta and J.A. Weinman, 1979: Remote Determination of Boundary Layer Characteristics from Lidar Measurements. Submitted to *Journal of Atmospheric Science*.
- Otness, R.K. and L.D. Enochson, 1972: *Digital Times Series Analysis*.
John Wiley and Sons, New York, 476 pp.

Wainstein, L.A. and V.P. Zubakov, 1962: Extraction of Signals from Noise.
Dover Publications, Inc., New York, 382 pp.

Welsh, P.D., 1967: The use of Fast Fourier Transforms for Estimation of
Power Spectra: A Method Based on Time Averaging over Short, Modified
Periodograms. IEEE, 15, 70-73.

Figure Captions

Figure 1. The geometry used for lidar wind measurements. The lidar is operated at a constant small elevation angle θ and scanned back and forth between three closely spaced azimuth angles ϕ_1 , ϕ_2 and ϕ_3 . Range resolved profiles of back-scattered intensity are recorded at ~ 1 second intervals for a period of 2 to 5 minutes to produce a wind measurement. Wind velocities are calculated in terms of a radial component, v , and a cross path component, u .

Figure 2. The signal to noise ratio as a function of wavenumber and the optimal filter estimated from Equations 15 and 12, respectively, for data obtained on Jan. 19, 1978 at White Sands, New Mexico.

Figure 3. An example of the weighted coherence, Eq. 13, as a function of time lag for three lateral separations, $\Delta x = 0$ m (\square), $\Delta x = 38$ m (\odot), $\Delta x = 76$ m (\triangle). A least squares regression of Eq. 17 to the data is shown by lines on the graph. The time lag, Δt_e , when the weighted coherence for zero angular separation and the 1° angular separation are equal is used with Eq. 18 to provide a first estimate of the cross path wind.

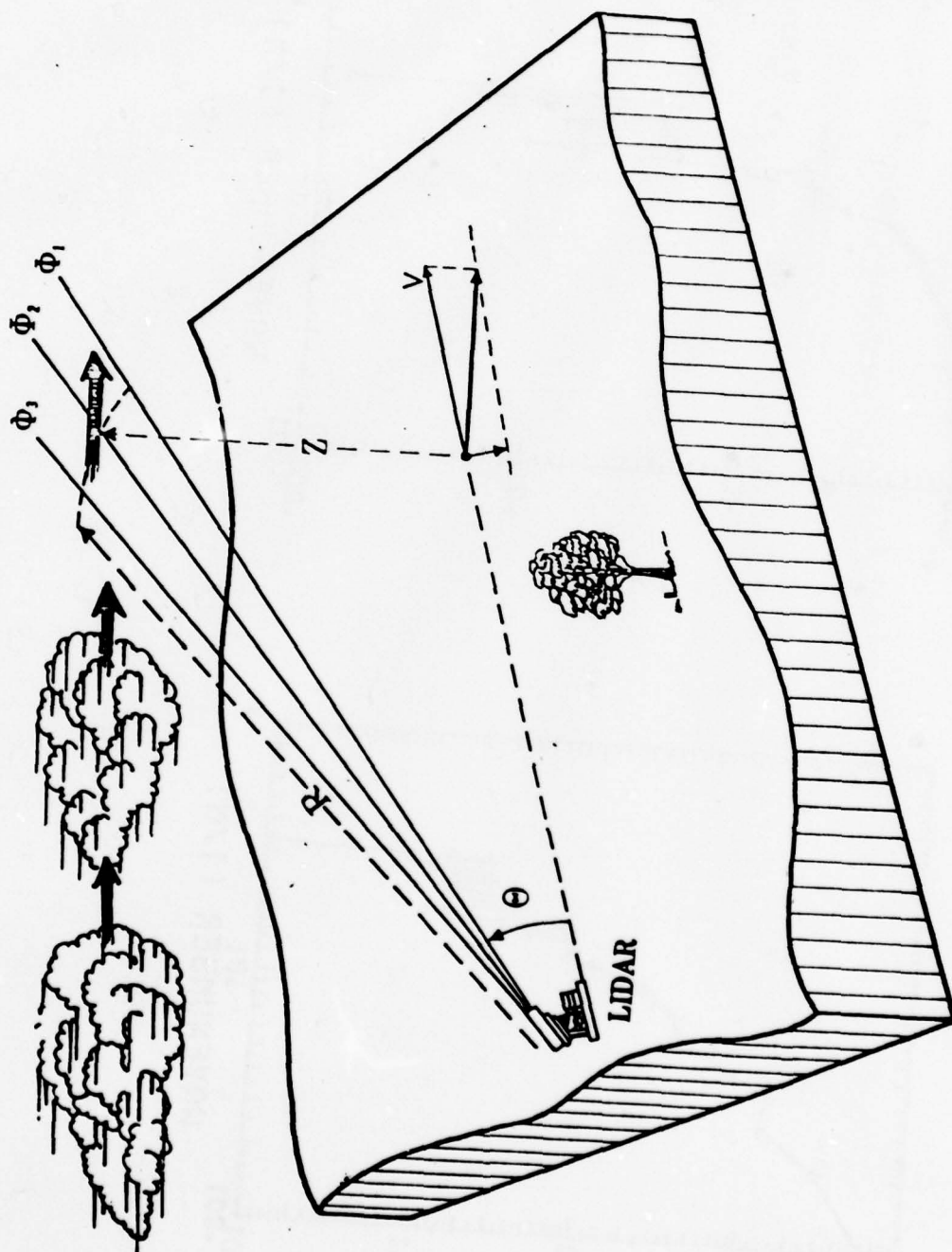
Figure 4. A time history comparison of winds measured on June 20, 1977 with lidar (solid lines) and a tower mounted anemometer (dashed line). These measurements were obtained on a clear day at Madison, Wisconsin.

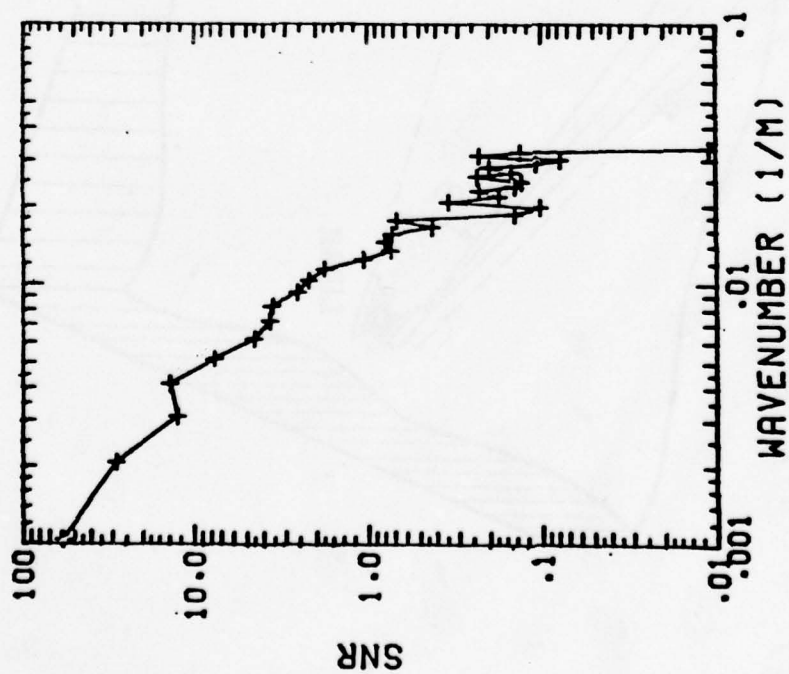
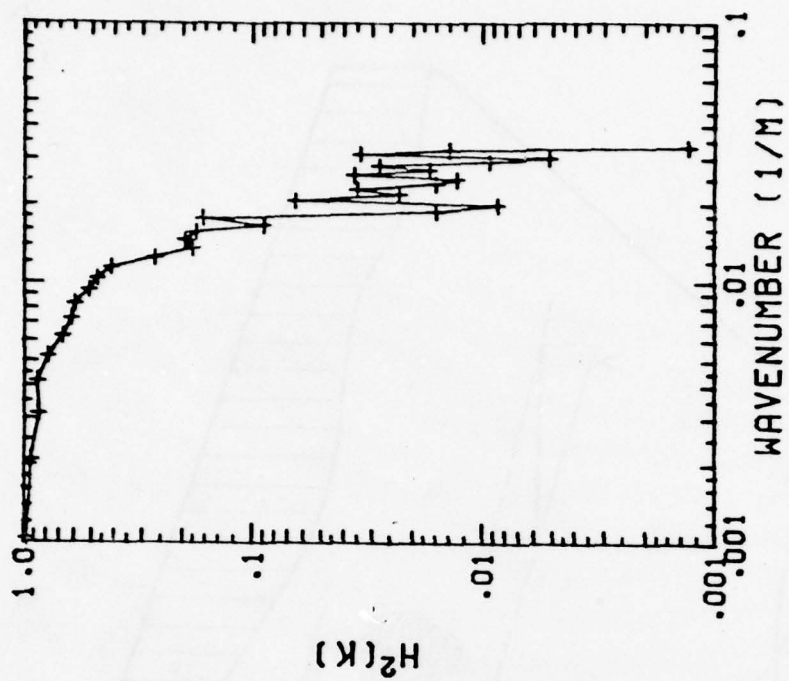
Figure 5. A comparison of winds measured under clear convective conditions at Madison, Wisconsin with lidar and a tower mounted anemometer on April 22 (\square), May 23 (\odot), June 20 (\triangle), June 23 (+), June 27 (\diamond), and July 27 (\star), 1977. The anemometer was centered within the lidar measurement volume and all measurements were averaged over the same time interval. Estimates of the uncertainty in both lidar and anemometer measurements are shown for each day.

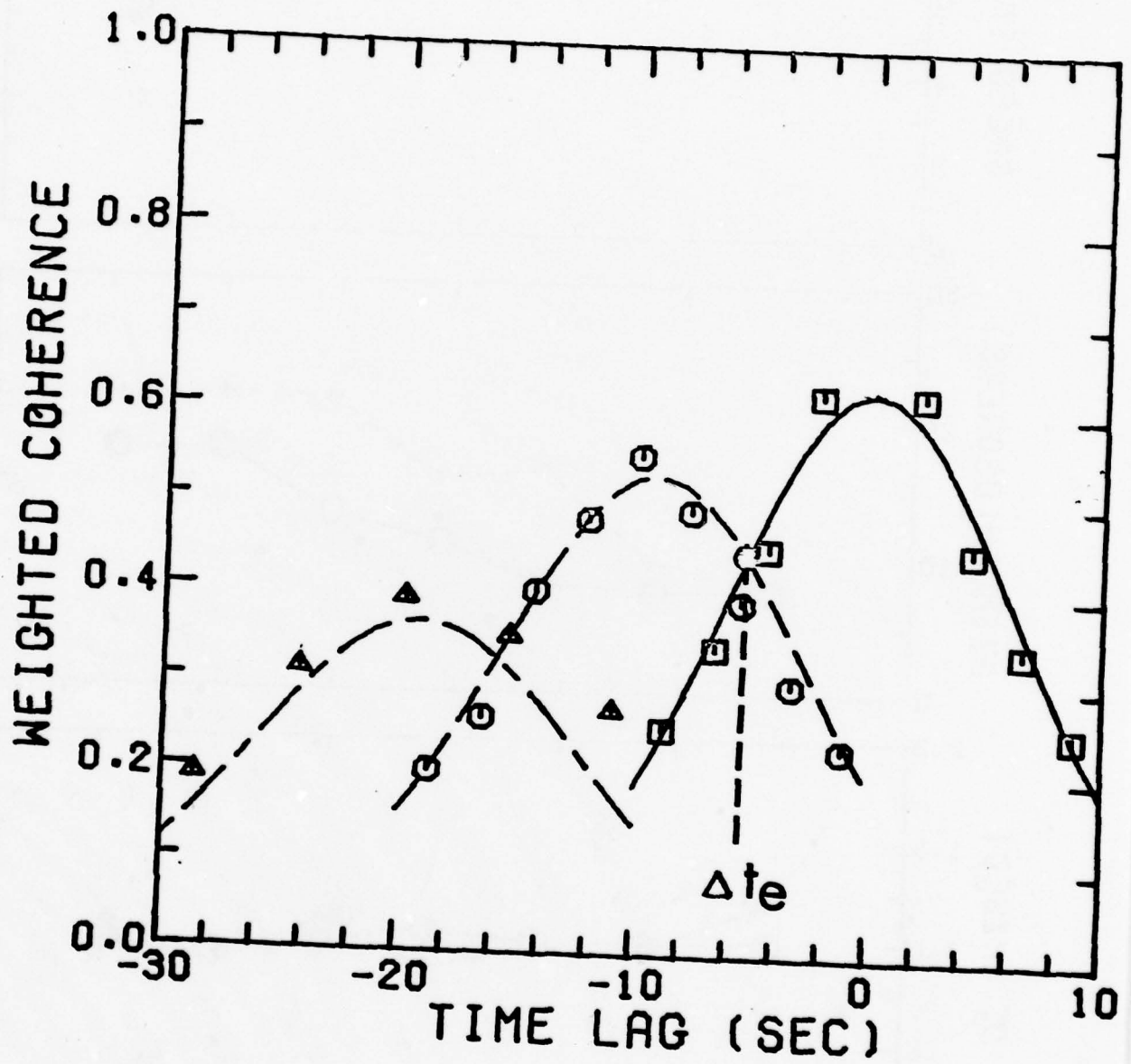
Figure 6. A comparison of lidar and pilot balloon wind measurements at White Sands, New Mexico on January 19, 1978. Lidar data was obtained between 1652 and 1657 mst and is plotted with solid lines. Pilot balloons are at 1645-1647 mst (- - - -) and 1655-1657 mst (— - —).

Figure 7. A comparison of winds measured at White Sands, New Mexico with lidar and radar tracked pilot balloons. All measurements were made during a light snowfall on January 19, 1978. Lidar and balloon measurements represent vertical averages over 100 meters, with the measurements centered at altitudes of 127 m (□), 227 m (⊙), 320 m (△), 410 m (+), 501 m (◇) and 594 (*). Two sets of estimated uncertainties in balloon and lidar measurements are shown: these represent the largest and smallest uncertainties computed for these data.

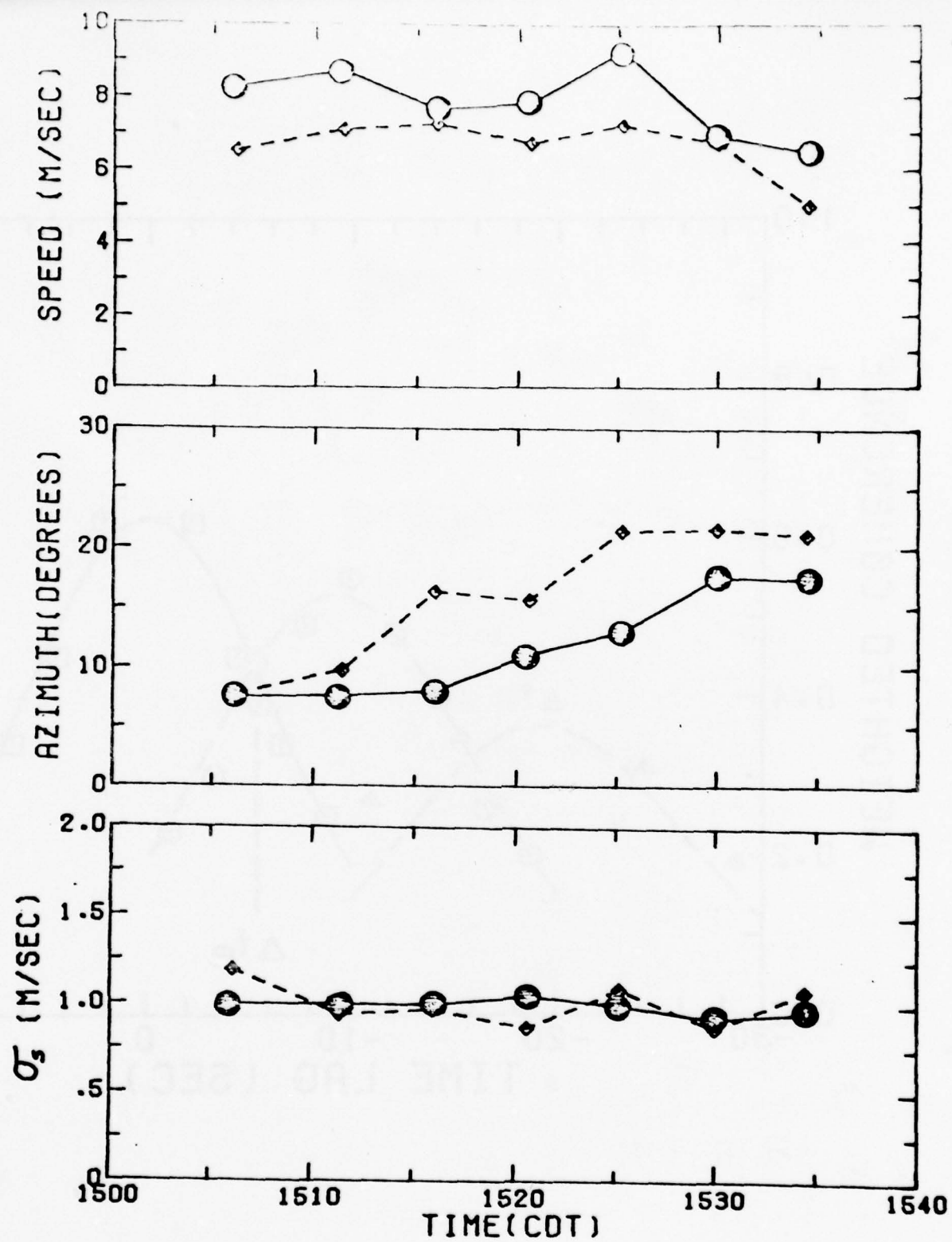
Figure 8. Wind profiles in the clear nocturnal boundary layer at White Sands, New Mexico on January 9, 1978. Strong directional shear is evident at an altitude of approximately 200 meters. Lidar wind measurements (2046 - 2051 mst) are compared to radar tracked pilot balloon observations at 2015 - 2018 mst (- - - - -), 2045-2048 mst (- — - — -), and 2105-2108 mst (——— - ———).

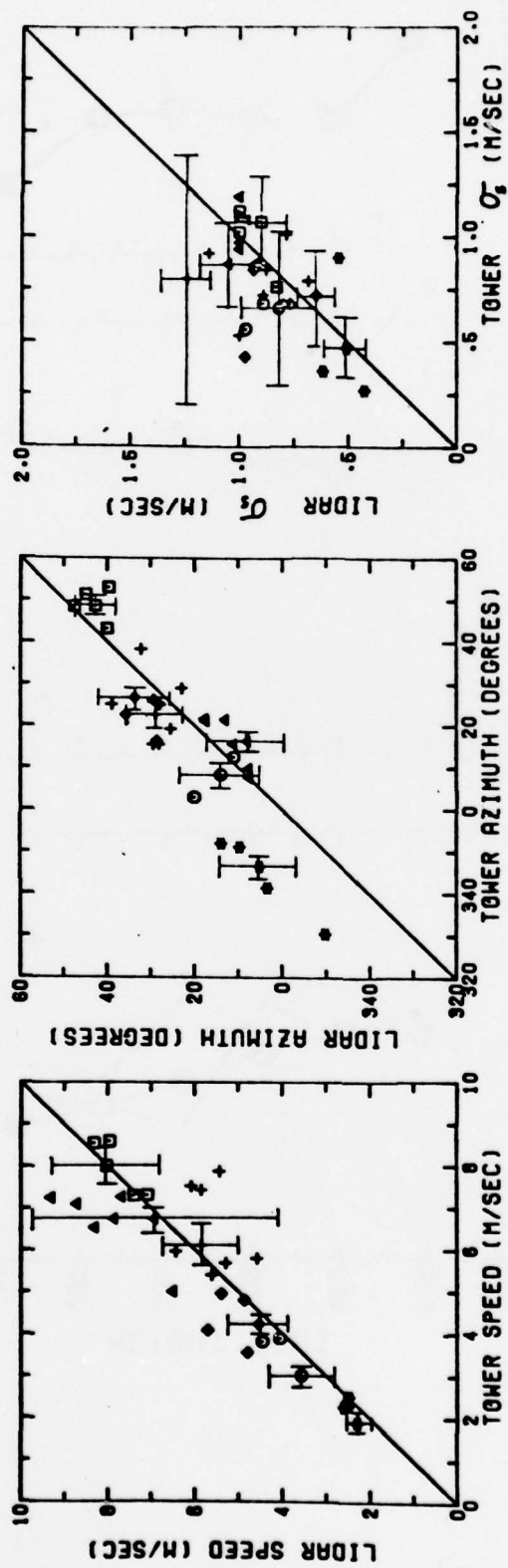


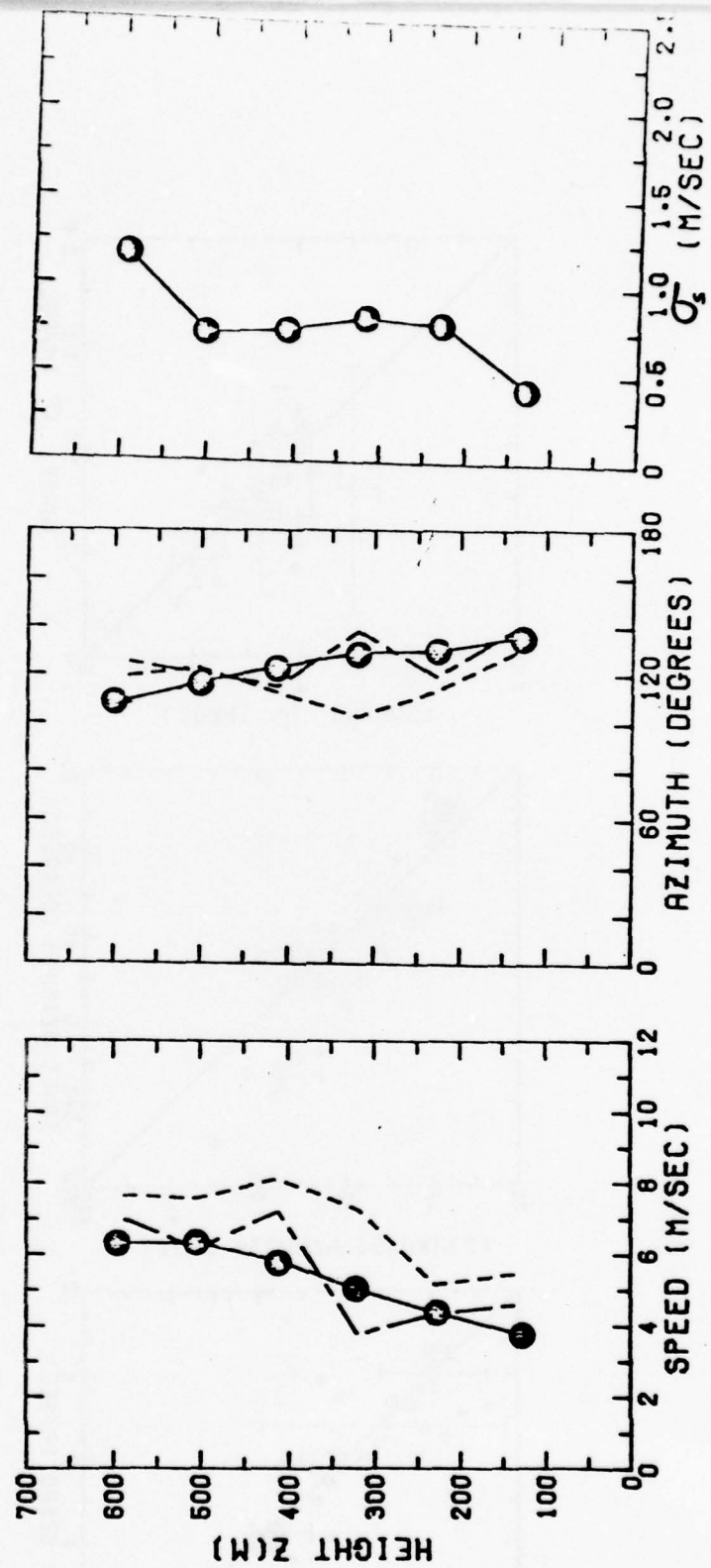


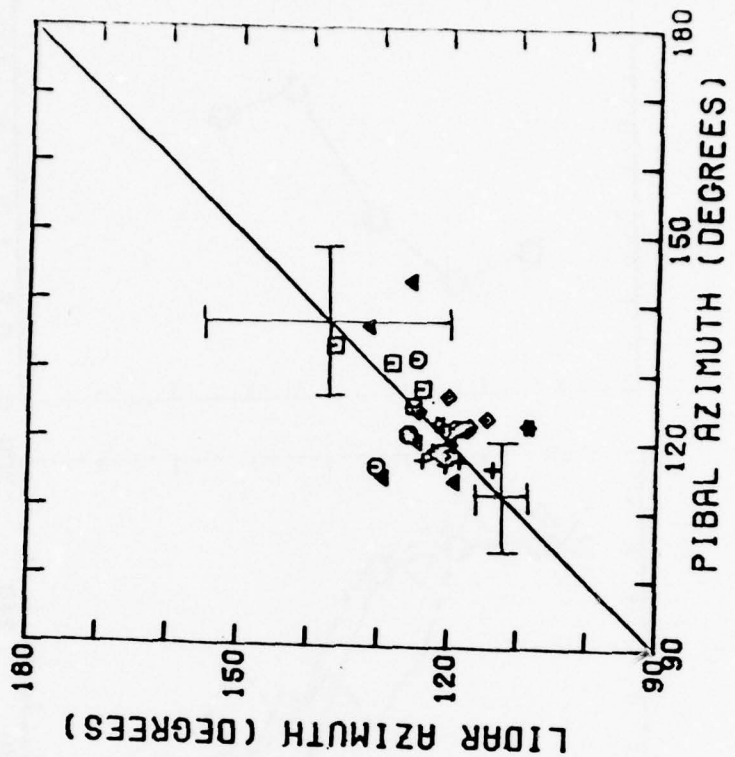
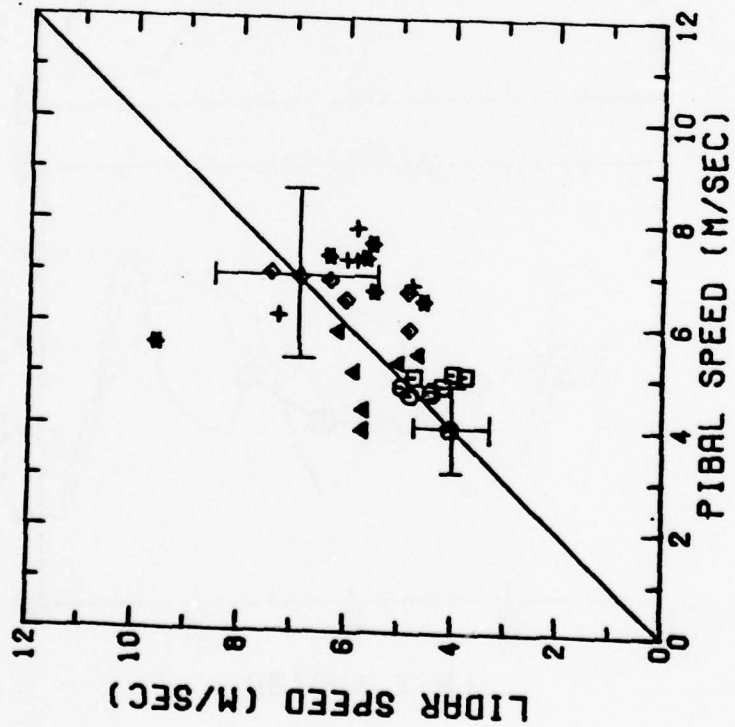


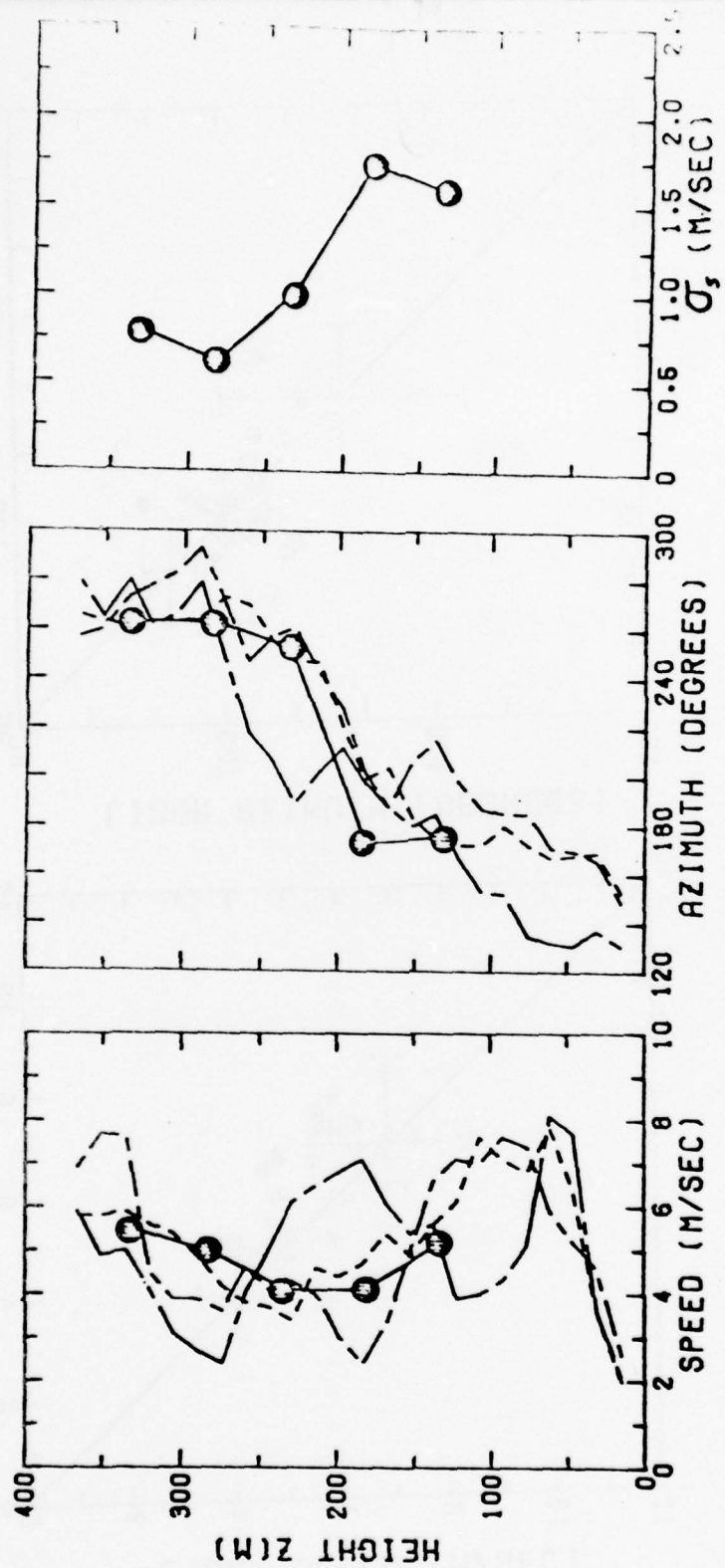
Fig











APPENDIX B

Reprinted from JOURNAL OF APPLIED METEOROLOGY, Vol. 16, No. 12, December 1977
American Meteorological Society
Printed in U. S. A.

Lidar Observations of the Convective Boundary Layer

K. E. KUNKEL, E. W. ELORANTA AND S. T. SHIPLEY

Wainstein, L.A. and V.P. Zubakov, 1962: Extraction of Signals from Noise.
Dover Publications, Inc., New York, 382 pp.

Welsh, P.D., 1967: The use of Fast Fourier Transforms for Estimation of
Power Spectra: A Method Based on Time Averaging over Short, Modified
Periodograms. IEEE, 15, 70-73.

Lidar Observations of the Convective Boundary Layer

K. E. KUNKEL, E. W. ELORANTA AND S. T. SHIPLEY

Department of Meteorology, University of Wisconsin, Madison 53706

(Manuscript received 16 May 1977, in revised form 20 September 1977)

ABSTRACT

A scanning lidar system has been used to observe convection in the atmospheric boundary layer. In particular, cell sizes and geometry have been determined and circulation patterns in and around the cells have been measured.

The lidar data show that the preferred form of convective cells are plumes with roots near the surface. The majority of these plumes have aspect ratios between 0.5 and 1.5. The measurements of circulation patterns show the strongest rising motion on the upwind side of the cell with sinking motion on the downwind side. These observations show that lidar is a powerful tool for observing convection.

1. Introduction

Clear air convective plumes are both too large and too short-lived to be easily observed with conventional meteorological instrumentation. Typical cells have altitudes on the order of 1 km and lifetimes of much less than 1 h. The most successful studies have used instrumented aircraft to observe a field of cells (Lenschow, 1970; Warner and Telford, 1963, 1964, 1967) and/or very high power radars to map plumes by observing the changes in radio refractive index which occur at cell boundaries (Konrad, 1970; Konrad and Robinson, 1972, 1973; Hardy and Ottersten, 1969; Rowland, 1973, 1976).

This paper shows how lidar, the optical equivalent of radar, can be used to make detailed observations of developing convective cells. In the atmospheric boundary layer, the principal scattering sources for the lidar signal are aerosols and air molecules. Aerosol particulates are introduced into the atmosphere from a variety of sources, including windblown dust and man-made pollution sources. Most of these sources are at or near the earth's surface. Particulate matter which is injected into the air during the night is usually trapped in a thin layer near the ground. After sunrise, solar heating produces convective cells which transport these aerosols aloft. Lidar is able to give a two-dimensional picture of relative aerosol concentration, and the convective cells can therefore be identified by their higher aerosol concentration.

Lidar possesses several advantages in observing the convective field over other methods. Unlike airplane and tower measurements, lidar is able to give essentially instantaneous two-dimensional pictures of convection. This capability is also possessed by radar. According to Konrad (1970), however, radar apparently can observe

cells only at the top of the convective field where they have negative buoyancy and are cool and moist compared to the environment. In light wind situations, lidar is frequently able to observe cells nearly to the surface. Mechanical turbulence appears to mix surface layer dust under windy conditions, and convective structures can no longer be observed near the ground with the current instrumentation. Under these conditions, however, cells can still be observed some distance above the surface. The data presented here were collected from the Meteorology and Space Science Building at the University of Wisconsin with the lidar pointing west over a primarily residential area of Madison. It should therefore be kept in mind that the results may include effects due to the inhomogeneous nature of the urban terrain.

2. Instrumentation and method

The observations presented in this paper were made with a computer controlled scanning ruby lidar system. The system has a maximum repetition rate of 1 Hz at a pulse energy of 1.5 J and a range resolution of 15 m.

In a typical observation period the lidar system is scanned under computer control through a sequence of elevation angles (RHI scan) or of azimuth angles (PPI scan) (see Kunkel *et al.*, 1975). Individual lidar profiles are logarithmically amplified, digitized at a 10 MHz rate, and transferred to an on-line computer for processing. Each lidar profile consists of 512 digital values of the range and energy corrected signal specified at 15 m range intervals. Each value is proportional to the logarithm of the product $\beta_{180}(r) \exp[-2\tau(r)]$, where $\beta_{180}(r)$ is the volume backscatter cross section at range r and $\tau(r)$ is the optical thickness between the laser and the scattering volume. Aerosol carried within convec-

tive plumes increases the value of β'_{180} with respect to a background level and thus the plume becomes visible to lidar probing. To produce the pictures shown in this paper, the digital values from a sequence of lidar profiles comprising one angular scan are used to specify intensities at each point in a 500×672 picture array. Since the sequence of lidar profiles consist of an angular scan with individual profiles separated by typical angles of 0.5° , not all elements of the picture array have corresponding values in the profiles. The intermediate points in the picture array are therefore generated by a linear interpolation between the nearest lidar data points. A background level which was taken to be the signal level above the inversion is subtracted from all data points to enhance the contrast. When appreciable attenuation is present, a background level which decreases linearly with range is used to approximately correct for attenuation. On the clear blue sky days considered in this study, however, the optical thickness τ was small and attenuation effects could usually be neglected.

The enhanced picture arrays were then stored on a 9-track digital magnetic tape in a format suitable for display on the McIDAS (Smith, 1975) image display and processing system. McIDAS allows video display of the lidar picture array while providing flexible operator control over grey scale enhancements, picture magnification and false color enhancements as well as sequential display of frames to produce motion pictures. Fig. 1 is an example of an RHI picture as shown on the McIDAS video display. These data were collected on 28 September 1976 and show a variety of convective structures. The contrast here between the convective structures and the surrounding environment is large. Fig. 2 shows an RHI scan taken on 22 October 1976. In this case convection is occurring under a strong capping inversion at a height of 0.8 km. Here the contrast is much smaller. The dip in the inversion at a range of 3.7 km is caused by the plume at a range of 4.0 km.

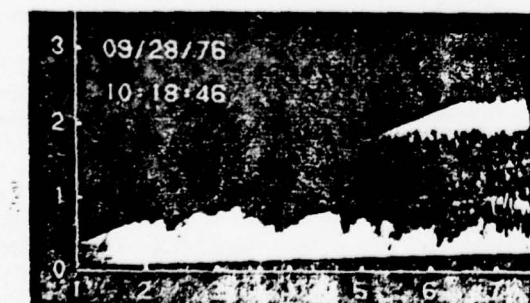


FIG. 1. RHI scan taken at Madison, Wisconsin, 28 September 1976 at 1010 CDT.

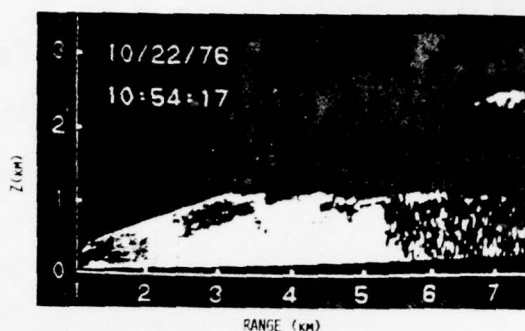


FIG. 2. RHI scan taken on 22 October 1976 which shows dips in the inversion at a range of 3.7 km due to plume at 4.0 km. Mean wind is to the left at 6.5 m s^{-1} .

3. General features of convective field

Controversy exists as to whether the individual convective elements are plume structures or bubbles. Airplane measurements by Warner and Telford (1963, 1967) and acoustic sounder observations by Hall (1972), among others, support a plume model. In contrast, radar observations by Hardy and Ottersten (1969), Konrad (1970) and Rowland (1976) show dome-like structures which Rowland interprets as bubbles.

In the lower part of the boundary layer, lidar RHI scans indicate that the most frequently occurring convective structure is a plume which has roots at or near the surface. These plumes on occasion have been observed to reach heights of 1500 m and still maintain their plume structure. The vertical velocity of the top of the plume is generally of the order of 1 m s^{-1} or more. We conclude from these observations that the plume structures are the primary mechanism for the vertical transport of heat near the surface. We also observe dome-like structures near the inversion top in the mature convective boundary layer. These structures probably correspond to the radar observed "bubbles." However, we hesitate to identify these structures with bubble convection models such as that of Scorer and Ludlam (1953).

The size of these convective elements as measured in other investigations is quite variable ranging from 100 m observed by Vulfson (1961) to as large as 2 km according to Konrad (1970). The lidar observations were used to measure the horizontal dimensions of the convective elements. Only convective elements with distinct boundaries and a coherent structure extending at least 150 m in the vertical were considered. The vertical dimension of these structures was always measured from the surface, and the diameter was measured at the point of largest horizontal extent. In some cases these plumes could be identified as distinct entities nearly to the surface. In other cases where the boundary layer was

well mixed, the plumes could only be seen where they intruded into the clear air above the inversion.

There are certain biases which may be present in the resulting measurements. Since the lidar sees a vertical slice through the plume, it will in general underestimate the size. For random vertical slices through a circular plume, the measured horizontal dimension will be greater than 50% of the actual diameter 87% of the time just from geometric considerations. However, since the lidar can usually make several vertical scans through the same plume and the largest diameter is taken, the actual measurements probably have less than a 10% error. Plumes are most visible to the lidar during mid and late morning when the inversion is rising most rapidly. The layer below the inversion becomes well mixed once a strong capping inversion is reached. Therefore, the great majority of plume sizes were measured at heights below 1 km and during a time when the boundary layer was rapidly evolving.

The lidar observations reveal a wide range of sizes with the following features. The observed dome-like structures exhibit diameters of 600–1500 m. This is in agreement with radar studies (e.g., Konrad, 1970). The plume structures are considerably smaller in diameter with a range of 100–800 m with the majority in the 200–500 m interval. Fig. 3 shows a probability distribution of plume top height z_p plotted as a function of plume diameter D . This plot was generated from measurements on 16 days distributed throughout the year. A total of 464 plumes were measured. We find that the diameter does not change significantly with

height for any given plume. However, Fig. 3 shows that the average diameter increases as the tops of the plumes, determined largely by the inversion height, get higher. These two facts are in qualitative agreement with the plume model of Telford (1966, 1970, 1972, 1975). Plume merging may be responsible for the increase in average plume size with inversion rise. We have observed several instances when this occurred. The lidar observations of cell size shown on the graph encompass the entire range which has been reported by other investigators. This suggests that the differences in reported plume sizes may be due to spatial and/or temporal sampling limitations.

The observed aspect ratio $A = D/Z_p$ of the majority of plumes is between 0.5 and 1.5 with an average value slightly less than 1.0. Willis and Deardorff (1976) found an average aspect ratio of 1.3 in a tank study. This falls within the range of the lidar measurements although it is slightly larger. In this tank study, the convective layer was allowed to reach a quasi-steady state. In contrast, the bulk of the lidar measurements were taken during periods of rapid growth in the boundary layer. This may account for the small difference in average aspect ratio.

Fig. 3 also shows that along a line of constant aspect ratio the probability of occurrence of plumes decreases above a height of about 250 m. This is a reflection of the average height of the capping inversion when the data were collected.

In order to see whether the urban nature of the surface affected the measured aspect ratios, lidar measurements were taken over Lake Mendota during Canadian cold air outbreaks in the late fall of 1976. Lake Mendota is located on the northwest side of Madison and is 5–7 km in diameter. The lake provided a flat and approximately isothermal heat source for convection. Measurements of aspect ratio taken on three separate days show essentially the same behavior as indicated in Fig. 2.

5. Measurement of convective circulation patterns: Case studies

Fig. 4 shows a time sequence of five RHI pictures taken on 29 April 1976 near 1045 CDT over urban terrain. The interval between frames was 80 s and the mean wind was less than 2 m s^{-1} . At the start of the sequence, skies were mostly clear and a few small cumulus clouds were beginning to form. These pictures clearly show two convective cells located approximately 3.5 and 6 km from the lidar. A small cumulus begins to form on the top of the cell at 6 km in frame 4b. This cumulus is responsible for the dark area in the upper left-hand corner of this and subsequent frames since the lidar cannot penetrate clouds.

The McIDAS system was used to map the circulation pattern in the layer by measuring the displacements of individual features in these frames. Fig. 5 shows frame 4a with these wind vectors superimposed. The base of

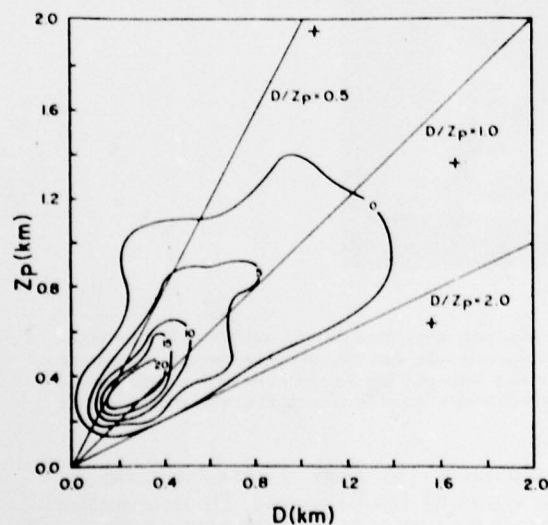


FIG. 3. Plume size versus plume height for lidar observations of convection over land. Contours show the number of plumes observed with height z_p and diameter D in $100 \text{ m} \times 100 \text{ m}$ size intervals. Crosses give location of individual plumes observed outside the zero probability contour.

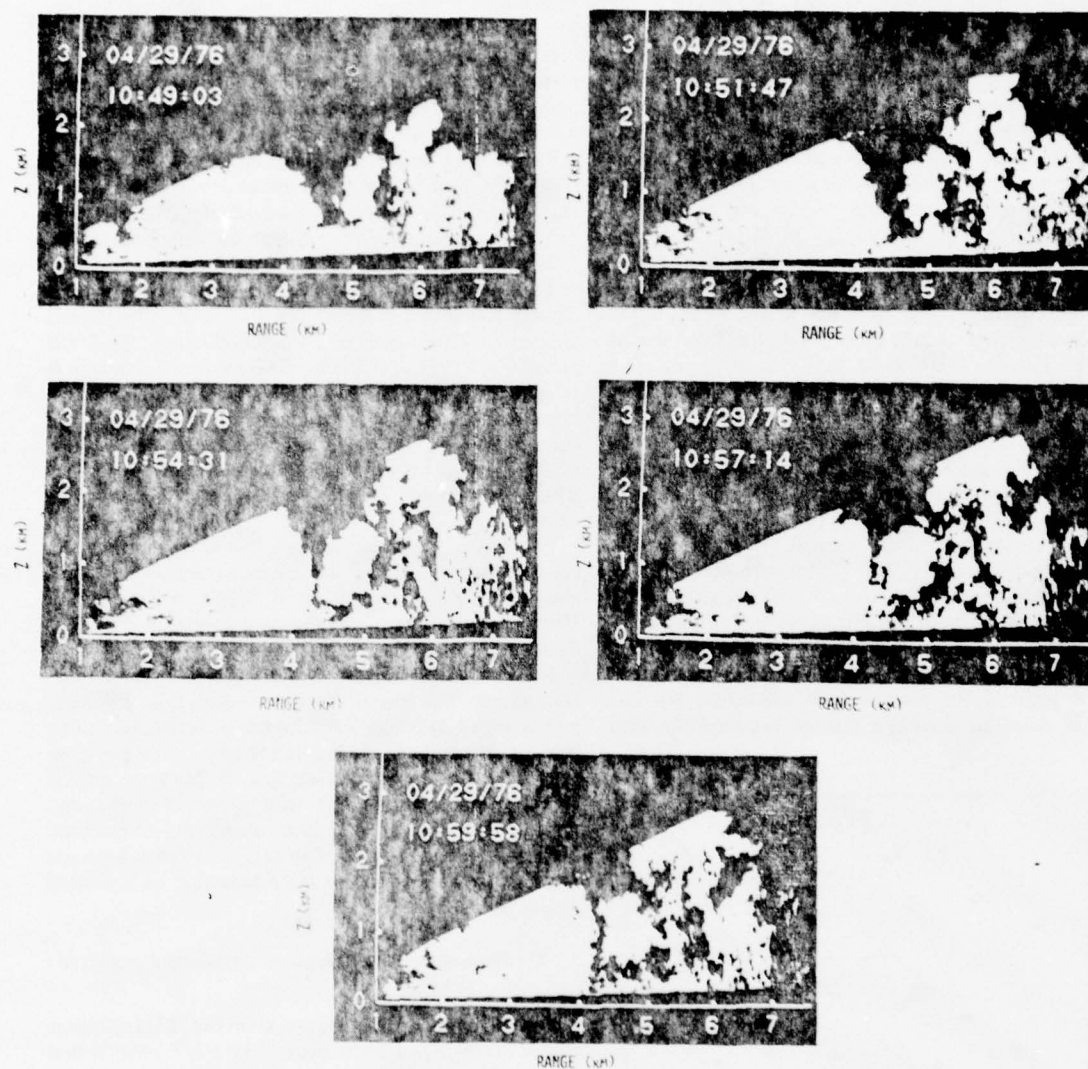


FIG. 4. Photographs of lidar range versus height displays showing the development of convective structure in a visually clear atmosphere on 29 April 1976. The white areas are those where aerosol density is somewhat greater than the ambient background. Observation times are shown in the figures. Notice the rapid development of the plume at a range of 6 km. Frames 4b-4e show a small cumulus cloud which has developed at the top of this plume in the time interval between frames 4a and 4b. The cloud quickly extinguishes the laser pulse causing a dark shadow at the upper right.

each vector is located at the position where the velocity was measured. These vectors indicate that most features are being advected slowly to the right in Fig. 5.

An interesting feature of the velocity field in Fig. 5 is that the strongest rising motion occurs on the upwind side of the cells. Aircraft and tower observations by Warner and Telford (1964, 1967), Lenschow (1970) and Kaimal and Businger (1970) indicate that the hottest part of a convective plume is on the upwind side. This is compatible with the present lidar observation. Since

the hottest part of the plume should coincide with the region of greatest vertical velocity. The compensating downdraft for both cells is considerably weaker and seems to occur preferentially on the downwind side of the cell. A model of a convective cell with rising motion upwind and sinking motion downwind is shown schematically in Fig. 6. This circulation has a sense of rotation about a horizontal axis perpendicular to the mean flow, suggesting that the rotational part of the circulation is dynamically driven by the shear flow.



FIG. 5. Wind vectors obtained from the displacement of plume structure in the 160 s time interval between frames 4a and 4b.

This type of circulation pattern has been observed by others in cumulus clouds (e.g., Byers, 1965, p. 178). The lidar data shows that this pattern exists before cloud formation has begun.

The observations of Fig. 4 also have implications for the parameterizations of vertical fluxes in convective boundary layers. Both cells shown in Fig. 4a have circulations which encompass nearly the entire depth of the boundary layer. The appropriate length scale of these vertical mixing processes must therefore be comparable to the inversion height z_i . Previous studies, e.g., Deardorff (1972) and Kaimal *et al.* (1976), have indicated that z_i is an important parameter in convective situations. The lidar depiction of convection gives visual support for this hypothesis.

Since typical vertical velocities in a convective field are around $0.1\text{--}1\text{ m s}^{-1}$, the vertical mixing of heat, momentum, water vapor, etc., is very rapid. In fact, vertical fluxes are probably entirely determined by the transport processes occurring in the viscous and surface

layers and by the rate of entrainment at the inversion. This is compatible with measurements of vertical profiles of wind and temperature which show that vertical gradients are weak or nonexistent in convective layers except near the top or bottom of the layer (see Clarke, 1970; Kaimal *et al.*, 1976).

Fig. 4 also visually illustrates the problems of using stationary *in situ* instruments to measure fluxes and other turbulence quantities in light wind convective situations. Over the entire period which these frames cover (~ 10 min), the convective cells have moved horizontally less than 0.5 km. Since the spacing between the two cells is about 3 km, an *in situ* sensor would sample about 1 cell h^{-1} . Any statistical description of the convective layer requires the sampling of many cells. But, during the morning when the boundary layer is evolving rapidly, the statistical description of the layer may change over the time period of 1 h. Obviously, an *in situ* sensor will fail to adequately describe the layer in such a situation.

6. Conclusions

These preliminary results indicate that a high spatial resolution lidar system with scanning capabilities is a powerful tool for the observation of the convective boundary layer. These lidar observations of convective motions show the following:

- 1) Convective plumes have roots near the surface. The lidar data indicate that the preferred form of convective cells are plumes rather than bubbles.
- 2) The observed plumes have a wide range of sizes, the majority having an aspect ratio between 0.5 and 1.5.
- 3) The lidar is able to observe circulation patterns in and around convective structures. These observations indicate that these cells have a maximum rising motion on the upwind side of the cell and sinking motion on the downwind side.

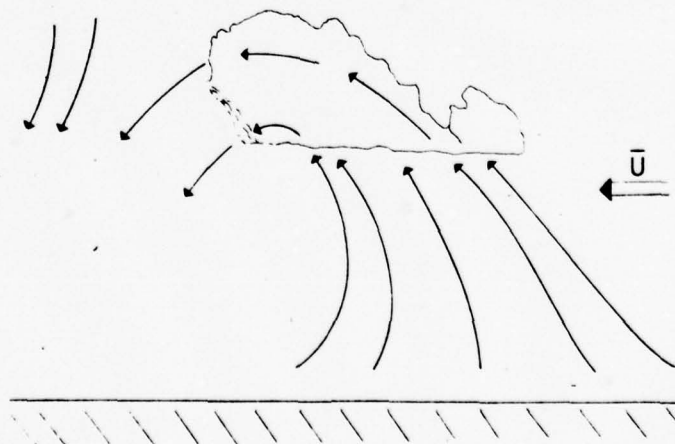


FIG. 6. Schematic view of the flow pattern observed around a developing fair weather cumulus cloud.

Acknowledgments. We would like to thank Professor James Weinman for his suggestions during the course of this work. This work was partially funded by USAROD grant DAAG29-76-C-0156. The senior author (Kunkel) was supported by a National Science Foundation fellowship during part of the work.

REFERENCES

- Byers, H. R., 1965: *Elements of Cloud Physics*. University of Chicago Press, 191 pp.
- Clarke, R. H., 1970: Observational studies in the atmospheric boundary layer. *Quart. J. Roy. Meteor. Soc.*, **96**, 91-114.
- Deardorff, J. W., 1972: Numerical investigations of neutral and unstable planetary boundary layers. *J. Atmos. Sci.*, **29**, 91-115.
- Hall, F. F., 1972: Temperature and wind structure studies by acoustic echo-sounding. *Remote Sensing of the Troposphere*, Govt. Printing Office, Chap. 18.
- Hardy, K. R., and H. Ottersten, 1969: Radar investigations of convective patterns in the clear atmosphere. *J. Atmos. Sci.*, **26**, 666-672.
- Kaimal, J. C., and J. A. Businger, 1970: Case studies of a convective plume and a dust devil. *J. Appl. Meteor.*, **9**, 612-620.
- , J. C. Wyngaard, D. A. Haugen, O. R. Coté, Y. Izumi, S. J. Caughey and C. J. Readings, 1976: Turbulence structure in the convective boundary layer. *J. Atmos. Sci.*, **33**, 2152-2169.
- Konrad, T. G., 1970: The dynamics of the convective process in clear air as seen by radar. *J. Atmos. Sci.*, **27**, 1138-1147.
- , and F. L. Robison, 1972: Simultaneous measurements of radar reflectivity and refractive index spectra in clear air convection. *J. Appl. Meteor.*, **11**, 1114-1119.
- , and —, 1973: Development and characteristics of free convection in the clear air as seen by radar and aircraft. *J. Appl. Meteor.*, **12**, 1284-1294.
- Kunkel, K. E., E. W. Eloranta and J. A. Weinman, 1975: Visualization of eddies in the planetary boundary layer by means of lidar. *Preprints Int. Conf. Environ. Sensing and Assessment*, Las Vegas, Amer. Meteor. Soc.
- Lenschow, D. H., 1970: Airplane measurements of planetary boundary layer structure. *J. Appl. Meteor.*, **9**, 874-884.
- Rowland, J. R., 1973: Intensive probing of a clear air convective field by radar and instrumented drone aircraft. *J. Appl. Meteor.*, **12**, 149-155.
- , 1976: Clear air convective behavior revealed by radar chaff. *J. Appl. Meteor.*, **15**, 521-526.
- Scorer, R. S., and F. H. Ludlam, 1953: Bubble theory of penetrative convection. *Quart. J. Roy. Meteor. Soc.*, **79**, 94-103.
- Smith, E., 1975: The McIDAS system. *IEEE Trans. Geosci. Electron.*, **GE-13**, No. 3.
- Telford, J. W., 1966: The convective mechanism in clear air. *J. Atmos. Sci.*, **23**, 652-666.
- , 1970: Convective plumes in a convective field. *J. Atmos. Sci.*, **27**, 347-358.
- , 1972: A plume theory for the convective field in clear air. *J. Atmos. Sci.*, **29**, 128-134.
- , 1975: The effect of compressibility and dissipation heating on boundary layer plumes. *J. Atmos. Sci.*, **32**, 108-115.
- , and J. Warner, 1964: Fluxes of heat and vapor in the lower atmosphere derived from aircraft observations. *J. Atmos. Sci.*, **21**, 539-548.
- Vulfson, N. L., 1961: *Convective Motions in a Free Atmosphere*. Moscow, Gidrometerizdat. [English translation from NTIS, Ref. No. OTS64-11017.]
- Warner, J., and J. W. Telford, 1963: Some patterns of convection in the lower atmosphere. *J. Atmos. Sci.*, **20**, 313-318.
- , and —, 1967: Convection below cloud base. *J. Atmos. Sci.*, **24**, 374-382.
- Willis, G. E., and J. W. Deardorff, 1976: Visual observations of horizontal planforms of penetrative convection. *Preprints Third Symp. Atmospheric Turbulence, Diffusion and Air Quality*, Raleigh, Amer. Meteor. Soc., 9-12.

APPENDIX C

Remote Determination of Boundary Layer Characteristics
from Lidar Measurements

K.E. Kunkel,⁽¹⁾⁽²⁾ E.W. Eloranta, and J.A. Weinman⁽³⁾

Department of Meteorology
University of Wisconsin
Madison, WI 53706

(1) Based on material submitted to satisfy the requirements for the
Ph.D. degree in Meteorology

(2) Now at White Sands Missile Range, N.M. 88002

(3) Now at Goddard Laboratory for Atmospheric Sciences, Greenbelt, MD 20771

Abstract

This study employs a scanning lidar system to remotely probe the atmospheric convective boundary layer. Aerosols present in the surface layer are carried aloft by convection, creating horizontal inhomogeneities in the aerosol concentration. These inhomogeneities can be detected with lidar and they serve as tracers allowing remote measurements of several boundary layer parameters. The data presented here were obtained over Madison, Wisconsin, over a three year period from 1975 to 1977.

The horizontally averaged variance of the range and energy corrected lidar signal return shows a monotonic increase with height, z , up to the inversion base. Variance spectra computed from lidar data agree with the shape of the wind velocity spectra which were parameterized by Kaimal et al. (1976). At high wavenumbers, the aerosol density spectra follow the $-5/3$ law. The peaks of the spectra occur at a wavelength of about $1.5 \times$ the boundary layer thickness.

Lidar data were used to measure the mean and the rms turbulent velocity components. The turbulent velocity measurements were combined with lidar measurements of the inversion height to calculate the energy dissipation. The results compared well with in situ anemometer measurements of these quantities.



Fig

1. Introduction

The measurement of meteorological parameters in convective boundary layers has been implemented with in situ sensors mounted on towers, airplanes, or balloons. Instruments on towers obtain only point measurements and they measure the lower part of the boundary layer. Airplanes and balloons are limited to line measurements of meteorological parameters. Remote sensors such as radar, sodar and lidar can scan large volumes of the planetary boundary layer in a much shorter time than is possible with in situ measurements.

This paper presents some preliminary results of remote measurements conducted with a lidar to yield the following meteorological parameters:

a) Spectra of aerosol density fluctuations: Porch and Gillette (1977), using nephelometer data taken at 6 m above the surface, showed that the spectrum of aerosol inhomogeneities was similar in shape to the horizontal wind speed spectrum. Kaimal et al. (1976) measured wind and temperature spectra in the convective boundary layer; his analysis yielded a series of universal curves for these spectra. This study presents spectra of lidar signal returns from aerosol density inhomogeneities which are compared with the universal curves of Kaimal et al.

b) Mean Wind Velocity and Fluctuations: A study by Eloranta et al. (1975) showed that lidar could be used to remotely measure the radial component of mean winds by tracking the motion of naturally occurring aerosol inhomogeneities. An extension of this technique is developed here to remotely measure radial and transverse components of the mean wind and the turbulent velocity fluctuation, \bar{u} , of the transverse wind component in the convective boundary layer.

c) Kinetic Energy Dissipation Rates: Doppler radar has been used to measure the kinetic energy dissipation rate, ϵ , see Gorelik and Mel'nechuk

(1963, 1968) Knyazev (1971), Frisch and Clifford (1974). More recently, Gaynor (1977) used sodar to obtain ϵ in the boundary layer. The present work will describe a technique whereby ϵ was measured with a lidar and the results are compared with in situ measurements obtained from an anemometer mounted on a tower.

2. Equipment Description

The University of Wisconsin lidar uses a ruby laser which emits 1 J pulses of .694 μm light with a maximum repetition rate of 1 Hz as the transmitter; a .31 m diameter telescope is employed as the receiver. The lidar has the capability to scan through both azimuth and elevation angles. An on-line PDP 11/40 computer controls the operation of the lidar and stores the data on magnetic tape. The lidar was operated over Madison, Wisconsin during numerous clear air situations between 1975 and 1977. To provide simultaneous independent measurements, a radio tower within the scanning sector of the lidar was instrumented at the 70 m level with a bivane to measure wind speed and direction. These data were transferred by telephone to the minicomputer and stored on magnetic tape. A more comprehensive description of the instrumentation appears in Kunkel's (1978) Ph.D. thesis.

3. Measurements and Analysis

3a) Spectral Density of the Variance of Aerosol Density Fluctuations

To a first approximation, the lidar signal return is proportional to the aerosol density; the variance of the returned signals therefore provides an estimate of the magnitude of aerosol density inhomogeneities which have been created by convection.

The data that were used for this study was restricted to regions below

the inversion where the aerosol inhomogeneities have been created by the convective field. The temporal variance, which was calculated at each point in an RHI cross-section, showed a monotonic increase with altitude above the lower third of the boundary layer. See Kunkel (1978) for a more detailed description of these measurements.

The lidar signals were subjected to a spectral analysis to derive variance spectra of the aerosol density fluctuations. A variance spectrum obtained from lidar data differs from traditional tower measurements in that it is essentially an instantaneous spatial spectrum rather than a temporal spectrum measured at a point.

The following computational scheme was used to obtain the power spectra: A mean lidar signal, averaged over many laser shots, $\bar{S}(R)$, was calculated as a function of range, R , from the returned power $P(R,j)$ corrected for variations in output energy E_o and the inverse range-squared attenuation, i.e. $\frac{R^2}{E_o} P(R,j)$. This was subtracted from the j^{th} individual signal return to produce a deviation return $S(R,j)$. The deviation return was also normalized by the average value of the mean return. Therefore

$$S(R,j) = \frac{\frac{R^2}{E_o} P(R,j) - \bar{S}(R)}{\frac{1}{L} \sum_{l=1}^L \bar{S}(R_l)} \quad (1)$$

where R_l and R_u are the limits on the range segment considered. Leakage was reduced by multiplying the deviation return by a data window $F(R)$ which produces a cosine taper on 10% of each end of the data segment as described by Bingham et al. (1967). $F(R)$ is defined as

$$F(R) = \begin{cases} \frac{1}{2} [1 - \cos 10\pi \frac{(R - R_1)}{(R_L - R_1)}] & R_1 \leq R < R_1 + .1(R_L - R_1) \\ 1 & R_1 + .1(R_L - R_1) \leq R \leq R_1 + .9(R_L - R_1) \\ \frac{1}{2} [1 - \cos 10\pi \frac{(R_L - R)}{(R_L - R_1)}] & R_1 + .9(R_L - R_1) < R \leq R_L \end{cases} \quad (2)$$

The resulting signal is

$$S'(R, j) = F(R) \cdot S(R, j) \quad (3)$$

A fast-Fourier transform algorithm was used to compute the Fourier coefficients. These coefficients were multiplied and added to obtain the variance spectrum, $\phi(k)$ as a function of wave number k , where

$$\overline{S'^2} = \int_0^\infty \phi(k) dk \quad (4)$$

The statistical uncertainty in the spectral estimates was minimized by averaging the spectra over a number of shots at the same angle.

Fig. 1 shows a representative aerosol density variance spectrum, $\phi(k)$, computed from data taken on Sept. 28, 1976. The data were obtained in the height interval of 130 m - 460 m. The inversion height, z_i , as measured by the lidar was 575 m. Superimposed on the graph is the universal curve of Kaimal et al. (1976) for the longitudinal wind component (solid curve). The shape of the aerosol density spectrum is quite similar to Kaimal's universal curve. The peak occurs at about the same location ($k \approx 4/z_i \approx .007 \text{ m}^{-1}$, equivalent to a wavelength of $\sim 1.5 z_i$). For $k > .02 \text{ m}^{-1}$, the aerosol density spectrum falls off with the 5/3 power. Fig. 1 also shows error bars which give the 90% confidence levels calculated using a chi-square analysis for Gaussian white noise described by Otnes and Enochson (1973). Other examples of such spectra are presented by Kunkel (1978).

3b) Mean Wind Velocity and Fluctuations

Leuthner and Eloranta (1977) used a lidar to measure mean wind speed and direction. Their technique involved scanning horizontally between two azimuth angles on days when the mean wind direction was approximately perpendicular to the laser axis. Typically the difference between the two azimuth angles was $1.0^\circ - 3.0^\circ$. Aerosol inhomogeneities which pass through the upwind direction were seen at the downwind direction at a time Δt later determined by the wind speed and at a range difference ΔR determined by the wind direction. To determine Δt and ΔR , a two-dimensional (range and time) lag cross-correlation was performed on a series of shots taken at the two angles.

This was defined as

$$C(I, J) = \frac{\sum_{l=l_1}^{l_2} \sum_{j=j_1}^{j_2} S'(R_{l+I}, j+J) \cdot S'(R_l, j)}{\left(\sum_{l=l_1}^{l_2} \sum_{j=j_1}^{j_2} S'^2(R_{l+I}, j+J) \right)^{1/2} \left(\sum_{l=l_1}^{l_2} \sum_{j=j_1}^{j_2} S'^2(R_l, j) \right)^{1/2}} \quad (5)$$

where $C(I, J)$ = average value of cross-correlation for range point lag I
and shot lag J

R_l = range of l th range interval

j = shot number

$S'(R_l, j)$ = deviation from mean lidar signal return. This has also been filtered to reject both very large and very small features.

Measurement of the lateral rms turbulent velocity was achieved by means of a three-angle scan. This scan is illustrated in Fig. 2. The lidar firing sequence is $\phi_1 - \phi_2 - \phi_3 - \phi_2 - \phi_1 - \phi_2$ -etc. An aerosol inhomogeneity detected at ϕ_1 will be detected at ϕ_2 at a shot lag J'_m and point lag I'_m . The inhomogeneity will be observed at ϕ_3 at shot lag J''_m and point lag I''_m . The

autocorrelation function $C(I,0)$ typically has a quasi-Gaussian shape as shown in Fig. 3. The mean square half-width of this function σ_0^2 can be defined as

$$\sigma_0^2 = (15 \text{ m})^2 \cdot \frac{\sum_{I=I_1}^{I_2} C(I,0) \cdot I^2}{\sum_{I=I_1}^{I_2} C(I,0)} \quad (6)$$

The cross-correlation function between shots at ϕ_1 and ϕ_2 , $C(I-I'_m, J'_m)$ shown in Fig. 3, has a broader shape. The half-width of this function σ_1^2 is defined as

$$\sigma_1^2 = (15 \text{ m})^2 \cdot \frac{\sum_{I=I_3}^{I_4} C(I-I'_m, J'_m) \cdot I^2}{\sum_{I=I_3}^{I_4} C(I-I'_m, J'_m)} \quad (7)$$

The cross-correlation function between shots at ϕ_1 and ϕ_3 at shot lag J''_m , $C(I-I''_m, J''_m)$ has an even broader shape as is shown in Fig. 3. The half-width of this function σ_2^2 is defined as

$$\sigma_2^2 = (15 \text{ m})^2 \cdot \frac{\sum_{I=I_5}^{I_6} C(I-I''_m, J''_m) \cdot I^2}{\sum_{I=I_5}^{I_6} C(I-I''_m, J''_m)} \quad (8)$$

The broadening of the cross-correlation functions is caused by two effects. First, the individual aerosol inhomogeneities will diffuse due to small scale turbulence as they are advected downwind. Second, the cross-correlation is averaged over a number of shots and a number of inhomogeneities will move through the scanning region during this time. Because of

the turbulent nature of the wind, the wind direction will continually fluctuate so that the point lag at which the cross-correlation is a maximum changes from one inhomogeneity to the next. Csanady (1973) showed that the mean square displacement σ_y^2 of an ensemble of independently diffusing particles in the y-direction is given by

$$\sigma_y^2 = \bar{\sigma}^2 t^2 \quad (9)$$

for values of t which are short compared to the Lagrangian time scale. The rms turbulent velocity is assumed to be isotropic, designated by $\bar{\sigma}$. If the autocorrelation and cross-correlation functions are viewed as probability distributions of particles about a mean position, Eq. (9) can be used to relate the spread of the correlation functions with time to the rms turbulent velocity $\bar{\sigma}$ in the lidar axis direction. This relation is satisfied by

$$\bar{\sigma} = (\sigma_1^2 - \sigma_0^2)^{1/2} / t_1 \quad (10)$$

where t_1 is now the time of transit from ϕ_0 to ϕ_1 . Since typical values of t_1 are 5 to 25 s while Lagrangian correlation times in the atmosphere are of the order of 100 s, Eq. (9) should be valid.

An analysis using Gaussian-shaped inhomogeneities is given in the Appendix. An expression was obtained relating the magnitude and shape of the cross-correlation function as a function of the rms isotropic turbulent velocity and of the size of the inhomogeneities. It is shown in Eq. (A.5) that:

$$C(\Delta X, \Delta y, t) = \frac{(\pi)^{3/2} \bar{\sigma}^2 e^{-\Delta y^2 / 4(\bar{\sigma}^2 + \frac{1}{2} t^2 \bar{\sigma}^2)} - (\Delta X - \bar{U}t)^2 / 4(\bar{\sigma}^2 + \frac{1}{2} t^2 \bar{\sigma}^2)}{(\bar{\sigma}^2 + \frac{1}{2} t^2 \bar{\sigma}^2)^{3/2}} \quad (11)$$

and from Eq. (A.9) it is evident that Eq. (10) is also appropriate.

-8-

The effects of noise on the correlation functions can be seen by letting the deviation profile, $S'(R_\ell, j)$, be the sum of a signal component $\hat{S}(R_\ell, j)$ and a noise component $N(R_\ell, j)$, i.e.,

$$S'(R_\ell, j) = \hat{S}(R_\ell, j) + N(R_\ell, j) \quad (12)$$

The correlation function is then given by

$$C(I, J) = \frac{\sum_{\ell=\ell_1}^{\ell_2} \sum_{j=j_1}^{j_2} [\hat{S}(R_\ell, j) + N(R_\ell, j)] [\hat{S}(R_{\ell+I}, j+J) + N(R_{\ell+I}, j+J)]}{[\sum_{\ell=\ell_1}^{\ell_2} \sum_{j=j_1}^{j_2} S'^2(R_\ell, j)]^{1/2} [\sum_{\ell=\ell_1}^{\ell_2} \sum_{j=j_1}^{j_2} S'^2(R_{\ell+I}, j+J)]^{1/2}} \quad (13)$$

Letting

$$\rho_{I,J}^{'2} = \frac{1}{(\ell_2 - \ell_1)(j_2 - j_1)} \left[\sum_{\ell=\ell_1}^{\ell_2} \sum_{j=j_1}^{j_2} S'^2(R_\ell, j) \right]^{1/2} \left[\sum_{\ell=\ell_1}^{\ell_2} \sum_{j=j_1}^{j_2} S'^2(R_{\ell+I}, j+J) \right]^{1/2} \quad (14)$$

and

$$\hat{C}_S(I, J) = \frac{1}{(\ell_2 - \ell_1)(j_2 - j_1)} \sum_{\ell=\ell_1}^{\ell_2} \sum_{j=j_1}^{j_2} \hat{S}(R_\ell, j) \cdot \hat{S}(R_{\ell+I}, j+J) \quad (15)$$

$$\hat{C}_N(I, J) = \frac{1}{(\ell_2 - \ell_1)(j_2 - j_1)} \sum_{\ell=\ell_1}^{\ell_2} \sum_{j=j_1}^{j_2} N(R_\ell, j) \cdot N(R_{\ell+I}, j+J) \quad (16)$$

and assuming that the signal and the noise are not correlated so that the cross terms will be zero, the expression becomes

$$C(I, J) = \frac{\hat{C}_S(I, J)}{\rho_{I,J}^{'2}} + \frac{\hat{C}_N(I, J)}{\rho_{I,J}^{'2}} \quad (17)$$

For different shots, the noise is assumed to be uncorrelated, i.e.,

$$\hat{C}_N(I, J) = 0 \text{ for } J \neq 0 \quad (18)$$

Therefore, the cross-correlation function is given by

$$C(I, J) = \hat{C}_S(I, J) / \overline{\rho_{I, J}^2} \quad (19)$$

while the autocorrelation function is

$$C(I, 0) = [\hat{C}_S(I, 0) + \hat{C}_N(I, 0)] / \overline{\rho_{I, J}^2} \quad (20)$$

This provides a means of removing many of the noise problems. Eq. (10)

implies that

$$\sigma_1^2 = \sigma_0^2 + \bar{\sigma}^2 t_1^2 \quad (21)$$

and

$$\sigma_2^2 = \sigma_0^2 + \bar{\sigma}^2 t_2^2 \quad (22)$$

Eqs. (21) and (22) give

$$\bar{\sigma} = \left[\frac{\sigma_2^2 - \sigma_1^2}{t_2^2 - t_1^2} \right]^{1/2} \quad (23)$$

Since σ_2^2 and σ_1^2 are both calculated from cross-correlation functions,

Eq. (23) states that the noise is effectively eliminated so that Eq. (23) may be used to calculate $\bar{\sigma}$.

The elimination of the noise in the cross-correlation function also allows the calculation of the signal-to-noise ratio. This is done by taking

the limit of the cross-correlation function for shots at the same angle as J approaches 0, i.e.,

$$\lim_{J \rightarrow 0} C(I, J) = \hat{C}_S(I, 0) \quad (24)$$

This gives the signal component for zero shot lag, which can be divided by the autocorrelation function, to give

$$\frac{\lim_{J \rightarrow 0} C(I, J)}{C(I, 0)} = \left[1 + \frac{\hat{C}_N(I, 0)}{\hat{C}_S(I, 0)} \right]^{-1} \quad (25)$$

Since the correlation functions are proportional to the square of the signal, the expression becomes

$$\frac{\lim_{J \rightarrow 0} C(I, J)}{C(I, 0)} = (1 + N^2/S^2)^{-1} \quad (26)$$

or

$$S/N = \left[\frac{C(I, 0)}{\lim_{J \rightarrow 0} C(I, J)} - 1 \right]^{-\frac{1}{2}} \quad (27)$$

For a point lag $I = 0$, the autocorrelation function $C(0, 0)$ is identically 1 and the final expression becomes

$$S/N = \left[\frac{1}{\lim_{J \rightarrow 0} C(0, J)} - 1 \right]^{-\frac{1}{2}} \quad (28)$$

The signal-to-noise ratios were obtained by calculating the cross-correlation function for shots at the same angle. The peak value of the cross-correlation at shot lag J increases as J approaches zero. The peak values were plotted and extrapolated to zero shot lag. The zero-extrapolated value was then used in Eq. (28) to obtain the signal-to-noise ratio.

In their measurements of the mean wind, Leuthner and Eloranta (1977) used the maximum value of the cross-correlation to determine the shot lag J_m and therefore the time interval for aerosol inhomogeneities to move from one angle to the other. This method can introduce some error in the measurements because turbulence in the boundary layer will cause the maximum cross-correlation to decrease with time as shown by the analysis in the Appendix. The maximum cross-correlation can then occur at a smaller shot lag (i.e., shorter time lag) than that indicated by the mean wind speed. To avoid this difficulty, Eq. (11) was fitted to the measured cross-correlation values by minimizing the least squares residue to obtain an optimum value of \bar{U} . This optimum value of \bar{U} was used to determine the shot lag at which $\bar{\sigma}$ was then computed. This quantity was initially computed at the shot lag at which the cross-correlation was a maximum. A value of \bar{U} was obtained and a shot lag was determined from \bar{U} . A new value of $\bar{\sigma}$ was then computed. This process was repeated until the shot lag at which the cross-correlation was a maximum no longer changed.

In performing these calculations, care was taken to exclude range intervals that included persistent and sharp increases or decreases in signal return which were either caused by a large scale feature such as an inversion base or a smaller feature that was not wholly contained in the range interval. Such features produced $\bar{\sigma}$ values that were too low.

Lidar data was used to compute $\bar{\sigma}$ using Eq. (23). Table 1 shows a comparison of these results with simultaneous tower mounted anemometer measurements of $\bar{\sigma}$. The tabulated values are arranged according to decreasing values of the signal-to-noise ratio, S/N. The table also gives the stability category of Pasquill (1961); (determined from the mean wind speed and an estimate of stability conditions), the mean wind speed measured at the tower, the mean wind speed determined by fitting Eq. (11) to cross-correlation values, the

Table 1

Comparison of $\tilde{\sigma}$ and \bar{U} obtained both by lidar and by a tower mounted bivane (anemometer). The quantities derived from lidar measurements were determined by fitting Eq. (11) to lidar cross-correlation values. The signal-to-noise ratio, S/N, the Pasquill stability category, the averaging time over which $\tilde{\sigma}$ and \bar{U} were determined, and the date are also given.

$\tilde{\sigma}$ (lidar) (m/s)	$\tilde{\sigma}$ (anemometer) (m/s)	\bar{U} (lidar) (m/s)	\bar{U} (anemometer) (m/s)	S/N	Pasquill stability category	averaging time (sec)	date
.98 ± .14	.92 ± .08	7.5 ± 1.0	6.7 ± .5	2.7	D	700	6/20/77
1.27 ± .23	1.02 ± .10	7.2 ± 1.0	6.8 ± .6	2.6	D	700	6/20/77
.70 ± .11	.74 ± .07	4.3 ± .4	4.6 ± .3	1.7	C	700	5/23/77
.84 ± .08	.90 ± .10	4.9 ± .4	4.4 ± .5	1.5	B	700	6/27/77
.99 ± .03	.35 ± .06	2.6 ± .2	2.1 ± .1	1.5	A	700	7/26/77
2.08 ± .32	.93 ± .07	5.3 ± .8	6.6 ± .5	.9	C	700	6/23/77
.70 ± .11	1.02 ± .09	8.6 ± 1.0	8.3 ± .6	.8	D	740	4/22/77
1.35 ± .21	1.39 ± .18	9.0 ± .8	7.7 ± 1.0	.7	D	740	4/22/77
1.62 ± .25	1.11 ± .10	7.6 ± 1.1	8.5 ± .7	.7	D	740	4/22/77

averaging time over which $\bar{\sigma}$ was determined, and the date. The uncertainties shown for $\bar{\sigma}$ (lidar) and \bar{U} (lidar) are mainly due to differences in the volume sampled i.e. the lidar samples an extended volume while the anemometer measures the atmosphere which advects past the instrument. The table shows that the lidar measurements of $\bar{\sigma}$ compare quite well with the anemometer measurements for signal-to-noise ratios greater than one. As the signal-to-noise ratio decreases, the technique becomes less reliable.

3c) Kinetic Energy Dissipation Rates

The lidar measurements of $\bar{\sigma}$ can be used to make estimates of the energy dissipation rate ϵ . Fig. 3 of Kaimal et al. (1976) shows that velocity spectra normalized by $(\epsilon z_1)^{2/3}$ plotted as a function of the non-dimensional frequency

$$v_n = v z_1 / \bar{U} \quad (29)$$

fall into a single region of the graph.

The velocity spectrum $\phi_v(v)$ is defined such that

$$\int_{v_a}^{\infty} \phi_v(v) dv = \bar{\sigma}^2 \quad (30)$$

where $v_a = t_a^{-1}$ and t_a is the averaging time over which $\bar{\sigma}$ is calculated.

Nothing is changed by expressing the integral in the following way

$$\int_{v_a}^{\infty} \phi_v(v) dv = (\epsilon z_1)^{2/3} \int_{v_a}^{\infty} \left| \frac{v \phi_v(v)}{(\epsilon z_1)^{2/3}} \right| \frac{dv}{v} \quad (31)$$

The function in brackets in the integral on the right side of Eq. (31) is plotted in Fig. 3 of Kaimal et al. (1976). Noting that $dv/v = dv_n/v_n$, Eqs. (30) and (31) can be combined and rearranged to give

$$\epsilon = \bar{\sigma}^3 \bar{z}_i^{-1} \left\{ \int_{v_{na}}^{\infty} \left| \frac{v \phi_v(v)}{(\epsilon \bar{z}_i)^{2/3}} \right| \frac{dv}{v_n} \right\}^{-3/2} \quad (32)$$

where $v_{na} = v_a \bar{z}_i / \bar{U}$. \bar{U} , $\bar{\sigma}$ and \bar{z}_i can all be obtained from lidar measurements so that ϵ can be obtained from such remote measurements.

Eq. (32) was used to calculate ϵ for the entries in Table 2 where the signal-to-noise ratio is greater than one. Table 2 shows these results. Since Fig. 3 of Kaimal et al. (1976) represents the velocity-spectrum as a region rather than a single curve, the integral in Eq. (32) was computed for both the lower and upper bounds on the region in which the spectra should fall. Table 2 then gives the limiting values of ϵ from lidar data using the limiting values of the integral. Lidar data was used to obtain \bar{z}_i on all days except on June 20, 1977. On that day, the lidar was operated at an elevation angle which was too low to see the inversion base. Since Section 3a showed that lidar spectra follow Kaimal's universal curves which depend on \bar{z}_i , lidar spectra were computed and these were used to estimate \bar{z}_i . The uncertainties in the lidar measurements of ϵ shown in the table are calculated from estimated errors in the measurement of $\bar{\sigma}$ and \bar{z}_i . Also given in Table 2 are independent estimates of ϵ from tower data taken at the same time. These were obtained by computing the spectra of the wind components and using the inertial subrange relationship

$$\phi(k) = D \epsilon^{2/3} k^{-5/3} \quad (33)$$

to compute ϵ . The constant D has been measured by Kaimal et al. (1972) who give a value of $0.50 \pm .05$ for the longitudinal component and a factor $4/3$ higher for the transverse and vertical components. The spectrum of each component was used to calculate ϵ and the range of values obtained is shown in the table. The uncertainties in the anemometer measurements of ϵ are

Table 2

Comparison of energy dissipation rate ϵ measured by means of lidar and anemometer. A range of values is given for both ϵ (anemometer) and ϵ (lidar). Uncertainties are given for these values. z_1 measured by the lidar is also listed. The values of $\bar{\sigma}$ and \bar{U} which were used in Eq. (32) are presented in Table 1.

ϵ (lidar) ($10^{-2} \text{ m}^2/\text{s}^3$)		ϵ (anemometer) ($10^{-2} \text{ m}^2/\text{s}^3$)		z_1	Date
min	max	min	max		
1.3 \pm .8	2.3 \pm 1.4	1.3 \pm .3	2.5 \pm .7	350	6/20/77*
2.7 \pm 1.7	4.9 \pm 3.1	1.4 \pm .4	2.7 \pm .7	350	6/20/77*
.7 \pm .2	1.3 \pm .4	.6 \pm .2	1.1 \pm .3	170	5/23/77
.6 \pm .2	1.3 \pm .4	.5 \pm .2	1.4 \pm .4	300	6/27/77
.13 \pm .03	.27 \pm .06	.07 \pm .02	.20 \pm .06	150	7/26/77

* z_1 was not available from lidar data, so lidar spectra were used to estimate z_1 .

-16-

due to uncertainties in the estimation of spectral levels ($\sim 15\%$) and uncertainties in the determination of the constant D . The table also gives the lidar measurements of z_1 .

The agreement between the lidar and anemometer measurements is satisfactory for all cases except the second entry from June 20, 1977. The source of the disagreement in this entry is primarily due to the 25% difference between the anemometer and lidar determinations of $\bar{\sigma}$ shown in Table 1. Because ϵ is proportional to the cube of $\bar{\sigma}$, ϵ is quite sensitive to uncertainties in the determination of $\bar{\sigma}$.

The accuracy of the $\bar{\sigma}$ determined with the current lidar system, is limited by the repetition rate of the laser. As lasers with higher repetition become available, the uncertainties in $\bar{\sigma}$ can be reduced accordingly. The signal-to-noise ratio of the lidar system also limits the accuracy of the $\bar{\sigma}$ determination; future technical developments can be expected to improve this ratio. Improvements in these two areas should allow remote lidar determinations of ϵ in the convective boundary layer to be applied to a wider variety of situations.

4. Summary

The presence of inhomogeneities in the aerosol concentration within the convective boundary layer has been utilized to derive several atmospheric boundary layer parameters from lidar measurements. The variance of the inhomogeneities was found to increase with height. Spectra have been computed from variances in the lidar returns and these show that aerosol spectra are similar to the curves given by Kaimal et al. (1976). A three-angle azimuth scan was employed to measure the mean wind and the rms value of the turbulent wind velocity. Agreement between the lidar measurements and simultaneous

in situ anemometer measurements was good, provided that the signal-to-noise ratios were sufficiently large. The lidar determination of the rms value of the wind and the inversion height were used to make remote measurements of the energy dissipation rate; these compared favorably with the energy dissipation rates measured in situ by anemometers.

5. Summary of Symbols

$A(\Delta y)$	autocorrelation function of Gaussian shaped inhomogeneities in Appendix.
B	amplitude factor for Gaussian shaped aerosol inhomogeneities in Appendix.
$C(I,J)$	cross-correlation at point lag I and shot lag J .
$\hat{C}_S(I,J)$	covariance of $S(R_l, j)$ for point lag I and shot lag J .
$\hat{C}_N(I,J)$	covariance of $N(R_l, j)$ for point lag I and shot lag J .
D	spectral constant.
E_o	lidar output energy.
ϵ	energy dissipation rate.
$F(R)$	cosine taper function.
G	Gaussian probability distribution of velocity fluctuations in Appendix.
I_m	point lag for which $C(I,J)$ is a maximum.
j	lidar shot index.
J_m	shot lag for which $C(I,J)$ is a maximum.
k	wavenumber.
λ	wavelength.
l	range point index.
$N(R_l, j)$	noise contribution to deviation profile $S(R_l, j)$.

- 15 -

$P(R, j)$ lidar power return as function of range R and shot number j .
 ϕ azimuth angle of lidar.
 $\Phi(k)$ spectral variance estimate as functions of wavenumber k .
 \dot{q}_i velocity components ($i = 1$ for u , $i = 2$ for v , and $i = 3$ for w) in Appendix.
 R range from lidar.
 R_ℓ ℓ 'th discrete range interval
 $\bar{S}(R)$ average value of corrected lidar signal at range R .
 $S(R, j)$ deviation profile of lidar signal return normalized by range average $\bar{S}(R)$.
 $S'(R, j)$ product of $S(R_\ell, j)$ and $F(R_\ell)$.
 $\hat{S}(R, j)$ deviation profile after noise contribution has been subtracted.
 S/N signal-to-noise ratio of lidar signal.
 $\hat{\sigma}$ rms width of Gaussian inhomogeneities in Appendix.
 σ_i^2 mean square half-width of correlation function $i = 0$ is autocorrelation function, $i = 1$ is cross-correlation function between outside and middle angles, and $i = 2$ is cross-correlation between outside angles.
 $\tilde{\sigma}$ rms velocity of velocity components.
 t time.
 t_a averaging time over which velocity variance is calculated.
 u deviation from the mean wind speed of the component of the wind along the mean wind direction.
 \bar{U} mean wind speed.
 v horizontal wind component perpendicular to mean wind direction.
 ν frequency.
 ν_a lowest frequency contributing to variance, i.e., $\nu_a = t_a^{-1}$.
 ν_n non-dimensional frequency = $\nu z_1 / U$.

w vertical wind component.
 x spatial coordinate oriented along mean wind direction.
 Δx distance between lidar azimuth angles.
 y spatial coordinate oriented horizontally and at a right angle
to mean wind direction.
 Δy $y_1 - y_0$
 y_i spatial coordinate parallel to lidar azimuth direction. $i = 0$
refers to upwind angle and $i = 1$ refers to downwind angle.
 z vertical coordinate.
 z_1 height of inversion base.

Acknowledgments:

We would like to thank Dr. S.T. Shipley and Mr. J.T. Sroga for their assistance in conducting various phases of this program. Funds to support this study were provided by the U.S. Army Research Office-Durham under grant USAROD #DAAG29-76-C-0156. We would like to thank this agency for its support.

APPENDIX TURBULENT VELOCITY DERIVATION USING GAUSSIAN SHAPED
AEROSOL INHOMOGENEITIES

For the purpose of this analysis, the aerosol inhomogeneities are assumed to be isotropically Gaussian in shape as a simple approximation with dimensions $\hat{\sigma}_x = \hat{\sigma}_y = \hat{\sigma}_z = \hat{\sigma}$ in all directions. The inhomogeneities are assumed to drift with the wind at velocities u , v and w .

$$S'(x,y,z,u,v,w,t) = B \cdot \exp\left[-((x-ut)^2 + (y-vt)^2 + (z-wt)^2)/2\hat{\sigma}^2\right] \quad (A.1)$$

where B is an amplitude factor. The velocity fluctuations are assumed to also have Gaussian distributions. The probability distributions G of $u-\bar{U}$, v and w are given by

$$G(\dot{q}_i) = \frac{\sqrt{2\pi}}{\tilde{\sigma}} e^{-\dot{q}_i^2/2\tilde{\sigma}^2} \quad (A.2)$$

where

$$\dot{q}_1 = u - \bar{U}, \dot{q}_2 = v, \dot{q}_3 = w$$

and $\tilde{\sigma}$ characterizes all of the turbulent velocity components. Fig. 5 shows the configuration which is analyzed. ΔX is the distance from ϕ_0 to ϕ_1 . \bar{U} is the mean wind speed, and $\Delta y = y_1 - y_0$. The cross-correlation C between shots at ϕ_0 to ϕ_1 is given by

$$C(\Delta x, \Delta y, t) =$$

$$\int_{-\infty}^{\infty} \int_{-\infty}^{\infty} \int_{-\infty}^{\infty} \int_{-\infty}^{\infty} \int_{-\infty}^{\infty} \int_{-\infty}^{\infty} S'(x,y,z,0) S'(x+\Delta x, y+\Delta y, z, t) G(u) G(w) du dx dv dy dw dz \quad (A.3)$$

$$\begin{aligned}
C(\Delta x, \Delta y, t) &= \frac{B^2}{(2\pi)^{3/2} \bar{\sigma}^3} \\
&\int_{-\infty}^{\infty} \int_{-\infty}^{\infty} \int_{-\infty}^{\infty} \int_{-\infty}^{\infty} \int_{-\infty}^{\infty} \int_{-\infty}^{\infty} \exp(-x^2/2\hat{\sigma}^2 - y^2/2\hat{\sigma}^2 - z^2/2\hat{\sigma}^2) \\
&\exp((x+\Delta x - \bar{u}t - ut)^2/2\hat{\sigma}^2 + (y+\Delta y - vt)^2/2\hat{\sigma}^2 + (z-wt)^2/2\hat{\sigma}^2) \\
&\exp(-u^2/2\bar{\sigma}^2 - v^2/2\bar{\sigma}^2 - w^2/2\bar{\sigma}^2) du dx dv dy dw dz
\end{aligned} \tag{A.4}$$

Integrating Eq. (A.4) yields

$$\begin{aligned}
C(\Delta x, \Delta y, t) &= \\
&\frac{(\pi)^{3/2} B^2 \bar{\sigma}^6 e^{-\Delta y^2/4(\hat{\sigma}^2 + \frac{1}{2}t^2\bar{\sigma}^2)} e^{-(\Delta x - \bar{u}t)^2/4(\hat{\sigma}^2 + \frac{1}{2}t^2\bar{\sigma}^2)}}{(\hat{\sigma}^2 + \frac{1}{2}t^2\bar{\sigma}^2)^{3/2}}
\end{aligned} \tag{A.5}$$

The mean square half-width of this function can be calculated from Eq. (7).

$$\begin{aligned}
\sigma_1^2 &= \frac{\int_{-\infty}^{\infty} (\Delta y)^2 C(\Delta x, \Delta y) d(\Delta y)}{\int_{-\infty}^{\infty} C(\Delta x, \Delta y) d(\Delta y)} \\
&= \frac{\int_{-\infty}^{\infty} (\Delta y)^2 e^{-y^2/4(\hat{\sigma}^2 + \frac{1}{2}t^2\bar{\sigma}^2)} d(\Delta y)}{\int_{-\infty}^{\infty} e^{-y^2/4(\hat{\sigma}^2 + \frac{1}{2}t^2\bar{\sigma}^2)} d(\Delta y)} \\
&= 2\hat{\sigma}^2 + \bar{\sigma}^2 t^2
\end{aligned} \tag{A.6}$$

The autocorrelation function $A(\Delta y)$, which is equivalent to $C(\Delta x, y)$ from (A.6) calculated at $\Delta x = 0$ and $t = 0$, is given by

$$A(\Delta y) = (\pi)^{3/2} B^2 \hat{\sigma}^3 e^{-\Delta y^2 / 4\hat{\sigma}^2} \quad (\text{A.7})$$

The mean square half-width of this function is

$$\begin{aligned} \sigma_0^2 &= \frac{\int_{-\infty}^{\infty} (\Delta y)^2 e^{-\Delta y^2 / 4\hat{\sigma}^2} d(\Delta y)}{\int_{-\infty}^{\infty} e^{-\Delta y^2 / \hat{\sigma}^2} d(\Delta y)} \\ &= 2\hat{\sigma}^2 \end{aligned} \quad (\text{A.8})$$

Combining (A.6) and (A.8) gives

$$\bar{\sigma} = (\sigma_1^2 - \sigma_0^2)^{1/2} / t \quad (\text{A.9})$$

This expression is presented as Eq. (9).

References

- Bingham, C., M.D. Godfrey, and J.W. Tukey (1967). Modern Techniques of Power Spectrum Estimation. IEEE Trans. on Audio and Electroacoustics, AU-15, 56-66.
- Csanady, G.T. (1973). Turbulent Diffusion in the Environment. D. Reidel Publishing Co., Boston, 248 pp.
- Eloranta, E.W., J.M. King and J.A. Weinman (1975). The Determination of Wind Speeds in the Boundary Layer by Monostatic Lidar. J. Appl. Meteor., 14, 1485-1489.
- Frisch, A.S. and S.F. Clifford (1974). A Study of Convection Capped by a Stable Layer Using Doppler Radar and Acoustic Echo Sounders. J. Atmos. Sci., 31, 1622-1628.
- Gaynor, J.E. (1977). Acoustic Doppler Measurement of Atmospheric Boundary Layer Velocity Structure Functions and Energy Dissipation Rates. J. Appl. Meteor., 16, 148-155.
- Gorelik, A.G. and Yu. V. Mel'nechuk (1963). Radar Study of Dynamic Processes in the Atmosphere. Tr. Vses. Nauchno Meteor., No. 5 [Amer. Meteor. Soc. Trans. T-R-667, 12 pp.]
- _____, and _____, (1968). A New Method for Measuring Dissipation Rate of Turbulence in Clouds and Precipitation Using Conventional Radar. Proc. Third All-Union USSR Radar Meteor. Conf., 150-156.
- Kaimal, J.C., J.C. Wyngaard, Y. Izumi, and O.R. Cote (1972). Spectral Characteristics of Surface Layer Turbulence. Quart. J. Roy. Meteor. Soc., 98, 563-589.
- Kaimal, J.C., J.C. Wyngaard, D.A. Haugen, O.R. Cote, and Y. Izumi (1976). Turbulence Structure in the Convective Boundary Layer. J. Atmos. Sci., 33, 2152-2169.
- Knyazev, L.V. (1971). Determination of the Rate of Dissipation of Turbulent Energy from Radar Data. Izv. Atmos. Oceanic Phys., 7, 1201-1205.
- Kunkel, K.E. (1978). Measurement of Upper Convective Boundary Layer Parameters by Means of Lidar, Ph.D. Thesis, Dept. of Meteorology, Univ. of Wisconsin, Madison, WI. Available through University Microfilms, Ann Arbor, Mich.
- Leuthner, T.G. and E.W. Eloranta (1977). Remote Measurement of Longitudinal and Cross Path Wind Velocities with a Monostatic Lidar. Presented at 8th International Laser Radar Conference, Philadelphia, Pa., June 6-9.
- Otnes, R.K. and L. Enochson (1972). Digital Time Series Analysis. John Wiley and Sons, New York, 467 pp.
- Pasquill, F. (1961). The Estimation of the Dispersion of Windborne Material. Meteor. Mag., 90, 33-49.
- Perch, W.M. and D.A. Gillette (1977). A Comparison of Aerosol and Momentum Mixing in Dust Storms Using Fast Response Instruments. J. Appl. Meteor., 16, 1273-1281.

Figure Captions

Fig. 1. Variance estimates $\phi(k)$ as a function of wavenumber, k , computed from lidar data taken on Sept. 28, 1976 at 1000 CDT. The smooth solid line is the idealized spectrum as given by Kaimal et al. (1976). Error bars show uncertainties given by chi-square analysis assuming lidar shots are uncorrelated. $\bar{U} = 1.9$ m/s, $z_1 = 575$ m, and $132 \text{ m} < z < 458 \text{ m}$.

Fig. 2. Schematic diagram showing the three-angle scan for measuring horizontal winds. ϕ_1 , ϕ_2 , and ϕ_3 are the azimuth angles at which the lidar fires. Aerosol inhomogeneities which are advected to the right by the mean wind \bar{U} will be first detected at ϕ_1 , then at ϕ_2 , and finally at ϕ_3 .

Fig. 3. Typical shapes for the correlation functions obtained from the three-angle scan. $C(I,0)$ is the autocorrelation function. $C(I-I'_m, J'_m)$ is the cross-correlation function between the outside and middle azimuth angles (i.e., ϕ_1 and ϕ_2 in Fig. 2) at the shot lag J'_m at which the function has its maximum value. $C(I-I''_m, J''_m)$ is the cross-correlation function between the outside azimuth angles (i.e., ϕ_1 and ϕ_3 in Fig. 2) at the shot lag at which the function has its maximum value.

Fig. 4. Geometry used for Gaussian cross-correlation analysis.

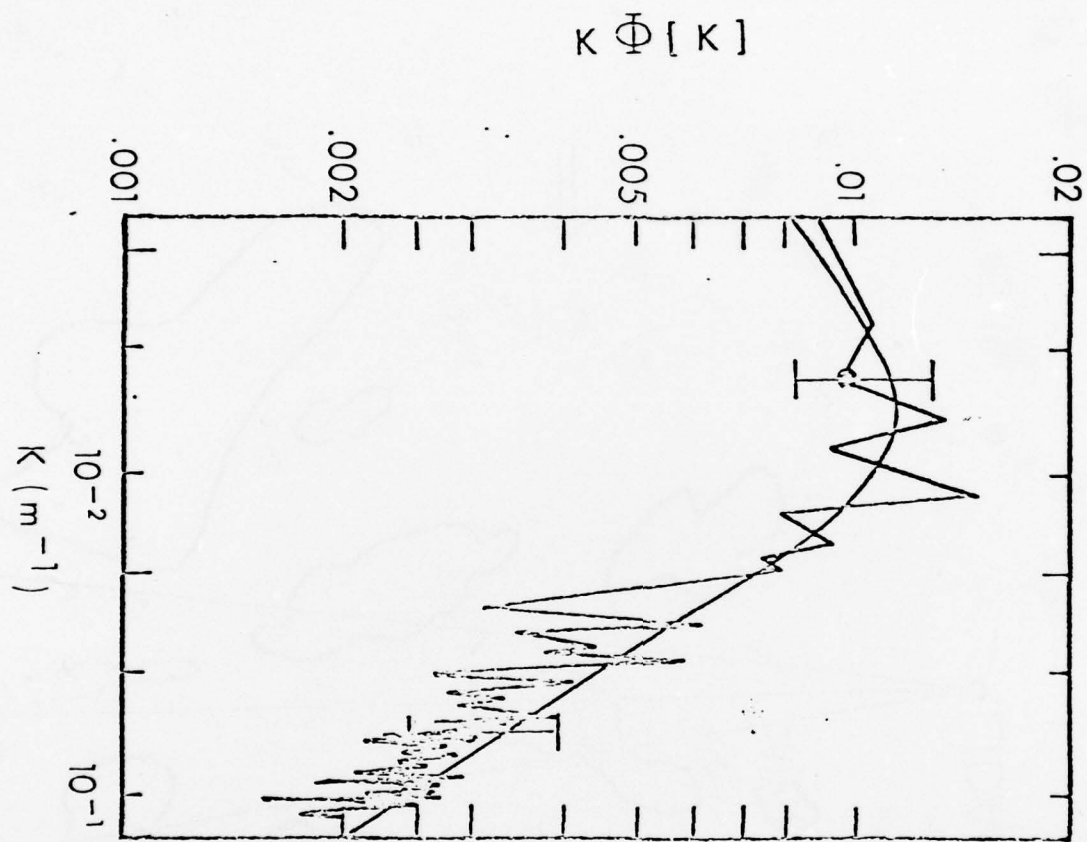
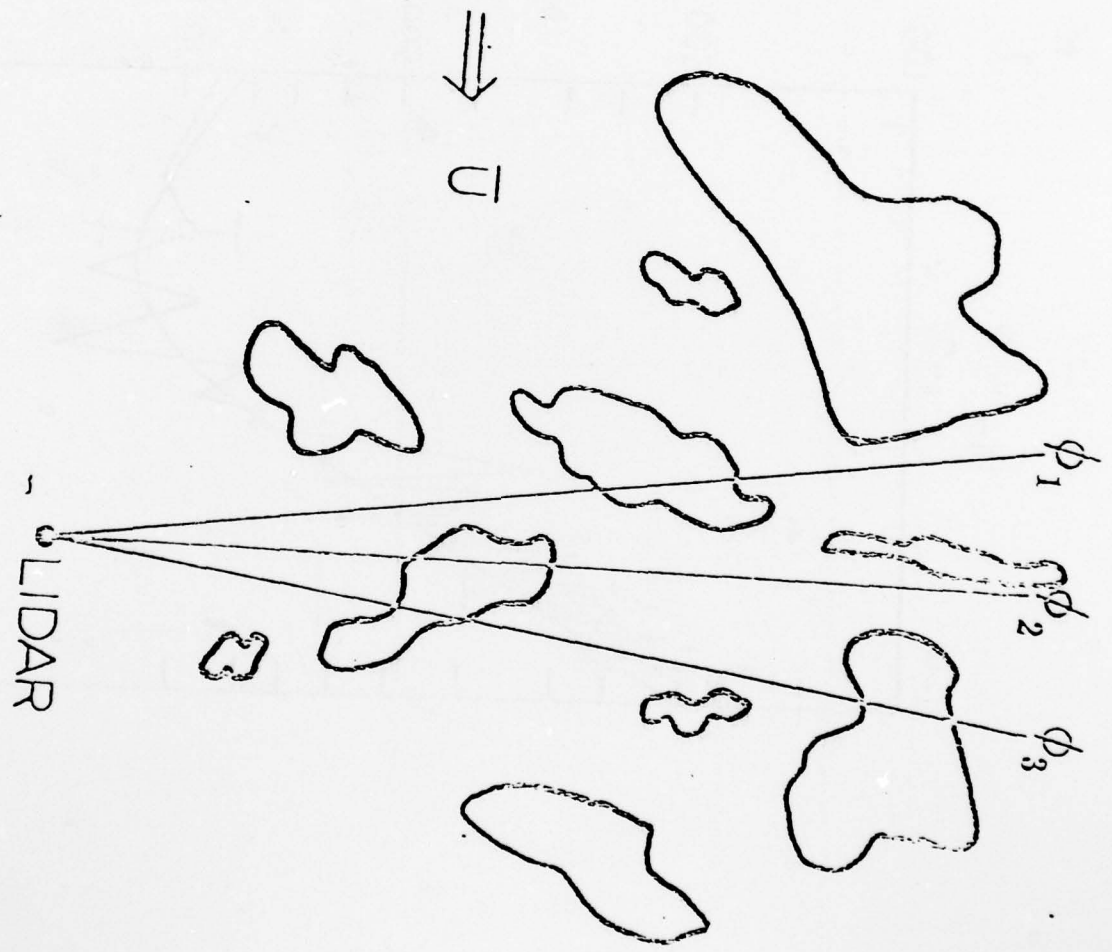


Fig. 2



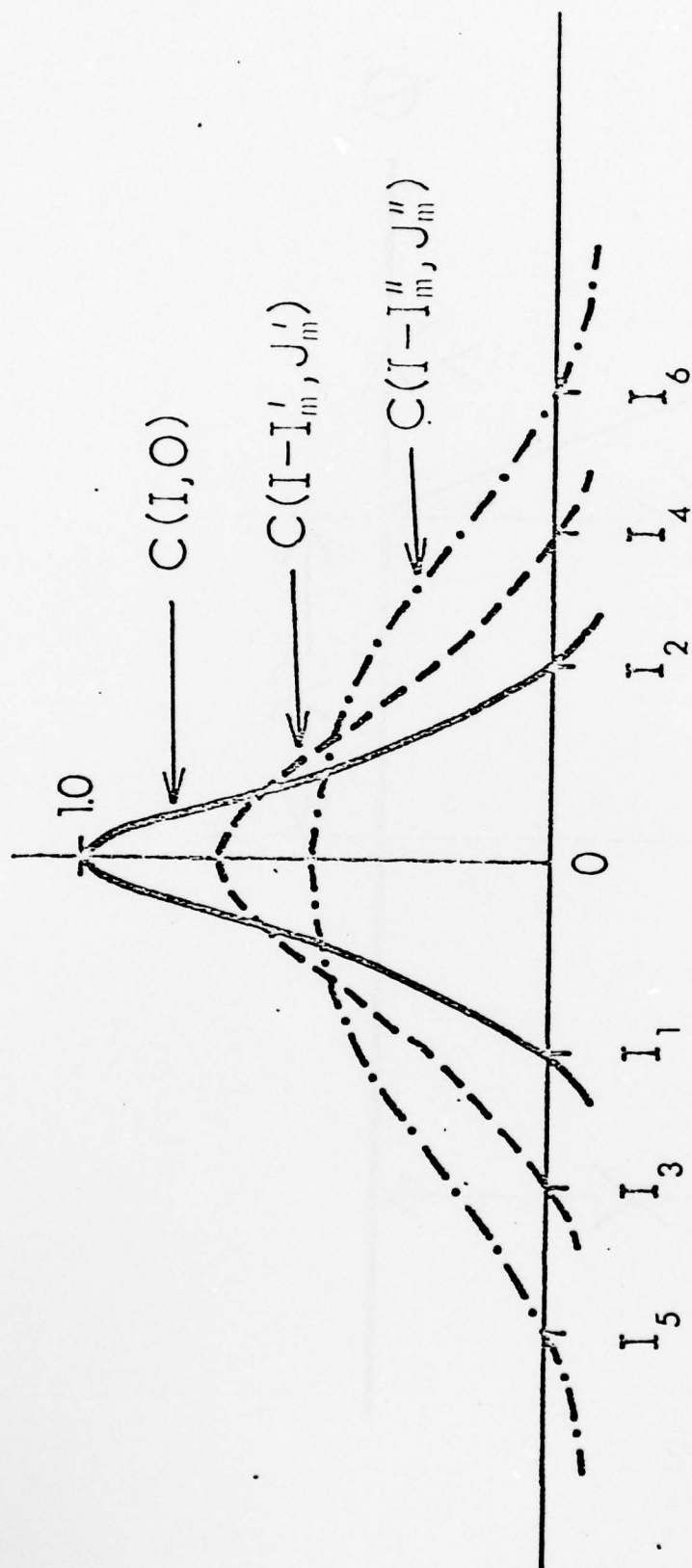


Fig 3

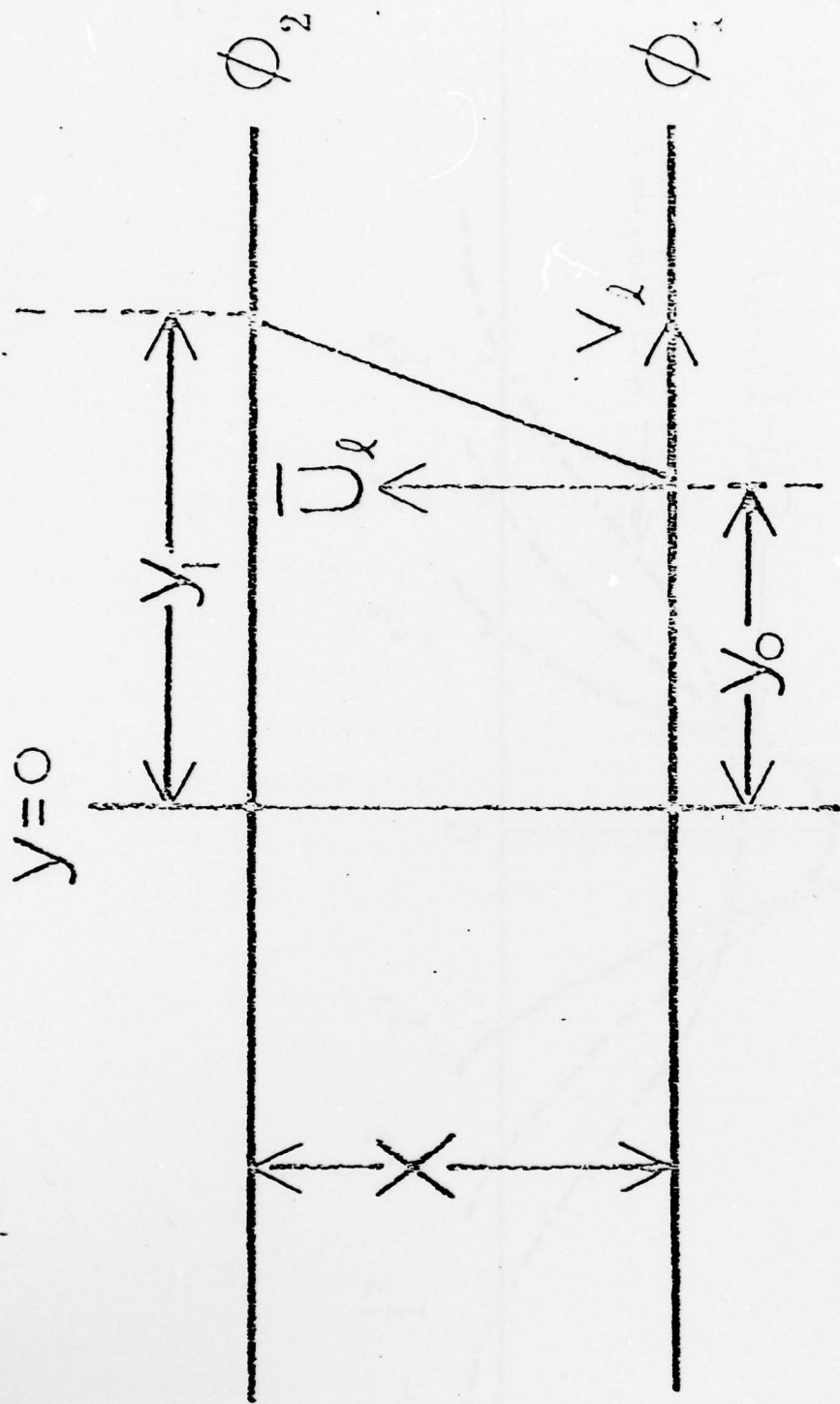


Fig. 4

APPENDIX D

THE USE OF LIDAR IN TESTING INVERSION RISE MODELS

REINOUT BOERS

MARCH 1979

A thesis submitted in partial fulfillment of the
requirements for the degree of
MASTER OF SCIENCE (Meteorology)
University of Utrecht, The Netherlands

Table of contents

Abstract	11
Acknowledgements.	2
List of symbols	3
Introduction	6
Instrumentation	8
Use of lidar in boundar layer observations .	11
Errors in estimating an inversion height .	15
Theory	17
A. Introduction	17
B. Equations	17
C. Parameterization.	19
Moisture correction to the heat flux . . .	23
Initialisation of the model	26
Site of the experiment.	28
Case studies	29
1. June 22, 1978.	29
2. June 23, 1978.	45
Discussion and conclusion.	62
Appendix	65
Profiles of case study 1	68
Profiles of case study 2	77
References	86

ABSTRACT

Lidar was used in determining the boundary layer height. During two days in June 1978, lidar data were obtained at Argonne National Laboratory, Illinois. During the observation periods, hourly temperature, wind and wind direction profiles were obtained by means of special radiosondes. In addition, heat flux, net solar radiation, Bowen ratio and friction velocity were measured by tower based instruments, located directly under the air volume, as observed by lidar.

It is shown, that lidar can overcome the lack of continuous data segments in testing boundary layer models. The Zeman-Tennekes model was compared with the observations. The results show, that the model underestimates the observed inversion rise.

ACKNOWLEDGEMENTS

I would like to thank the following persons:

Professor Dr. James Weinman, who made this experiment possible.

Dr. Edwin Floranta, for his constant help and encouragement, and for the many discussions I had with him concerning the lidar system and its use.

Dr. Richard Coulter and Dr. Marvin Wesely and their group at Argonne National Laboratory, Illinois, who assisted us during the experiment.

William Hooper, Jeffrey Sroga and Scott Shipley for their help in gathering the data and picture processing.

Drs. Ad Driedonks, at the Royal Meteorological Institute of the Netherlands for proofreading the thesis.

This research was conducted under A.R.O.D. grant, number DAA C29-76-C-0156.

LIST OF SYMBOLS

A	effective aperture of receiver
A_c	latent heat of condensation
β'	back scattering coefficient
B	Bowen ratio
c	speed of light
c_p	specific heat of air with constant pressure
C_D	dissipation term constant
C_F	flux divergence term constant
C_P	production term constant
C_T	temporal term constant
$\Delta u, \Delta v$	components of mean velocity jump across the inversion
$\Delta \rho$	density jump across the inversion
$\Delta \theta$	potential temperature jump across the inversion
d	dissipation length
ϵ_i	dissipation at the inversion base
E	vapor flux
E_0	laser energy output per pulse
η	constant, used to combine the mechanical part of the standard deviation of vertical velocity with the convective part
f	Coriolis parameter
g	acceleration due to gravity
γ	lapse rate in the atmosphere above the inversion
H	dry heat flux
H_1	latent heat flux

H_v	virtual heat flux
L	latent heat of condensation
M	mean molecular weight of air
M_d	molecular weight of dry air
M_w	molecular weight of water vapor
p	pressure
P_i	production, due to shear, at the inversion
$\frac{-2}{q}$	turbulent kinetic energy at the inversion base
q	specific humidity
R	universal gas constant
r	range
ρ_d, ρ_w	densities of dry air and water vapor
ρ	density of air
s_x, s_y	components of shear above the inversion
σ	extinction coefficient
σ_w	standard deviation of vertical velocity
ω_b	Brunt-Väisälä frequency
t	time
θ'	first order fluctuation of mean potential temperature
θ	potential temperature
θ_v	virtual potential temperature
θ_a	ambient potential temperature
T_o	temperature in the bulk of the boundary layer
T_v	virtual temperature
\bar{T}	temperature in the bulk of the boundary layer

U_g, V_g components of the geostrophic wind
 U, V components of the mean wind above the inversion
 u', v', w' first order fluctuations of the mean wind components
 u_* friction velocity
 w_* convective velocity scale
 z height
 z_i inversion height
 z_{i0} inversion height at the initial time

INTRODUCTION

A problem in air pollution is the occurrence of temperature inversions, that will trap waste gases in a layer near the earth's surface. In clear air conditions, the nocturnal boundary layer is usually thin. During the morning hours, the surface heat flux becomes positive and the boundary layer will heat up. Convective cells reach the inversion and mixing with the air aloft will cause the inversion to rise, thus increasing the depth of the boundary layer. This process is called entrainment.

In the last few years, various simple models have been developed to describe the inversion rise mechanism (Stull, 1973; Stull, 1976; Tennekes, 1973; Zeman, 1975; Zeman and Tennekes, 1977; Mahrt and Lenschow, 1976). These models are supported by few observations, since it has been difficult to obtain a continuous data set of the growing boundary layer (Willis and Deardorff, 1974; Kato and Phillips, 1969) .

Lidar, the optical equivalent of radar, has been used for a more detailed analysis of the inversion rise mechanism. In clear air conditions, the most important source for light reflections to the receiver is aerosol. This aerosol, created by man made pollution, or by natural sources at the surface, is continuously injected into the atmosphere, and is trapped in the layer near the ground. Thus, the boundary layer will contain a large amount of aerosol in comparison with the air aloft. As the layer grows during the morning hours, the aerosol is transported upward.

AD-A078 590

WISCONSIN UNIV-MADISON DEPT OF METEOROLOGY

F/G 4/2

LIDAR MEASUREMENT OF BOUNDARY LAYER WINDS AND CONVECTIVE STRUCT--ETC(U)

AUG 79 E W ELORANTA

DAA629-76-6-0156

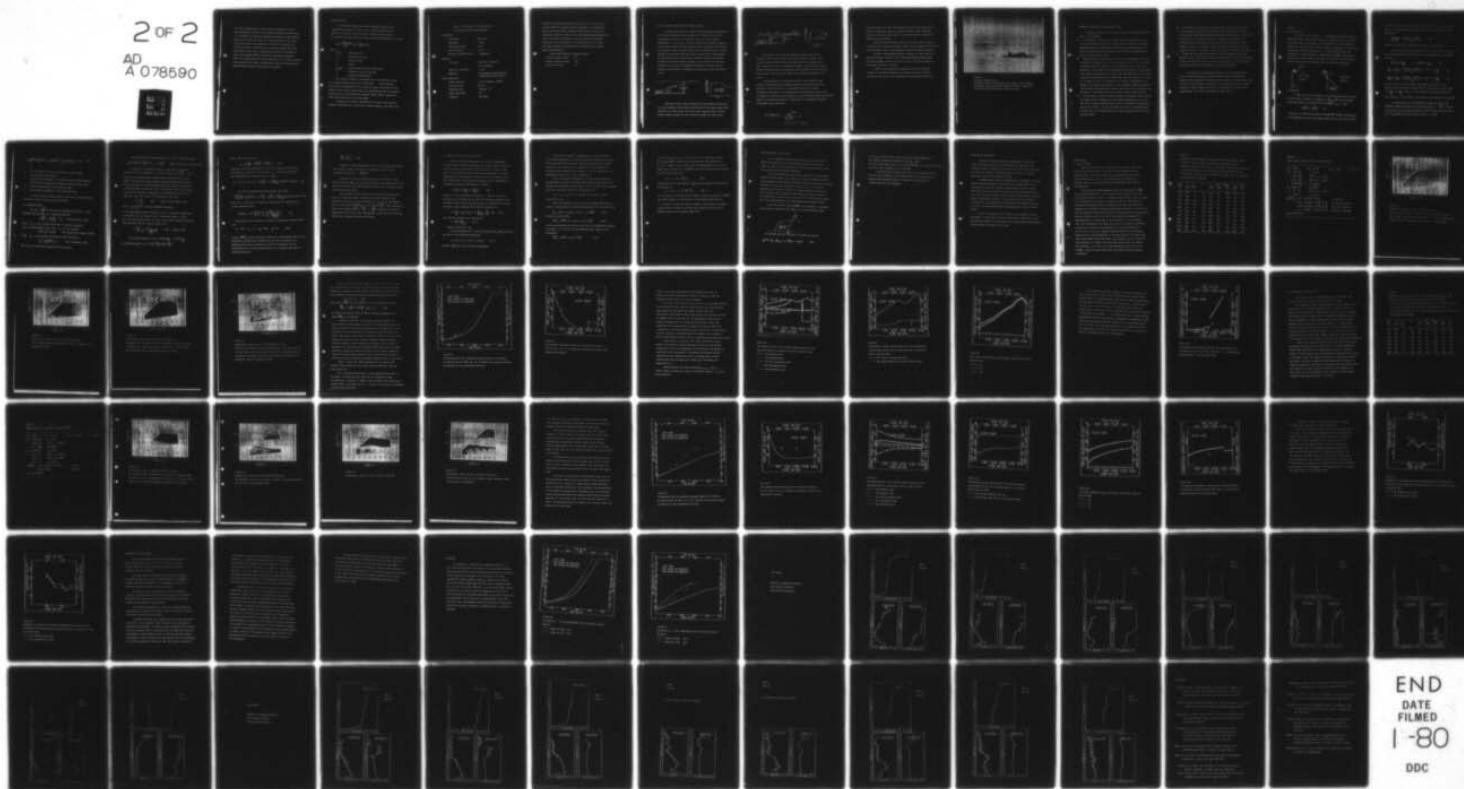
UNCLASSIFIED

ARO-13535.2-6S

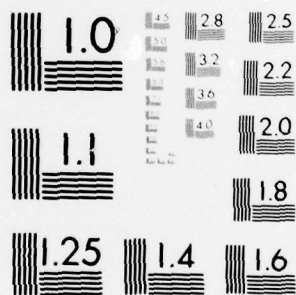
NL

2 OF 2

AD
A 078590



END
DATE
FILMED
1-80
DDC



MICROCOPY RESOLUTION TEST CHART
NATIONAL BUREAU OF STANDARDS-1963-A

With the scanning lidar system, which is capable of making two-dimensional pictures of the relative aerosol concentration, it is possible to determine remotely the height of the boundary layer as a function of time. It is also possible to get more information about the processes, involved in entrainment, by looking at spacial variations in mixed layer depth. The lidar observations were used in testing the inversion rise model by Zeman and Tennekes (1977). During the observation periods, heat flux, Bowen ratio, net solar radiation and friction velocity were measured, and hourly, temperature, wind and wind direction profiles were obtained from balloon soundings.

INSTRUMENTATION

A ruby laser (694.3 nm), that transmits pulses with a repetition frequency of about 1 Hz, is mounted parallel to a Newtonian telescope, that receives the backscattered light.

For singly scattered received power, the following equation is valid:

$$P(r) = \frac{E_0 A c \beta'_{180^\circ}}{8\pi r^2} \exp -2 \int_0^r \sigma(r') dr'$$

where :

$P(r)$	received power
E_0	transmitted energy
c	speed of light
r	range
β'_{180°	volume backscattering coefficient
A	effective receiver aperture
σ	extinction coefficient

The returned signal is converted into an electrical signal by a photomultiplier tube. After logarithmic amplification, the signal is digitized at 15 m range intervals, corrected for the inverse range squared attenuation and normalized by the transmitted energy E_0 . It is then stored on magnetic tape. Table 1 gives the lidar specifications of the 1978 model.

A single lidar return, displayed on a scope, shows varying aerosol intensities as a function of radial distance from the laser.

Table 1. Parameters of the University
of Wisconsin lidar system (1978).

Transmitter

Wavelength	694.3 nm
Beamwidth	1 mrad
Energy per pulse	1.5 J
Pulse duration	20 ns
Maximum repetition rate	1 pulse/sec

Receiver

Telescope	Newtonian reflector (.31 diameter)
Spectral resolution	1.0 nm
Detector	RCA C70042K Photomultiplier (6.8% quantum efficiency)

Data Acquisition

Video amplifier	Log (4 decades, 10 MHz)
A/D conversion	10 bits
Sampling rate	10^7 words s^{-1}
Range resolution	15 m
Computer	PDP 11/40

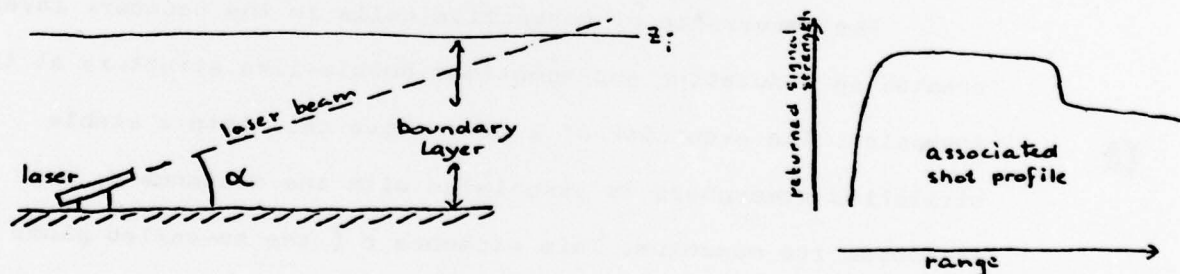
Usually, the boundary between the layer near the surface and the air aloft, is clearly visible, because of a significant drop of returned signal strength. After firing the laser at subsequent elevation angles (a so-called Range Height Indicator scan), the returned signals can be converted into relative intensities and displayed on a storage display. It is thus possible to obtain two-dimensional pictures of the relative aerosol distribution.

Typical RHI scanning parameters were:

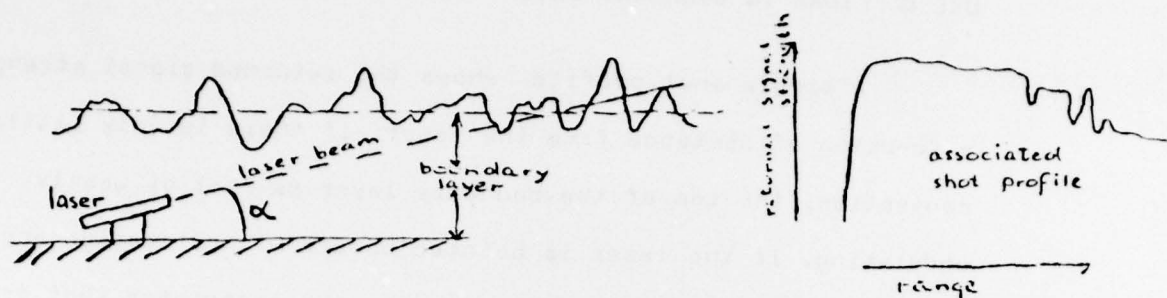
lowest elevation angle	3°
highest elevation angle	24°
scanning interval	$.5^{\circ}$

USE OF LIDAR IN BOUNDARY LAYER OBSERVATIONS

A single shot profile shows the returned signal strength as a function of distance from the laser. If there is only little convection, the top of the boundary layer is flat or weakly undulating. If the laser is pointed upward with elevation angle α , the inversion height can be located in the associated shot profile at the point, where a significant drop in returned signal strength appears. The distance from the laser, at which this drop appears, is multiplied by $\sin \alpha$ to get the inversion height. The initial increase in returned signal strength, as is visible in the shot profile, is due to the incomplete overlap of the laser and the receiver. The overlap is complete at distances of more than about .5 km.



Convective cells show themselves by more complex structures in a shot profile, which makes calculation of the exact height more difficult. A single laser pulse may pass through several plumes, giving several values for the inversion height for each pulse.



By scanning the laser up and down, RHI-pictures can be obtained. The inversion height was then estimated visually from a small storage display. Since the lidar data was obtained from a slant range of 7.5 km, the horizontal range, over which the average inversion height could be determined, was dependent on the inversion height itself. The averaging range varies typically between 1 and 5 km.

The occurrence of convective cells in the boundary layer creates an undulating and sometimes bubble-like structure at the inversion. The excursion of a convective cell into a stable stratified atmosphere is associated with the distance d , over which it loses its momentum. This distance d (the so-called plume penetration depth, or dissipation length) is known to be an important parameter in boundary layer modeling.

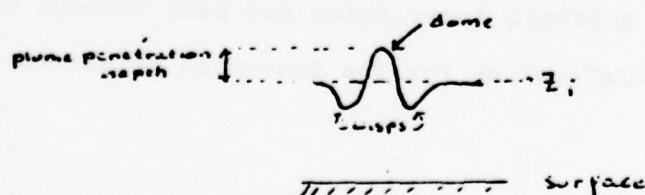


Figure a shows a typical RHI-picture. The convective cells at the top of the boundary layer are clearly visible. Thus, from this picture, it can be seen, that it is also possible to estimate the plume penetration depth.

Aerosol stratifications above the boundary layer allowed us to observe the creation of gravity waves there, because of interaction with convective cells, that penetrate into the stable atmosphere.

During an observation period, a series of 7 RHI scans were alternated with a series of PPI scans (Plan Position Indicator) at three azimuth angles. The time interval between two series of RHI scans was about 5 minutes.

Lidar is thus capable of overcoming one of the biggest problems in testing inversion rise models by giving an almost continuous data set of some important boundary layer quantities.

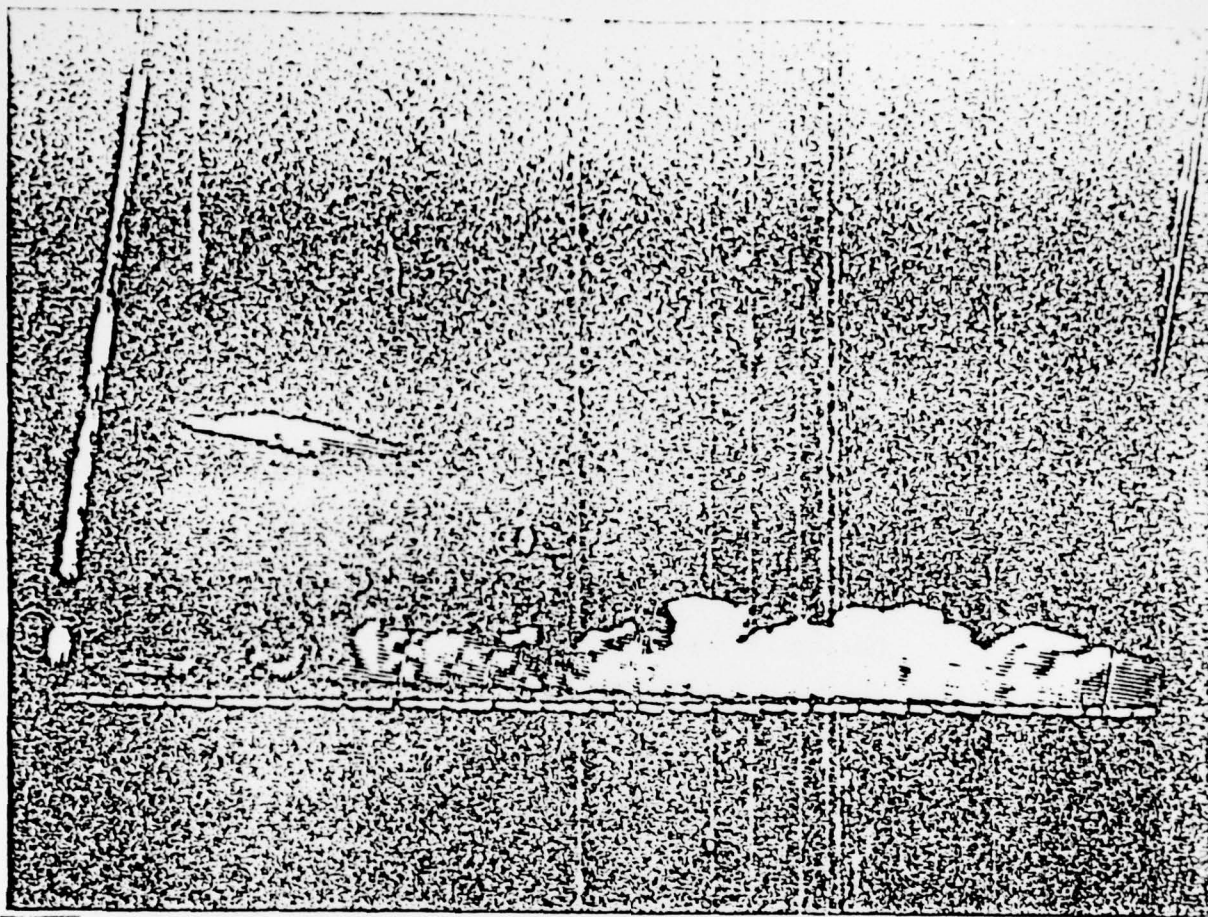


Figure a:

a typical RHI-picture.

The white areas in the picture are regions that contain relatively large amounts of aerosol. Clearly visible are the convective cells at the inversion base.

ERRORS IN ESTIMATING AN INVERSION HEIGHT

Sources of error in estimating visually the inversion height, have to be examined:

- A: The estimate is done from a small display screen, which makes the determination of the exact height rather difficult. Sometimes magnification of the RHI-picture could improve the estimate. The error introduced here is dependent on the factor of magnification and is of the order of 75 m.
- B: During portions of the day, the top of the boundary layer has an irregular structure. This is due to convection or to the occurrence of gravity waves. If the top of the boundary layer is flat, the estimate of the height can be supported by calculation of the height from single shot profiles. In that case, the other sources of error, that are mentioned here, are unimportant, and the overall error can be as small as 15 m. If convection is visible, calculation of the height from single shot profiles is not reliable. During periods of rapid growth, big plumes are visible, that have their sources at the surface. In that case, the overall error can be as big as 150 m.
- C: If the drop in aerosol content between the boundary layer and the air aloft was not limited to a very short distance, or if the air aloft had a large aerosol content too, the transition from black to white on a picture was very gradual. The error in estimating the height, that is introduced here, is rather variable, but can be as much as 100 m.

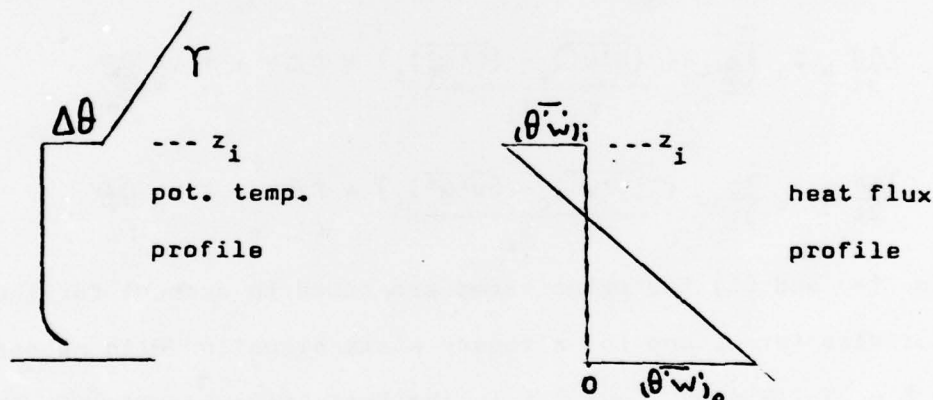
- D: Variations in the slope of a shot profile, caused by attenuation of the signal, influence the gray scale enhancement, that is used in converting the signals into RHI-pictures. The gray scale enhancement influence the transition from black to white in a picture, thus influencing the visibility of the structure of the boundary layer. Slope corrections to the gray scale enhancement sometimes had to be adjusted manually from shot to shot. The error introduced is variable.
- E: During the data taking sessions, a malfunctioning in the energy monitor of the lidar system produced some problems in the normalization of each shot profile with the transmitted energy E_0 . This introduced sometimes variable fluctuations from signal to signal.

In practice, the mentioned sources of error interact and it was not always possible to discern between them. In summary, the overall error depended on the state of evolution of the boundary layer. In early morning hours, the error can be as small as ± 15 m. During periods of rapid growth, the error is $\pm 100-150$ m. As soon as the growth stops, the error drops again to about 75 m.

THEORY

A. Introduction

The model to be tested is developed by Zeman and Tennekes (Tennekes, 1973; Zeman, 1975; Zeman and Tennekes, 1977). It applies to a horizontally homogeneous, dry atmosphere, in which radiation effects are neglected. The boundary layer is assumed to be well mixed, so that the potential temperature is constant with height. The inversion is characterised by a temperature jump $\Delta\theta$, above which the air has a lapse rate γ . The model is valid for zero or positive surface heat flux, thus applying only to day time conditions.



B. Equations

If the air at the inversion is entrained downward, it loses per unit time an amount of enthalpy of $\Delta\theta c_p \rho \frac{dz_i}{dt}$. This enthalpy is carried away by a downward heat flux $(\theta'w')_i c_p \rho$. So:

$$-(\theta'w')_i = \frac{dz_i}{dt} \Delta\theta \quad (1)$$

The rate, at which the inversion strength $\Delta\theta$ changes, is governed by the heating rate of the boundary layer and by the rate, at which

the boundary layer rises into the stable atmosphere with lapse rate γ . If we assume a linear decrease in heat flux with height, this results in:

$$\frac{\partial \Delta \theta}{\partial t} = \gamma \frac{\partial z_i}{\partial t} - \frac{(\overline{\theta'w'})_0 - (\overline{\theta'w'})_i}{z_i} \quad (2)$$

Changes of γ during the entrainment process are neglected.

If ΔU and ΔV are the jumps of mean velocity at the inversion base, similar equations are valid for the components of the Reynold stresses:

$$-(\overline{u'w'})_i = \Delta U \frac{\partial z_i}{\partial t}, \quad -(\overline{v'w'})_i = \Delta V \frac{\partial z_i}{\partial t} \quad (3)$$

$$\frac{\partial \Delta U}{\partial t} = S_x \frac{\partial z_i}{\partial t} - \frac{(\overline{u'w'})_0 - (\overline{u'w'})_i}{z_i} + f \Delta V + f v_g \frac{\Delta \rho}{\rho_0} \quad (4)$$

$$\frac{\partial \Delta V}{\partial t} = S_y \frac{\partial z_i}{\partial t} - \frac{(\overline{v'w'})_0 - (\overline{v'w'})_i}{z_i} - f \Delta U + f u_g \frac{\Delta \rho}{\rho_0} \quad (5)$$

In (4) and (5) the extra terms are added to account for the Coriolis force, and for a steady state situation with no heat flux.

($S_x = \frac{\partial U}{\partial z}$, $S_y = \frac{\partial V}{\partial z}$, $z > z_i$, f is the Coriolis parameter, ρ_0 is the mean density of the air, $\Delta \rho$ is the density jump across the inversion)

To complete the set of equations, one has to look at the turbulent energy equation at the inversion base. If $\frac{1}{2} \overline{q^2}$ is the sum of horizontal and vertical turbulent kinetic energy per unit mass, and if we assume no mean vertical motion, it reads:

$$\frac{1}{2} \frac{\partial \overline{q^2}}{\partial t} = \underbrace{\frac{g}{T_0} \overline{(\theta' w')}}_a - \underbrace{\frac{\partial}{\partial z} \left(\overline{\frac{1}{2} q^2 w'} \right)}_b + \underbrace{\frac{1}{\rho} \overline{(p' w')}}_c - \underbrace{\epsilon_i}_d + \underbrace{P_i}_e \quad (6)$$

- a is the temporal change of turbulent kinetic energy
 b is the buoyancy production
 c is the flux divergence of turbulent kinetic energy combined with the flux divergence of pressure-velocity correlation
 d is the dissipation at the inversion base
 e is the shear production at the inversion base

To solve system (1)-(6), equation (6) has to be parameterized in terms of known boundary layer quantities.

C. Parameterization

The term $\frac{1}{2} \frac{\partial \overline{q^2}}{\partial t}$ is known to be important in periods of rapid boundary layer growth. It is parameterized as:

$$\frac{1}{2} \frac{\partial \overline{q^2}}{\partial t} = C_T \frac{\sigma_w^2}{h} \frac{\partial z_i}{\partial t} \quad (7) \quad (\text{Zilitinkevich, 1975})$$

where σ_w is the standard deviation of vertical velocity.

σ_w is proportional to w_* and u_* via the relation

$$\sigma_w^2 = w_*^2 + \eta^2 u_*^2 \quad (8) \quad (\text{Zeman and Tennekes, 1977})$$

where w_* is the convective velocity scale defined as

$$w_*^3 = \frac{g}{T_0} \overline{(\theta' w')} z_i \quad (9) \quad (\text{Tennekes, 1970})$$

and u_* is the friction velocity at the surface.

The flux divergence term scales on σ_w and z_i via the formula:

$$-\frac{\partial}{\partial z} \left(\frac{1}{2} \overline{q^2 w'} + \frac{1}{\rho} \overline{p' w'} \right) = C_f \frac{\sigma_w^3}{z_i} \quad (10) \quad (\text{Zeman and Tennekes, 1977})$$

If there is a turbulent energy cascade process near the inversion, the dissipation ϵ_i can be written as $C_D \frac{\sigma_w^3}{d}$ (11)

where d is a characteristic length scale of dissipation. In many cases, d is different from z_i and all the dissipation, that scales on z_i , is put into the flux divergence term. The parameterization of d can be derived in different ways. The simplest one is by stating, that the only important parameters, in determining its value, are

σ_w and γ . This leads to an estimate of the type

$$d = \frac{\sigma_w}{\omega_b} \quad (12) \quad (\text{Stull, 1973; Zeman, 1975})$$

where $\omega_b = \left(\frac{g}{T_0} \gamma \right)^{1/2}$ the Brunt-Väisälä frequency.

If the atmosphere, above a boundary layer, is neutrally stratified, a situation, that can happen, when a well mixed layer is left over from the previous day, γ goes to zero, and d becomes infinite. More realistic then is, that d scales on z_i :

$$d = \frac{\sigma_w}{\omega_b} \frac{1}{\left(1 + \left(\frac{\sigma_w}{z_i \omega_b} \right)^2 \right)^{1/2}} \quad (13) \quad (\text{Zeman, 1975})$$

The energy production term $-(\overline{u'w'}) \frac{\partial u}{\partial z} - (\overline{v'w'}) \frac{\partial v}{\partial z}$ is parameterized as $C_p \left(-(\overline{u'w'}) \frac{\Delta u}{d} - (\overline{v'w'}) \frac{\Delta v}{d} \right)$

Using (3), this leads to :

$$P_i = C_p \frac{\partial z_i}{\partial t} \left(\frac{(\Delta U)^2}{d} + \frac{(\Delta V)^2}{d} \right) \quad (14)$$

Assuming, that the production term can not exceed the dissipation very much, C_p must be of the order of C_D . Usually, production and dissipation are combined in one formula:

$$\epsilon_i - P_i = \epsilon_i (1 - \chi) = C_D \frac{\sigma_w^3}{d} \left(1 - \frac{\partial z_i}{\partial t} \frac{1}{C_w^3} ((\Delta U)^2 + (\Delta V)^2) \right) \quad (15)$$

The fully parameterized energy budget now reads:

$$C_T \frac{\sigma_w^2}{z_i} \frac{\partial z_i}{\partial t} = \frac{g}{T_0} (\overline{\theta' w'})_i + C_F \frac{\sigma_w^3}{z_i} - C_D \frac{\sigma_w^3}{d} \left(1 - \frac{\partial z_i}{\partial t} \frac{1}{C_w^3} ((\Delta U)^2 + (\Delta V)^2) \right) \quad (16)$$

Using (1), one can get an explicit expression for the heat flux at the inversion base:

$$(\overline{\theta' w'})_i = (-1) \frac{\sigma_w^3}{z_i} \frac{T_0}{g} \frac{C_F - C_D \frac{z_i}{d} (1 - \chi)}{1 + C_T \frac{\sigma_w^2 T_0}{z_i \Delta \theta_g}} \quad (17)$$

The values of the constants, as given by Zeman and Tennekes (1977) are:

$$C_T = 3.55, \quad C_F = .5, \quad C_D = .024, \quad \eta = 2.0 \quad (18)$$

If $\gamma \rightarrow 0$, $(\overline{\theta' w'})_i \rightarrow 0$ and $d \rightarrow z_i$, and since C_D is much smaller than C_F , the dissipation becomes much smaller than the flux divergence. The temporal term is then balanced by the flux divergence, and the entrainment rate is only proportional to the standard deviation of vertical velocity:

$$\frac{\partial z_i}{\partial t} = \frac{c_F}{c_T} \sigma_w \quad (19)$$

Another situation, that might occur, is, when the dissipation term becomes bigger than the flux divergence. In that case entrainment stops, and $(\overline{\theta'w'})_i = 0$

System (1) - (5), and (16) is now fully solvable, if the initial values of Δt , z_i , γ , S_x , S_y and ΔU , ΔV are known, and if the course of the heat flux and friction velocity are prescribed during the observation periods.

The solution of this system can be obtained numerically by using an iteration scheme. Knowing the initial values of the mentioned parameters, we can evaluate w_* , σ_w , z_i/d , and $(\overline{\theta'w'})_i$. With the new value of $(\overline{\theta'w'})_i$, we can compute $\frac{\partial z_i}{\partial t}$, and knowing this one, we can evaluate $\frac{\partial \Delta \theta}{\partial t}$ and $\frac{\partial \Delta U}{\partial t}$, $\frac{\partial \Delta V}{\partial t}$. Finally, by using the appropriate time step, we can compute Δt , z_i , ΔU and ΔV at the new time. Then we repeat the whole procedure.

MOISTURE CORRECTION TO THE HEAT FLUX

One of the model assumptions is, that the atmosphere is dry. Except from arid regions, like deserts, this is not the case. Moist air is less dense than dry air by a small amount, due to the presence of water vapor, and therefore, it has more buoyancy than a corresponding parcel of dry air, that has the same temperature. The moisture correction to the temperature is derived, starting at the equation of state:

$$p = \frac{R}{M} \rho T = \frac{R}{M_d} \rho_d T + \frac{R}{M_w} \rho_w T \quad (20)$$

where M is the mean molecular weight of wet air, R is the universal gas constant, M_d , M_w are the molecular weights of dry air and of water vapor, and ρ_d , ρ_w are the densities of dry air and water vapor. Equation (20) can be rewritten as:

$$p = \frac{R}{M_d} T (\rho_d + \rho_w) \left(1 + \frac{\rho_w}{\rho_d + \rho_w} \left(\frac{M_d}{M_w} - 1 \right) \right) \quad (21)$$

The specific humidity q is defined as:

$$q = \frac{\rho_w}{\rho} = \frac{\rho_w}{\rho_d + \rho_w} \quad (22)$$

and $M_d = 28.9$, $M_w = 18$.

If we substitute (22), and the values of M_d and M_w in (21), we come to the following expression:

$$p = R \rho T (1 + .61 q) = R \rho T_v \quad (23)$$

where $R = \frac{R}{M}$ and T_v the virtual temperature.

In words, the virtual temperature of a parcel of moist air is the temperature, at which a fictitious neighbouring parcel of dry air would have the same density, and therefore the same buoyancy as the moist air. In using the virtual temperature, we can apply the model, that is based on the assumption of a dry atmosphere, directly on a moist atmosphere.

Like the virtual temperature (or the virtual potential temperature), we have to introduce the virtual heat flux. If we define some reference state by $T_{vo} = T_o (1 + .61 \bar{q})$, any deviation from this reference state will be described by :

$$T'_v = T_v - T_{vo} = T' (1 + .61 \bar{q}) + T q' .61 \quad (24)$$

where $T' = T - T_o$.

Time fluctuations of T'_v , as can be directly expressed in terms of fluctuations of potential temperature θ' , are written as:

$$\theta'_v = \theta' (1 + .61 \bar{q}) + .61 q' T - .61 \overline{q' \theta'} \quad (25)$$

and thus, we may write:

$$\overline{w' \theta'_v} = \overline{w' \theta'} (1 + .61 \bar{q}) + .61 \bar{T} \overline{q' w'} \quad (26)$$

In the last equation the third order terms are neglected. Usually, the factor $(1 + .61 \bar{q})$ is ignored, too, which leads to the expression:

$$\overline{w' \theta'_v} = \overline{w' \theta'} + .61 \bar{T} \overline{q' w'} \quad (27)$$

If H is the heat flux, as measured by the instruments, defined as $H = \rho c_p (\overline{w' \theta'})$, and H_1 is the latent heat flux, defined as $H_1 = LE$, where L is the latent heat of condensation and E is the vapor flux, written as $E = \rho (\overline{w' q'})$, we come to the final expression of the virtual heat flux :

$$H_v = H + .61 \bar{T} \frac{c_p}{L} H_1 \quad (28)$$

The Bowen ratio is defined as $B = \frac{H}{LE}$, so the virtual heat flux may be written as :

$$H_v = H \left(1 + .61 \bar{T} \frac{c_p}{L} \frac{1}{B} \right) \quad (29)$$

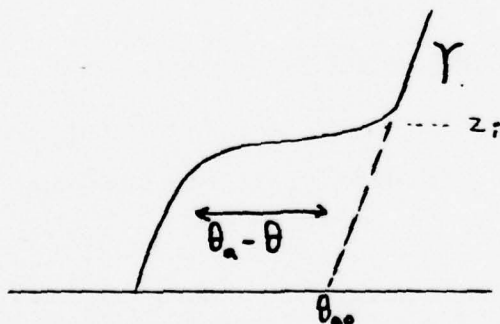
If we assume an air temperature of 300 K, and take $c_p = .24 \text{ cal / gm / } ^\circ\text{K}$, and $L = 585 \text{ cal / gm}$, the correction to the observed heat flux is $(1 + .075 / B)$. Over the ocean or above a wet surface, the Bowen ratio can be of order .1, so that the virtual heat flux can be twice as much as the observed heat flux.

INITIALISATION OF THE MODEL

It is important to know accurately the initial value of θ and the lapse rate in the atmosphere above the inversion, since the model is very sensitive to those input parameters. Both were determined from balloon soundings.

To get the lapse rate above the inversion, the temperature profiles at the initial time and all previously obtained profiles were averaged. In the stable atmosphere above the inversion, vertical transport of heat by turbulence is small, and if we assume no advection, the thermal structure of those profiles should be the same. However, later during the observation periods, changes in the upper part of the profiles did occur. This had to be accounted for in the computation of the mean profiles (see CASE STUDIES).

To get the initial value of $\Delta\theta$, the procedure, recommended in the earlier version of the model, was used (Tennekes, 1973)



An enthalpy deficit integral is defined as follows:

$$\int_0^{z > z_{ic}} (\theta_s - \theta)_{t=0} dz = \Delta\theta_0 z_{ic} - \frac{1}{2} \gamma z_{ic}^2 \quad (30)$$

where z_{io} is the initial value of the inversion height, t_a is the ambient temperature defined as $t_a = t_{ao} + \gamma z$. With the known lapse rate, we can evaluate Δt_o . If z_{io} is obtained from the lidar data, Δt_o can be computed.

The half-hourly averaged heat flux, the friction velocity, the net solar radiation and the Bowen ratio were measured at the Argonne meteorological tower. To account for moisture, the virtual heat flux was computed.

SITE OF THE EXPERIMENT

During June and July 1978, the University of Wisconsin lidar system was located at Argonne National Laboratory near Chicago, Illinois. Distance from Lake Michigan was about 20 miles. The lidar was pointed in south-easterly direction, a smoothly undulating region with patches of wood.

A meteorological tower, operated by the atmospheric sciences group at Argonne National Laboratory, was located about 1 mile south-east of the lidar system, directly under the air volume, that was observed. By tower based instruments, heat flux, latent heat flux, friction velocity and net solar radiation were measured. Hourly, temperature profiles and wind profiles of the lowest 2 kilometers of the atmosphere were obtained from balloon soundings (via the so-called Wind, Height And Temperature system, Frenzen, 1972) .

The days on which data was taken, were selected as being favorable, if clear air conditions would exist during the day and the previous night. If sea breezes from Lake Michigan were apparent from the data, the data was not used.

CASE STUDIES

1. JUNE 22 1978

Table 2 gives the solar radiation, Bowen ratio, heat flux, and friction velocity as a function of time. Computed are the moisture flux, the virtual heat flux, the moisture correction on the dry heat flux, and the fractional moisture correction. It appears, that the virtual heat flux is about 40% higher than the dry heat flux.

Since heat flux measurements started at about 630 CST, $\Delta\theta_0$ had to be estimated from run 3. Since the lower part of run 3 was not recorded properly, this is a rather crude estimate. When we looked at the temperature profiles, it appeared, that the upper part of the profiles changed during the course of the day. The lapse rate between 400 m and 600 m changed significantly between run 3 and run 4. This was probably caused by advection. A stratification at about 700 m, that is visible in run 2, 3, and 4, was gradually removed. It is characterised by a large jump in wind direction. It is possible, that the weakening of the lapse rate there is caused by turbulence. A crude way to account for advection is to use the profiles of run 2, run 4, and run 5, together with the profile at the initial time, run 3, in the computation of the mean profile. To compute the lapse rate between 150 m and 400 m, the profiles of run 2 and run 3 were averaged. To compute the lapse rate between 400 m and 600 m, the profiles of run 3 and run 4 were averaged. From run 5, it is visible, that the layer above 600 m has become almost neutrally stratified.

Table 2:

Additional meteorological data for case study 1 (June 22 1978).

Listed are time, net solar radiation S , the heat flux H , the Bowen ratio B , the latent heat flux H_1 , the moisture correction to the heat flux Δh , the fractional correction $\Delta h / H$, the virtual heat flux H_v , and the friction velocity u_* . All parameters are half-hourly averaged.

Time CST	S W/m^2	H W/m^2	B	H_1 W/m^2	Δh W/m^2	$\Delta h/H$ 100	H_v W/m^2	u_* m/s
645	180	7	.04	175	13	185	20	.20
715	242	24	.12	200	15	62	39	.23
745	306	41	.17	241	18	44	59	.24
815	372	48	.16	300	22	46	70	.24
845	424	73	.23	317	23	32	96	.24
915	474	80	.22	364	27	34	107	.23
945	482	57	.15	380	28	49	95	.19
1015	480	61	.16	381	28	46	89	.18
1045	584	81	.18	450	33	41	114	.15
1115	602	112	.25	448	33	29	145	.18
1145	624	70	.14	500	37	53	107	.19

Table 3:

Model input for case study 1 (June 22 1978)

$z_{i0} = 150 \text{ m}$	$\Delta t_o = 1.6^\circ\text{C}$	$\Delta U = 4 \text{ m/s}$	$u_* = .21 \text{ m/s}$
$\gamma = .003^\circ\text{C/m}$	$z_i < 400 \text{ m}$		
$= .001^\circ\text{C/m}$	$400 \text{ m} < z_i < 600 \text{ m}$		
$= .0^\circ\text{C/m}$	$600 \text{ m} < z_i < 1600 \text{ m}$		
$= .016^\circ\text{C/m}$	$z_i > 1600 \text{ m}$		
$S_x = -.015 \text{ s}^{-1}$	$z_i < 600 \text{ m}$		
$= .0 \text{ s}^{-1}$	$600 \text{ m} < z_i < 1400 \text{ m}$		
$= .022 \text{ s}^{-1}$	$z_i > 1400 \text{ m}$		
$(\overline{\theta_v'w'})_o = .02 + .07/150 t^\circ\text{C m/s}$	$t < 150 \text{ min}$		
$= .09 - .015/60 (t-150)^\circ\text{C m/s}$	$150 \text{ min} < t < 210 \text{ min}$		
$= .075 + .045/60 (t-210)^\circ\text{C m/s}$	$210 \text{ min} < t < 270 \text{ min}$		
$= .12 - .03/30 (t-270)^\circ\text{C m/s}$	$270 \text{ min} < t < 300 \text{ min}$		

t_o is at 630 CST

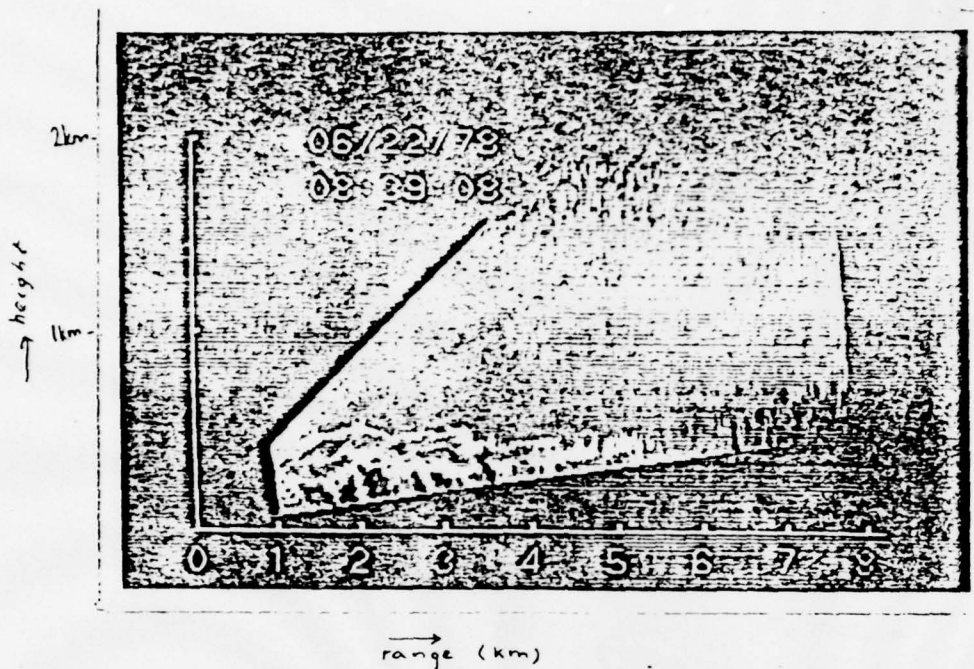


Figure 1:

RHI-picture, taken on June 22 1978 at 8.39 EDT .

The white areas contain relatively large amounts of aerosol.

The boundary layer, as visible here has a height of about 220 m.

There is some interaction with the layer directly above it .

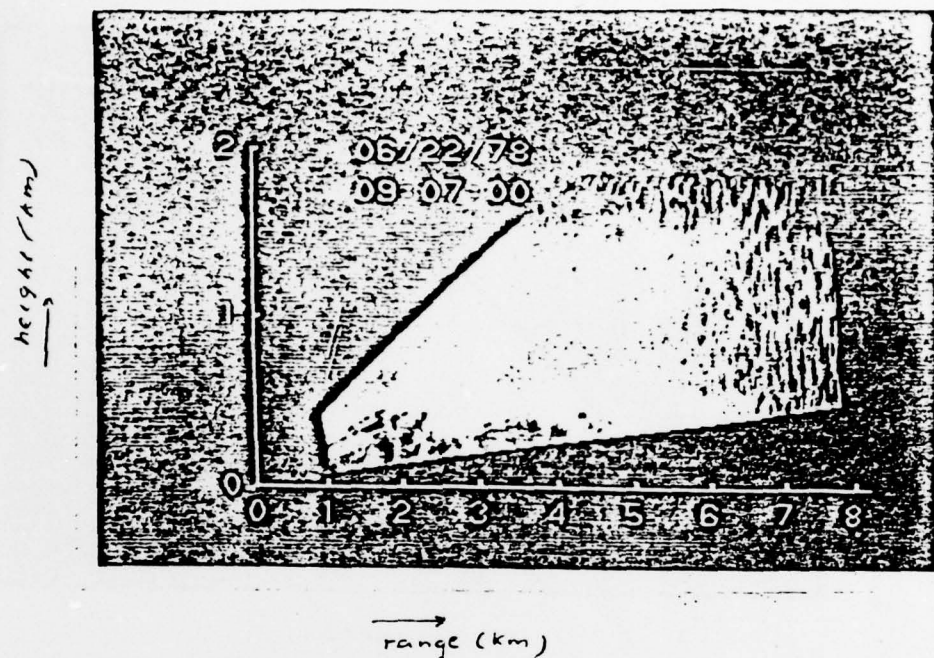


Figure 2:

RHI-picture, taken on June 22 1978 at 9.07 LDT.

The boundary layer has increased in depth, compared to the previous picture.

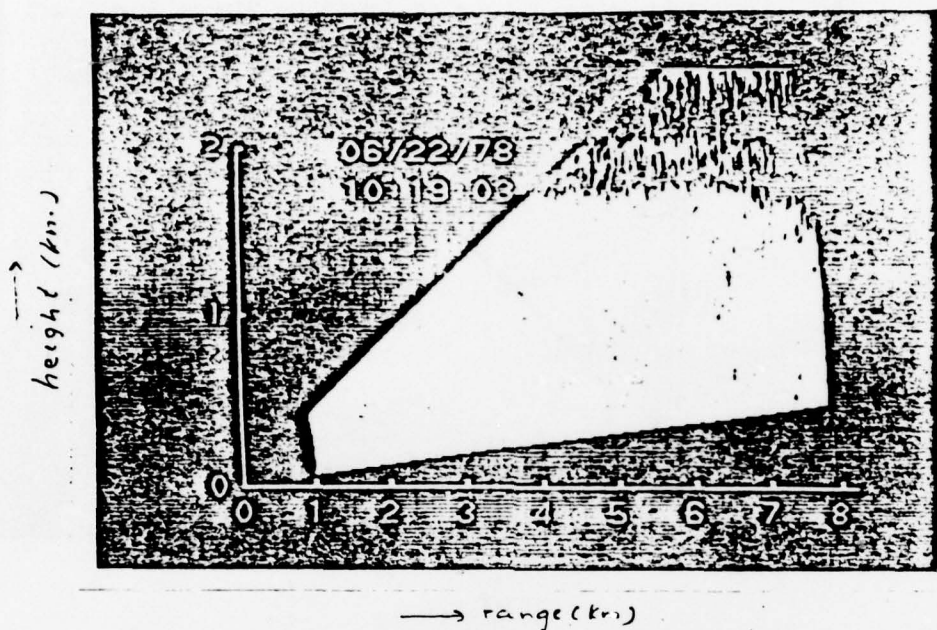


Figure 3:

RHI-picture, taken on June 22 1978 at 10.19 CLT .

Two plumes are visible, the left one almost reaching the upper inversion, the right one somewhat lower. During this portion of the period, the mixing process was very rapid.

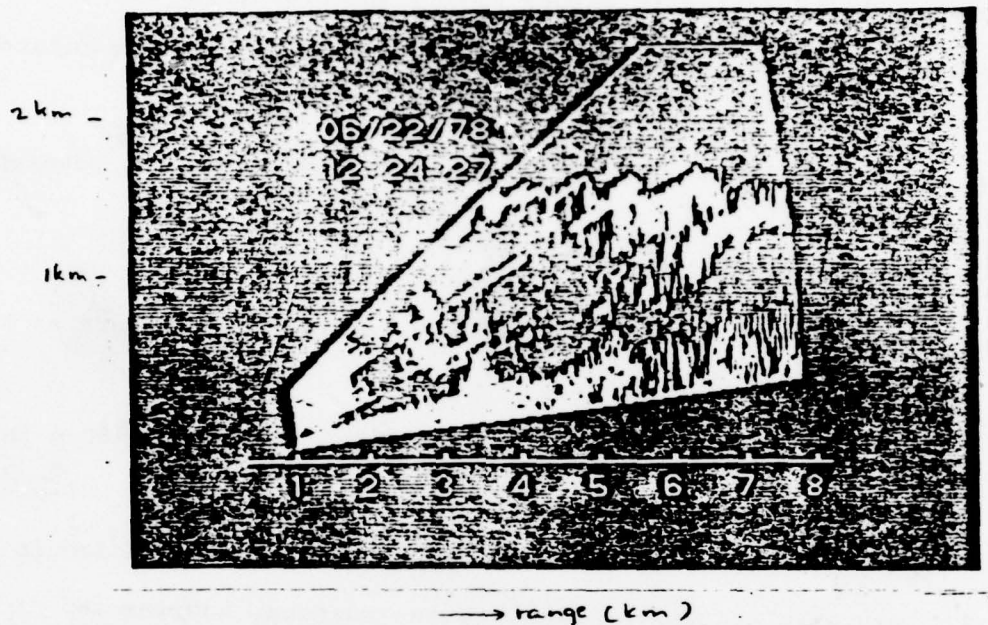


Figure 4:

RHI-picture, taken on June 22 1978 at 12:24 CDT .

The layer beneath 1600 m is entirely mixed. Note, that the top of this layer, that was flat in all the other pictures, has an irregular structure, indicating, that convective cells try to penetrate into the atmosphere aloft.

During the early morning hours, a low level jet existed with its maximum at the inversion. The rate of change of wind direction across the inversion is rather small, therefore, to account for the shear production, equation (4) was rewritten with the conditions:

$$v = 0, S_y = 0 \quad (21)$$

(21) leads to $\frac{\partial \Delta v}{\partial t} = 0$, and $-(\overline{v'w'})_i = 0$. Using (3), (4) becomes:

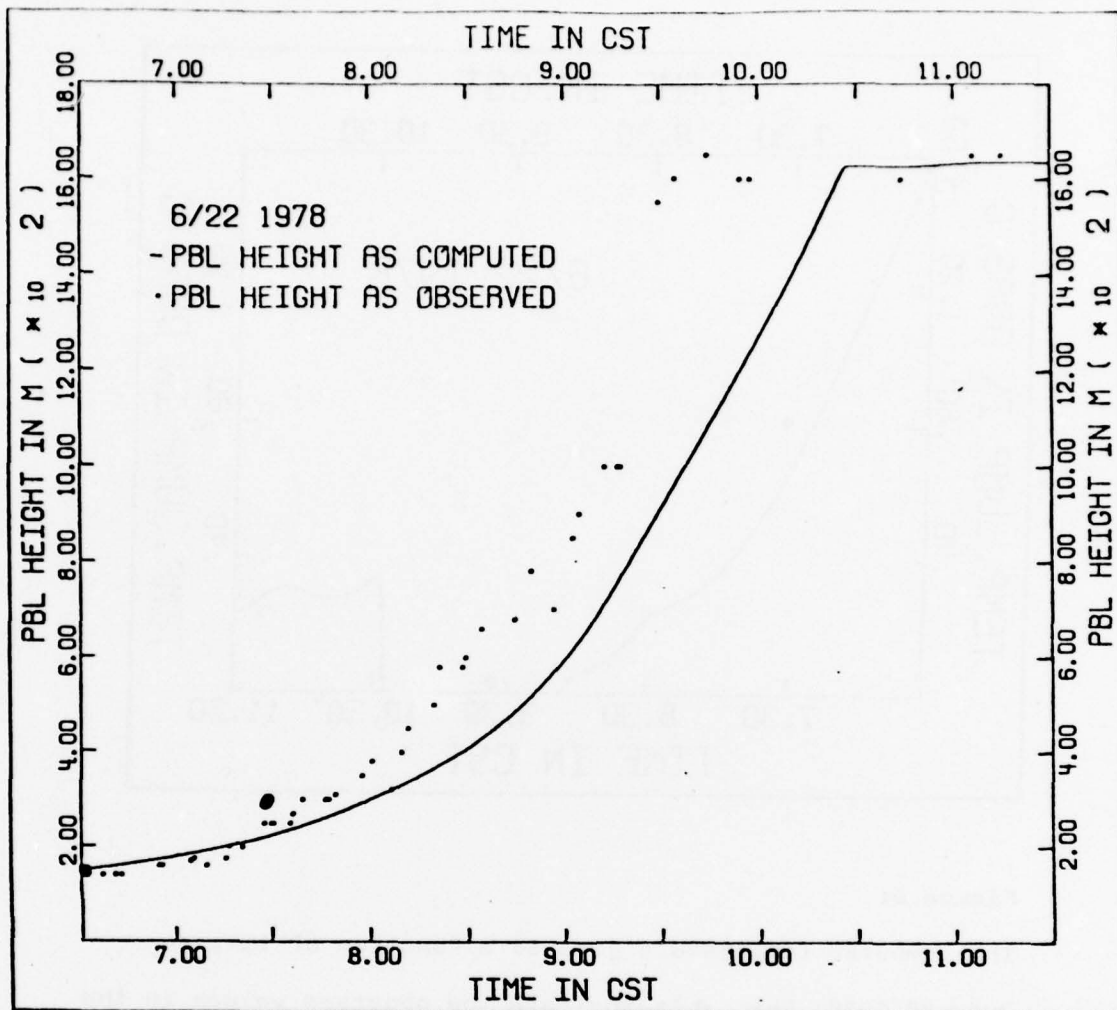
$$\frac{\partial \Delta u}{\partial t} = S_x \frac{\partial z_i}{\partial t} + (\Delta u \frac{\partial h}{\partial t} - u_*^2) / z_i \quad (22)$$

To compute the initial value of Δu , a similar procedure as to compute $\Delta \theta_0$ is recommended.

Starting at 630 CST, the inversion rises from 150 m to about 1600 m, 3 hours later. Figures 1 - 4 show some RHI-pictures from that period. In the early morning hours, convection is still confined to the region close to the surface, and the top of the layer, that reaches the strong inversion at 1600 m, is still flat. During the period of rapid growth, irregular shaped plumes are visible, that have their source at the surface. This is well in agreement with observations by Kunkel (1978). When the big plumes eventually reach the strong inversion, and the layer beneath it becomes entirely mixed, the top of this layer gets an irregular structure, because convective elements penetrate into the inversion.

Table 3 gives the input parameters of the model. The initial time was 630 CST, the final time was 1130 CST. The time step was 60 sec.

As is apparent from figure 5, the computed entrainment is too small. It takes too much time for the temperature jump to erode away (figure 6). About 1 hour too late, the mixed layer reaches 1600 m. The model can not account for the rapid entrainment, observed around 930 CST.



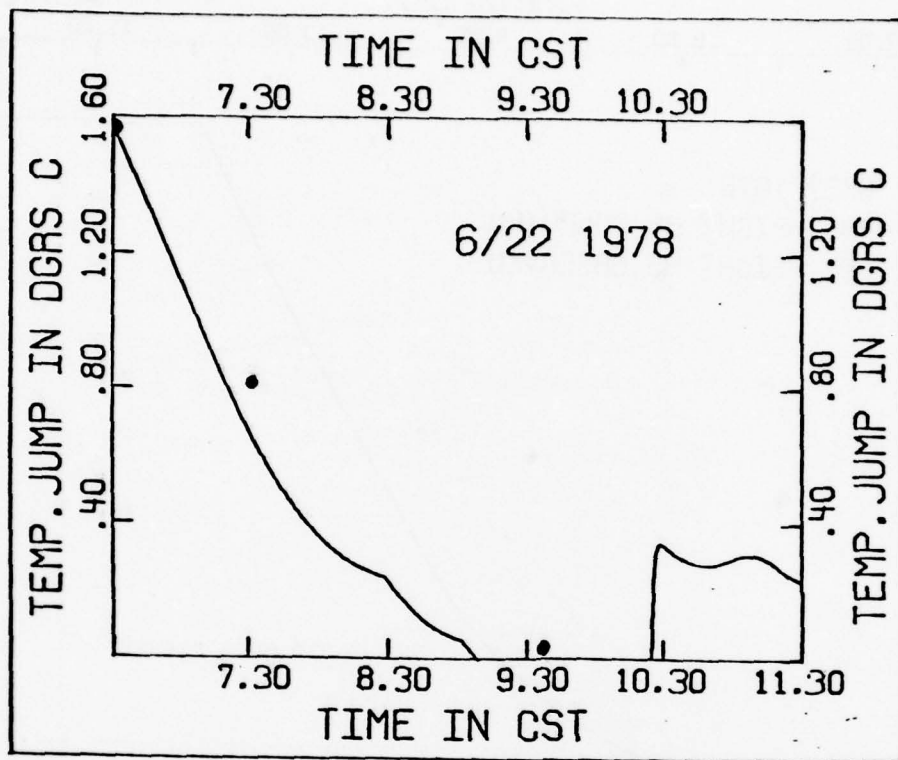


Figure 6:

The computed temperature jump as a function of time on June 22 1978. The •'s indicate the observed values in the temperature profiles.

Figure 6 also gives some values of the temperature jump, as observed from the temperature profiles. It appears, that the computed values follow the observed values.

In figure 7 are shown the terms of the energy budget equation as a function of time. When the lapse rate is zero, the temporal term equals the divergence of kinetic energy flux. The discontinuous character of this graph and all the others is caused by changes in the model input at the appropriate times and at specific heights, that are reached by the boundary layer. The production term remains small throughout the period, apart from a spike due to the model conditions $\gamma > 0$ and $\Delta \theta = 0$, at the moment, when the strongly stratified region is reached. The divergence term is then exactly balanced by the dissipation and entrainment stops.

From figure 8, it can be seen, that, during the initial period, the downward virtual heatflux is as big as the virtual surface heat flux. This indicates, that mechanical entrainment is important. As the day goes on, convective entrainment becomes gradually of more importance, since u_x remains small and the surface heat flux increases with time, thus influencing the magnitude of w_x .

Figure 9 gives the scaled velocities ζ_w , w_x and u_x . Again, clearly visible is, that the convective part of ζ_w is the most important.

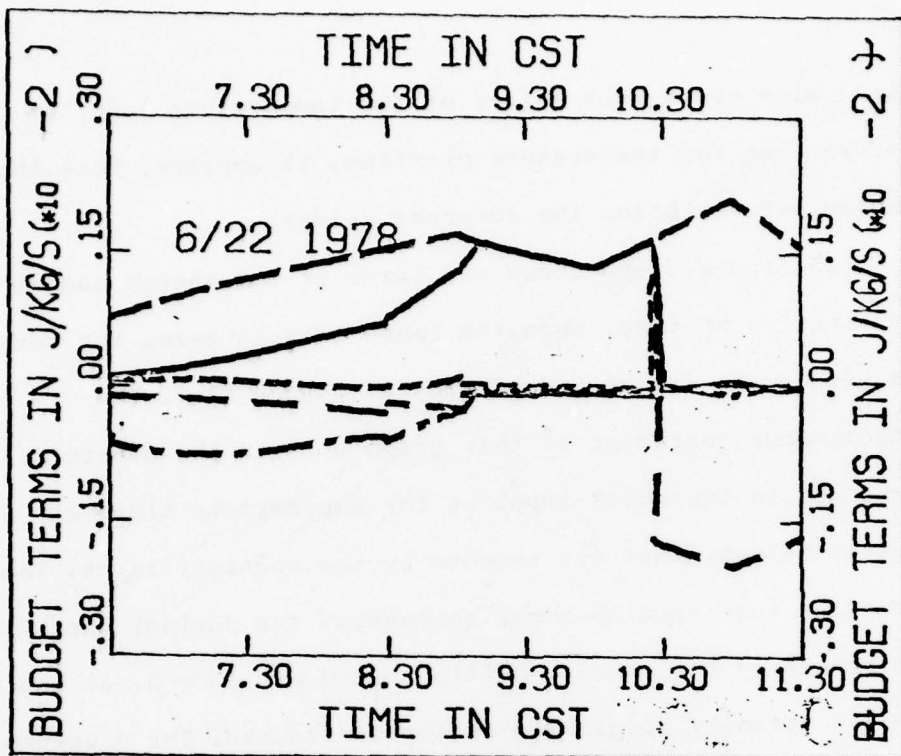


Figure 7:

The computed terms of the energy budget equation at the inversion base as a function of time on June 22 1978.

- the temporal term
- - - the buoyancy term
- - - the flux divergence term
- . - the dissipation term
- - - - the production term

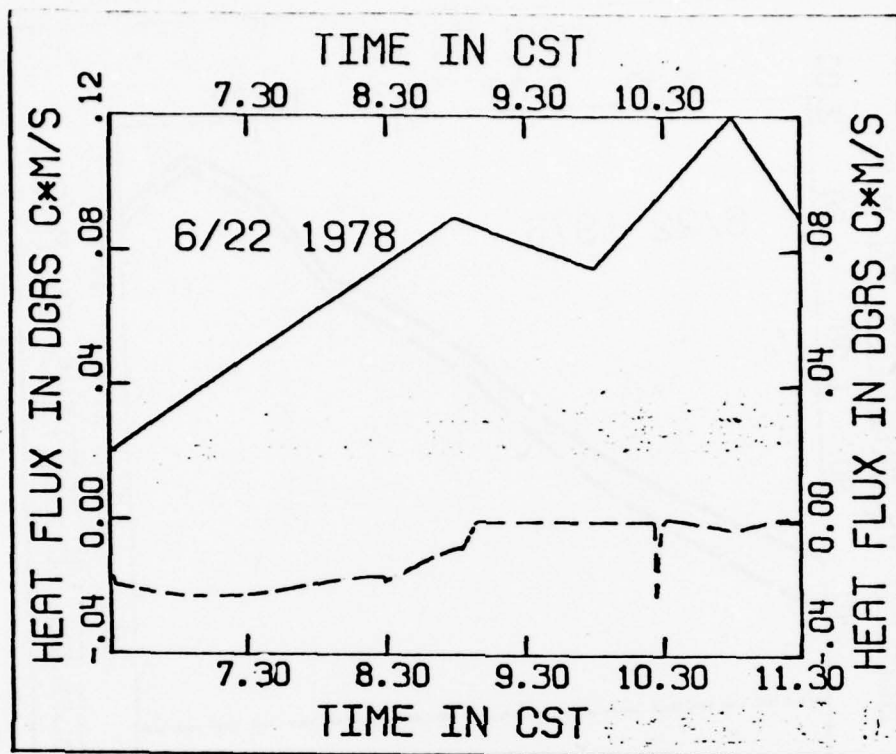


Figure 8:

The observed virtual surface heat flux and the computed virtual heat flux at the inversion base as a function of time on June 22 1978.

— the virtual surface heat flux

- - - the virtual heat flux at the inversion base

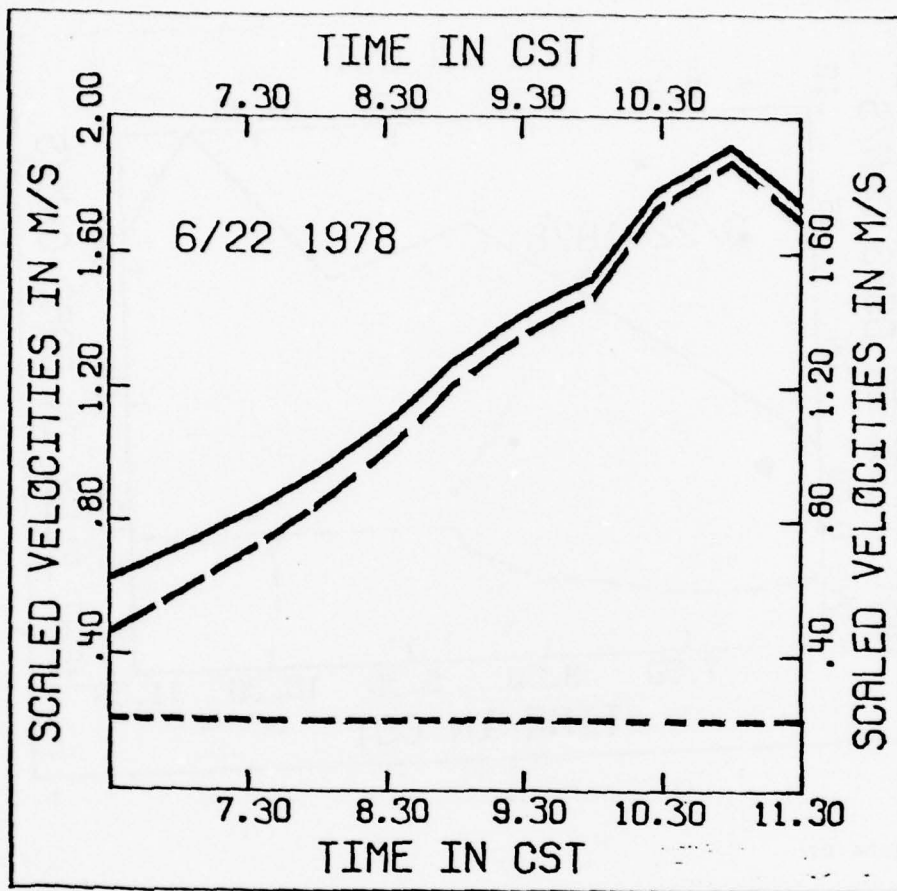


Figure 9:

The scaled velocities C , w^* and u^* as a function of time on June 22 1978.

——— C
 - - - w^*
 . . . u^*

The computed dissipation length (figure 10) increases from 50 m at the initial time to 110 m, when the layer reaches 400 m. Compared with the observed values, the model slightly overestimates the dissipation length. Between 600 m and 1600 m, when the lapse rate is zero, d is of the order of the mixed layer height. It appears, that the plumes, that are visible then have sizes, comparable to the mixed layer height. The observed values of d are smaller, although they have the same order of magnitude. A comparison between theory and practice during this portion of the observation period is of no value, since the dissipation is of no importance during that time. When the layer stops growing at 1600 m, d is about 80 m, which is in agreement with the observations.

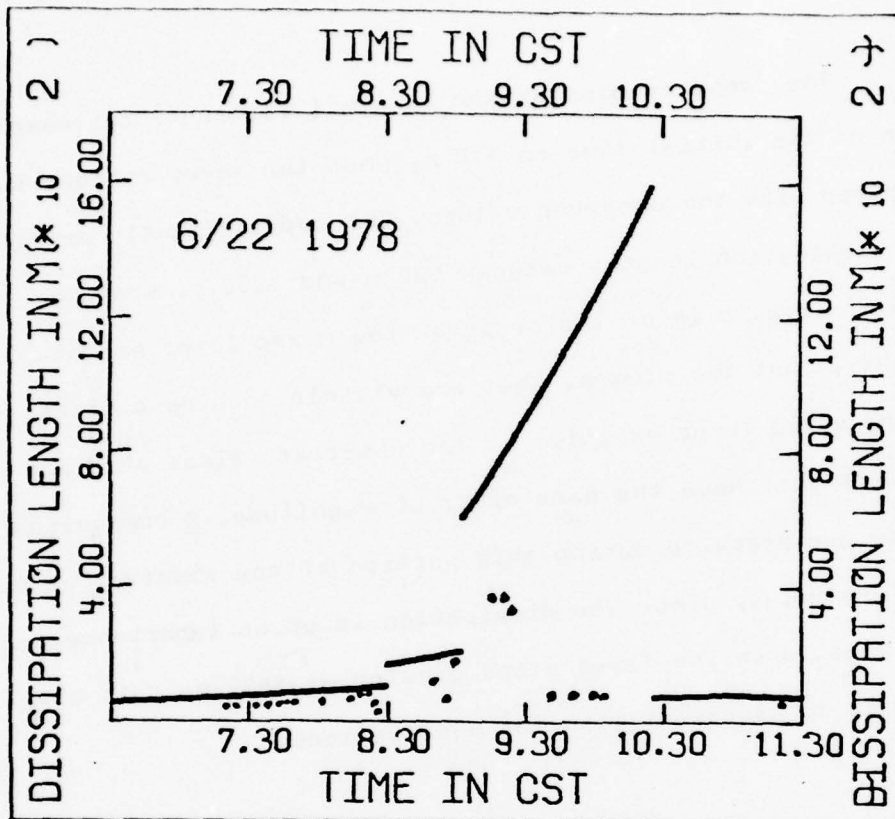


Figure 10:

The computed dissipation length at the inversion base as a function of time on June 22 1978. The • 's indicate the observed values from the lidar data.

2. CASE STUDY 2: JUNE 23 1978

From table 4, it is apparent, that the virtual heat flux is more than twice as big as the observed heat flux.

The lapse rate differs significantly from the previous day, June 22. There is a weakly stratified layer between 1000 m and 1500 m, characterised by a large aerosol content. This is probably left over from the previous day. The inversion at 1000 m could be due to subsidence, because, during both days, a region of high pressure was situated over the Great Lakes. ΔT_0 was estimated from run 3. The profiles of run 1, 2, and 3 were averaged to get the lapse rate above the inversion. Again, a low level jet existed during the early morning hours. Table 5 gives the input parameters of the model. The initial time was 700 CST, the final time was 1000 CST.

Figure 11-14 give some RHI-pictures, that were taken during the period. Clearly visible is the layer of enhanced scattering between 1000 and 1500 m. The attenuation correction, that was applied to the pictures, may have stressed the apparent wave motion in the upper layer. The highest altitude, the mixed layer reached was 1000 m. It was not capable of penetrating into the layer of enhanced scattering. Difficulty in estimating the inversion height was caused by the small change in aerosol content between the mixed layer and its environment, thus creating a rather diffuse boundary during some portions of the period.

Table 4:

Additional meteorological data for case study 2 (June 23 1978).

Listed are time, net solar radiation S , the heat flux H , the Bowen ratio B , the latent heat flux H_L , the moisture correction to the heat flux Δh , the fractional correction $\Delta h / H$, the virtual heat flux H_v , and the friction velocity u_* . All parameters are half-hourly averaged.

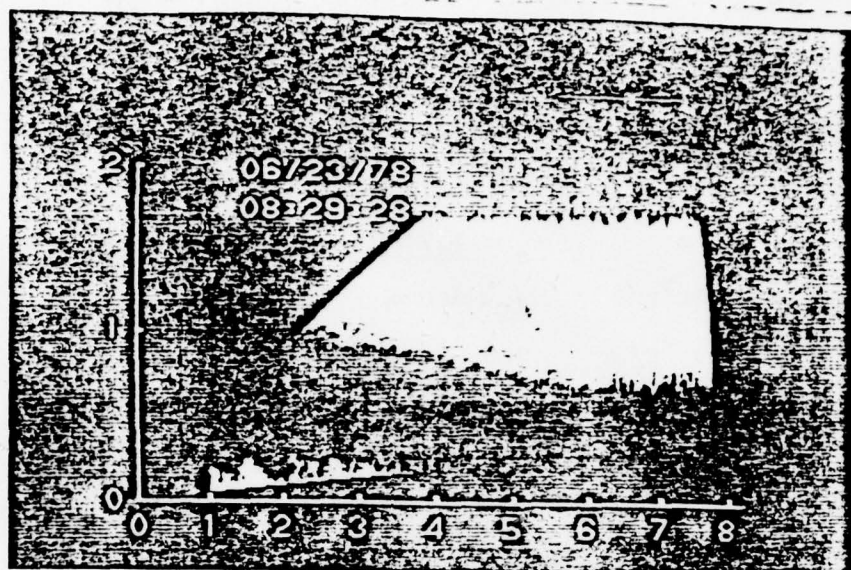
Time CST	S W/m^2	H W/m^2	B	L W/m^2	Δh W/m^2	$\Delta h/H$ 100	H_v W/m^2	u_* m/s
715	228	7	.03	233	17	242	24	.21
745	356	26	.09	289	21	80	47	.39
815	348	18	.06	300	22	122	40	.38
845	394	20	.06	333	24	109	44	.40
915	586	27	.05	540	40	148	67	.42
945	410	14	.04	350	26	185	40	.39
1015	388	19	.06	317	23	121	42	.45

Table 5:

Model input for case study 2 (June 23 1978)

$z_{io} = 150 \text{ m}$	$\Delta t_o = 1.7 \text{ } ^\circ\text{C}$	$\Delta U = 4.75 \text{ m/s}$	$u_y = .38 \text{ m/s}$
$\gamma = .002 \text{ } ^\circ\text{C/m}$	$z_i < 800 \text{ m}$		
$= .003 \text{ } ^\circ\text{C/m}$	$800 \text{ m} < z_i < 1000 \text{ m}$		
$= .0 \text{ } ^\circ\text{C/m}$	$z_i > 1000 \text{ m}$		
$s_x = -.005 \text{ s}^{-1}$	$z_i < 500 \text{ m}$		
$= .0 \text{ s}^{-1}$	$500 \text{ m} < z_i < 800 \text{ m}$		
$= -.025 \text{ s}^{-1}$	$800 \text{ m} < z_i < 1000 \text{ m}$		
$= .0 \text{ s}^{-1}$	$z_i > 1000 \text{ m}$		
$(\overline{t_v'w'})_o = .02 + .0185/30 \text{ t } ^\circ\text{C m/s}$	$t < 30 \text{ min}$		
$= .0385 \text{ } ^\circ\text{C m/s}$	$t > 30 \text{ min}$		
t_o is at 700 CST			

height (km)



range (km)

Figure 11:

RHI-picture, taken on June 23 1978 at 8.29 CUT.

The boundary layer is very thin, so that the averaging range is small (2 km). The apparent wave motion in the upper layer could be due to slope corrections applied to the picture..

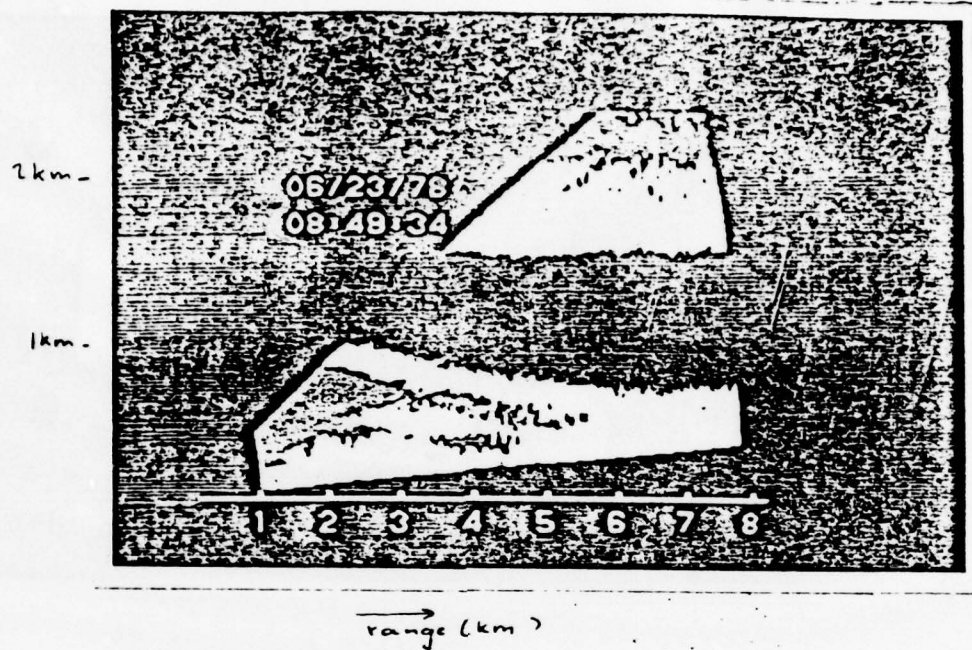
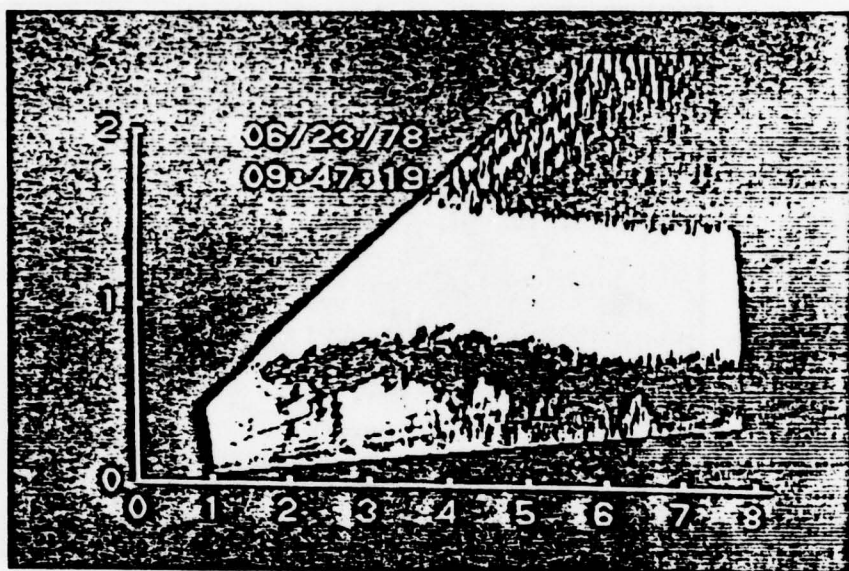


Figure 12:

RHI-picture, taken on June 23 1978 at 8.50. CUT.

The boundary layer has increased in depth. Note the wave motion at the top of the boundary layer.

height (km)



range (km)

Figure 13:

RHI-picture, taken on June 23 1978 at 9.47 CDT.

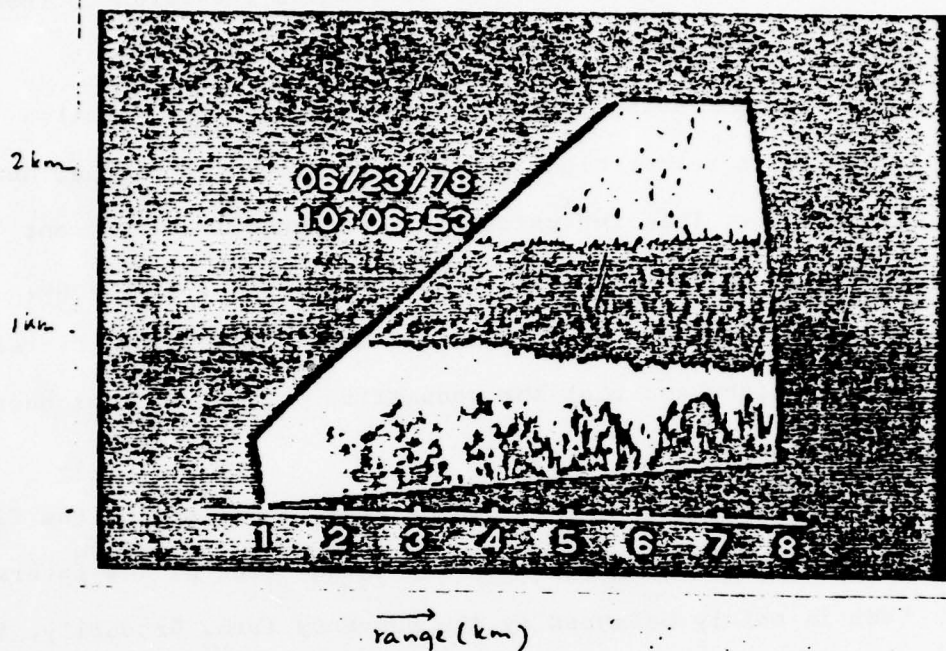


Figure 14:

RHI-picture, taken on June 23 1978 at 10.07 LDT.

Four plumes are visible, with smaller areas inbetween, where air is entrained downwards.

The inversion rise, as computed, is too small(figure 15). The computed temperature jump across the inversion decreases somewhat faster than as was observed (figure 16).

In comparison with the previous day, the friction velocity is rather high. At the same time, the virtual heat flux is low. This indicates, that mechanical entrainment should be more important. Indeed, figure 17 and 18 show, that the magnitude of the virtual heat flux at the inversion base is high, and that the convective part of σ_w has decreased in influence.

From figure 19, it can be seen, that, during the first hours, the divergence of kinetic energy flux at the inversion base is mainly balanced by the buoyancy term. Gradually, the dissipation becomes more important until it equals the buoyancy term.

A problem in estimating the dissipation length was the diffuse boundary between the mixed layer and its environment. At the end of the period, the mixed layer reached the upper layer of enhanced scattering, thus creating an extra difficulty in estimating the length scale. Therefore, only a few reliable values could be obtained. The computed length scale increases from 90 m at the initial time to 175 m, when the layer hit 800 m. The observed values are smaller, but are well within the same order of magnitude.

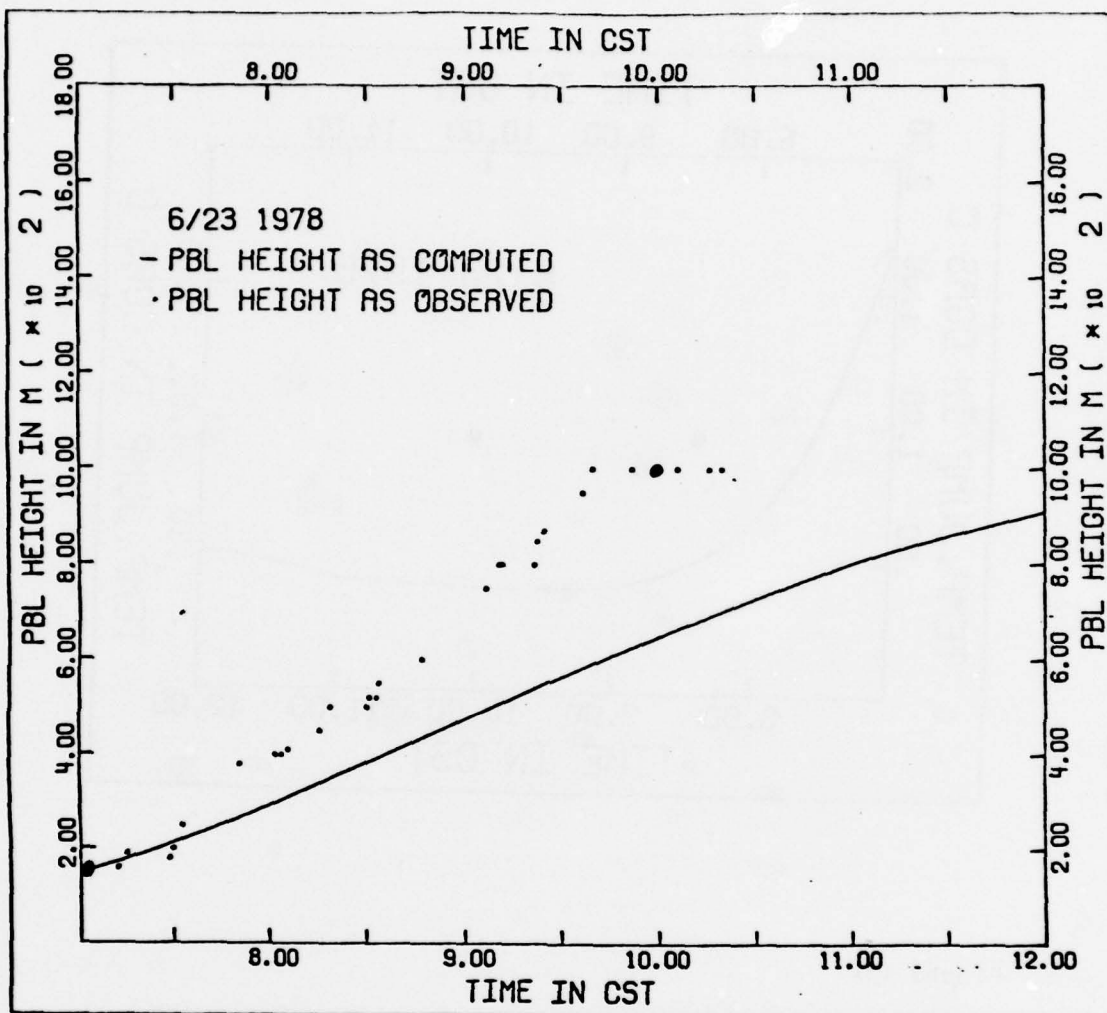


Figure 15:

The observed and the computed inversion height as a function of time on June 23 1978. The •'s indicate the inversion height as observed in the temperature profiles.

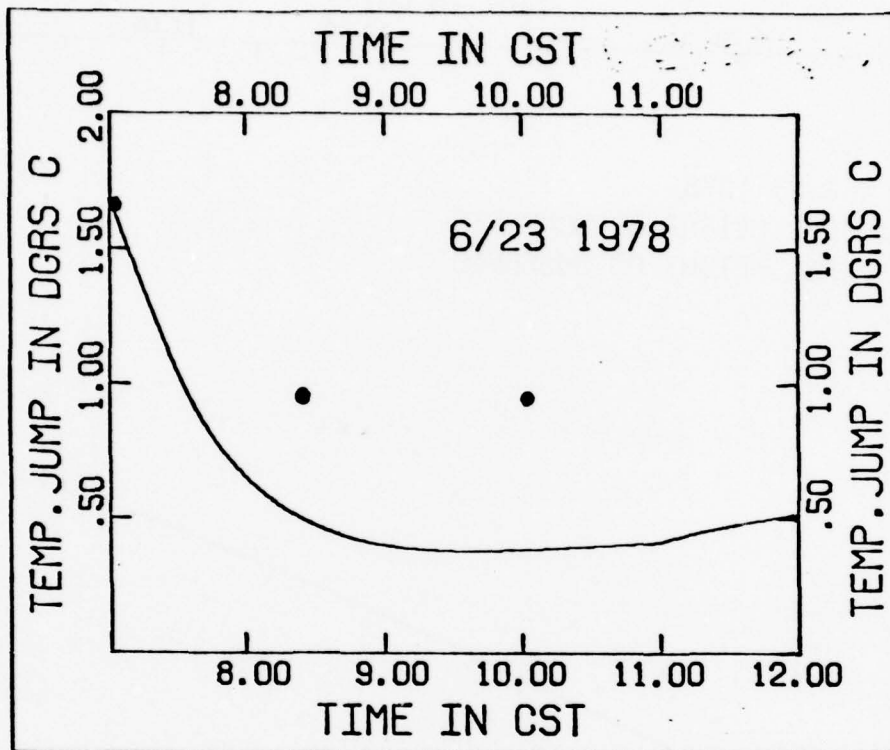


Figure 16:

The computed temperature jump as a function of time on June 23 1978. The •'s indicate the observed values in the temperature profiles.

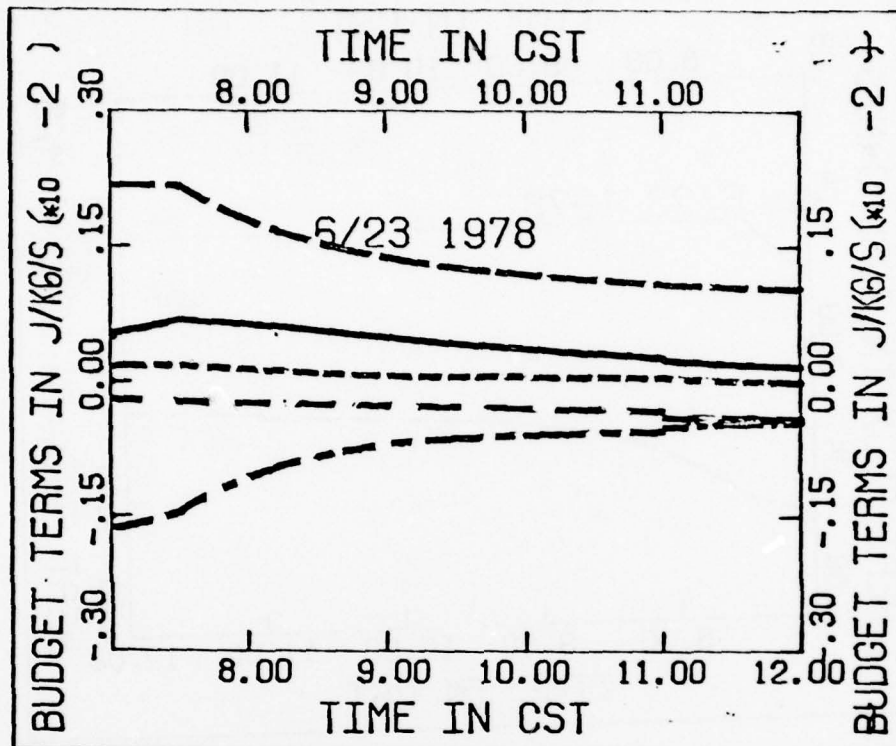


Figure 17:

The computed terms of the energy budget equation at the inversion base as a function of time on June 23 1978.

- the temporal term
- ... the buoyancy term
- - - the flux divergence term
- - - the dissipation term
- . - the production term

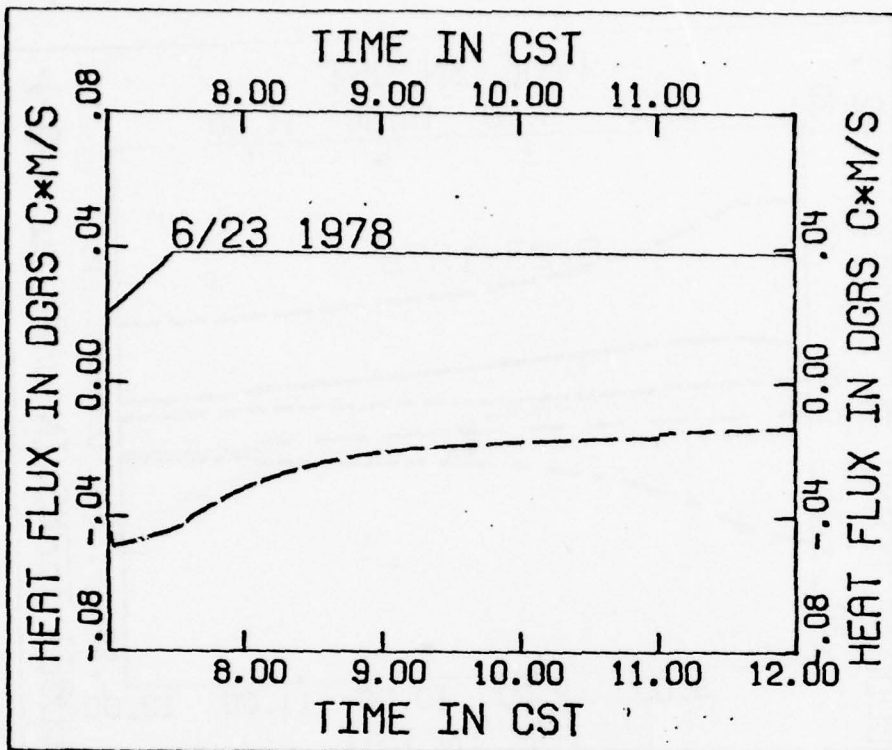


Figure 18:

The observed virtual surface heat flux and the computed virtual heat flux at the inversion base as a function of time on June 23 1978.

—— the virtual surface heat flux

- - - - the virtual heat flux at the inversion base.

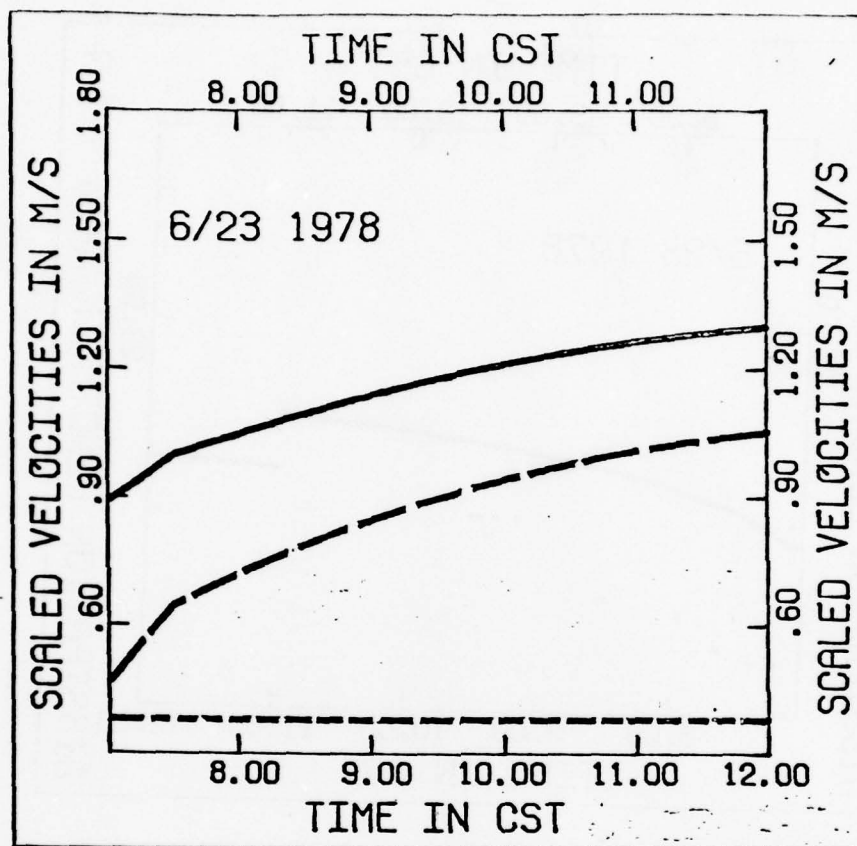


Figure 19:

The scaled velocities c_w , w_* and u_* as a function of time on June 23 1978.

— c_w
 --- w_*
 - - - u_*

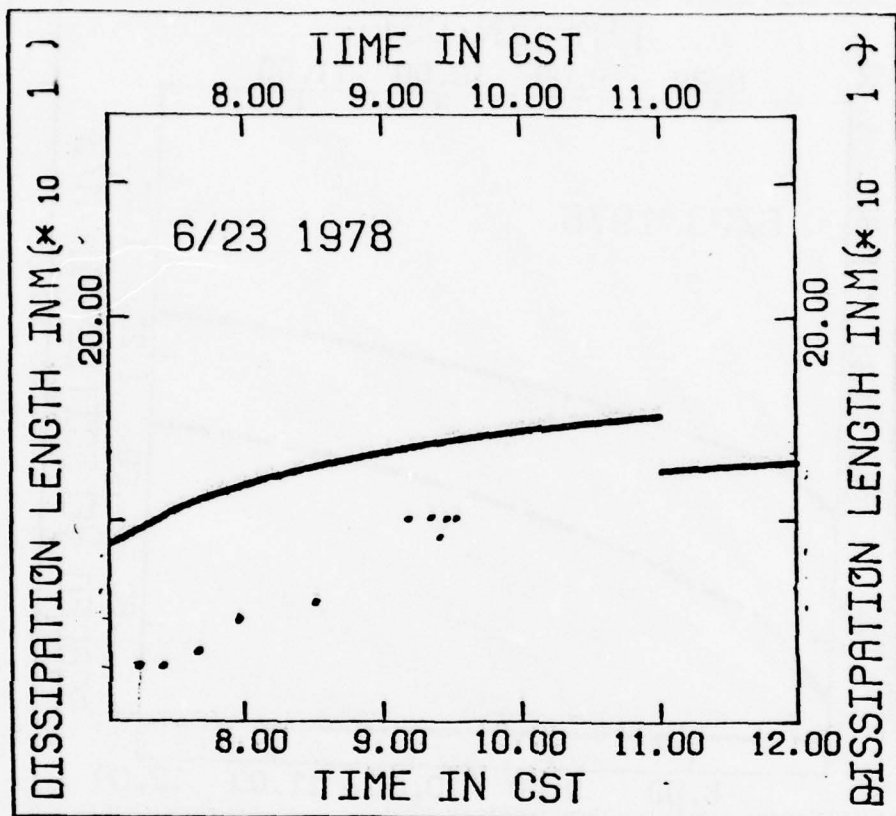


Figure 20:

The computed dissipation length at the inversion base as a function of time on June 23 1978. The . 's indicate the observed values from the lidar data.

The model was run for a period of 5 hours, although the data input stops after 3 hours at 1000 CST.

The lidar system can be used to obtain estimates of the wind speed in the boundary layer (Leuthner and Eloranta, 1977, Kunkel, 1978, Sroga, in preparation). Aerosol is a passive contaminant of the atmosphere and its displacement is a measure of the wind speed. After scanning the laser at 3 azimuth angles, cross correlations (range and time) of the shot profiles were computed. This provided estimates of the wind speed at different heights in the boundary layer, that were compared with the available wind profiles. Figure 21 and 22 show, that the computed wind speeds match the data remarkably well. Visible is the decrease of wind speed at 400 m, indicating the break-down of the low-level jet.

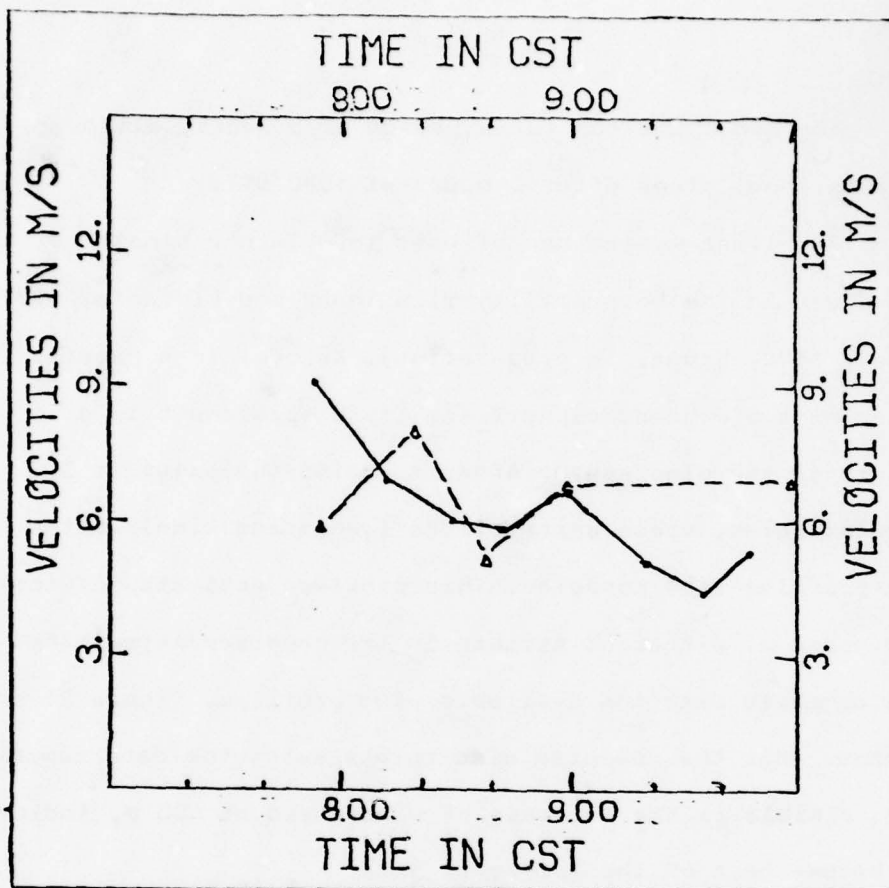


Figure 21:

Comparison of computed wind speed (averaged between 185 and 235 m altitude) and the observed wind speed at 200 m as a function of time on June 23 1978.

— the computed wind speed
 - - - the observed wind speed

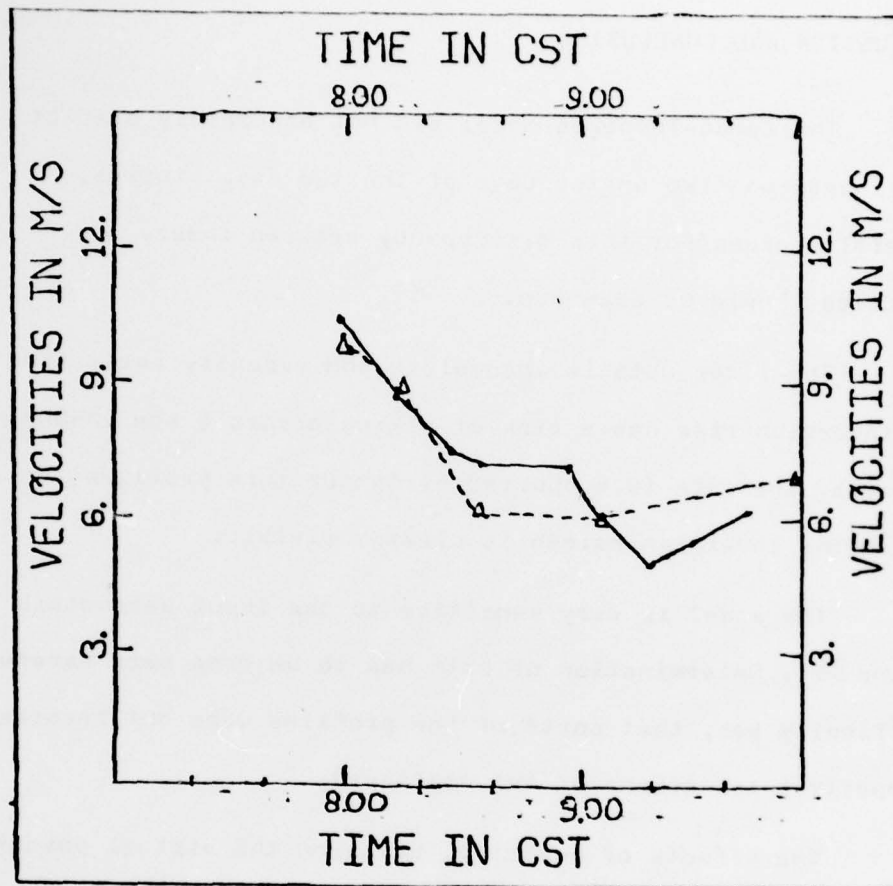


Figure 22:

Comparison of computed wind speed (averaged between 385 and 435 m altitude) and the observed wind speed at 400 m as a function of time on June 23 1978.

— the computed wind speed
 - - - the observed wind speed

DISCUSSION AND CONCLUSION

The Zeman-Tennekes model did not accurately predict the inversion rise on the days of the two case studies. Several reasons for this discrepancy between theory and practice should be examined.

The lidar data is incomplete and visually estimating an inversion rise has a risk of making errors (see ERRORS..). However, the data is supported by temperature profiles, on which the inversion height is clearly visible.

The model is very sensitive to the input parameters γ and Δt_0 . Determination of both has to be done very carefully. Difficulty was, that parts of the profiles were not recorded properly (see graphs of the profiles).

The effects of humidity, by using the virtual potential temperature as a function of height, were not taken into account. No humidity profiles were available.

The model constants were computed from only few laboratory experiments. It is possible, that they have to be adjusted for atmospheric experiments. It makes no sense to adjust the constants with the few data, that is available here. On June 23, mechanical entrainment is more important than on June 22, and the computed entrainment of June 22 matches the data better than the computation of June 23. Therefore it could be, that the effect of mechanical

entrainment is somewhat underestimated. This means, that the constant η , which has the value of two in the original description of the model, has to be adjusted. In order to see the effect of the constant, the model was rerun for both days with $\eta = 4$. It appears, that on June 22, the computed entrainment matches almost completely the observed entrainment. On June 23, the entrainment is overestimated during the first hours and underestimated during the last hour (see APPENDIX).

Besides the use in the determination of the inversion height, the lidar data can provide estimates of the plume penetration depth, which is an important model parameter. From the scarce data, that is available here, there is an indication, that the plume penetration depth is overestimated by the model. Therefore, the dissipation at the inversion base could be underestimated. The dissipation process, that hampers the growth of the mixed layer, appeared to be unimportant during the growth phase of the boundary layer. Since the model underestimates the inversion rise anyway, no direct conclusions can be given on the parametrization of the dissipation length. In favour of the validity of the parametrization is, that on June 22, the boundary layer stops growing at the appropriate height, which is due to the sudden increase of the dissipation.

The case studies do not prove, that the model is not working. They show, that lidar is probably the tool to overcome the lack of continuous data segments in testing inversion rise models. Clearly, further studies are necessary. During future experiments at the University of Wisconsin, it is necessary to obtain measurements of the latent heat flux, and of humidity profiles. As the case studies show, the correction to the observed heat flux can be of the order of 100%.

APPENDIX

The constant η combines the mechanical part of C'_w with the convective part. The value of this constant therefore influences the effect, that mechanical entrainment has compared to the convective entrainment. Its influence in the model equations is rather complex, since C'_w affects all terms but one of the energy budget equation. The value, originally given to η is two. To see the effect of η on the entrainment process the model was rerun with $\eta=4$. The computed entrainment of June 22 matches the observed entrainment rather well (figure 23). The entrainment rate on June 23 is overestimated during the first hour and underestimated during the last hour (figure 24). As more data becomes available, a better value of η could be obtained.

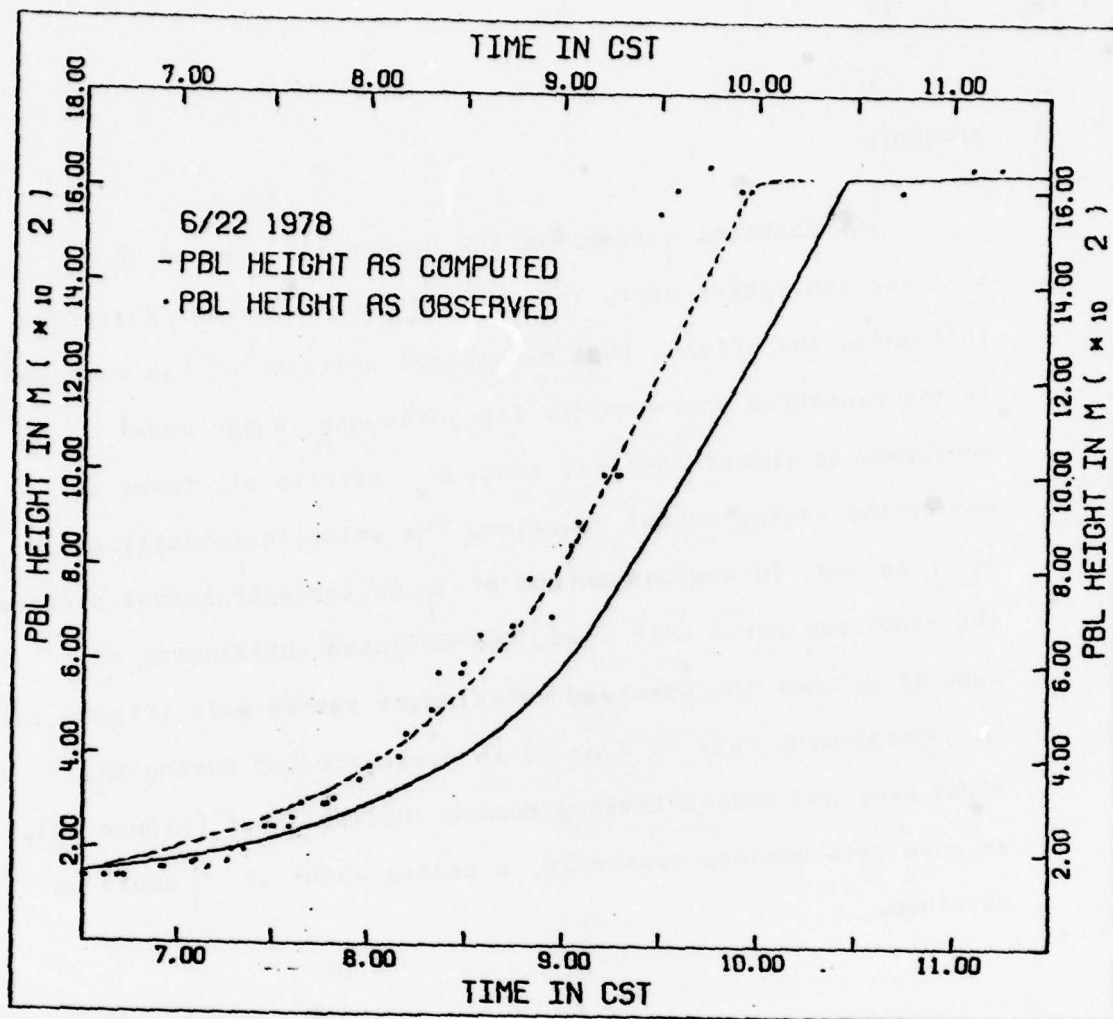


Figure 23:

The effect of η on the computation of the inversion rise on June 22.

- model run with $\eta=2$
- - - model run with $\eta=4$

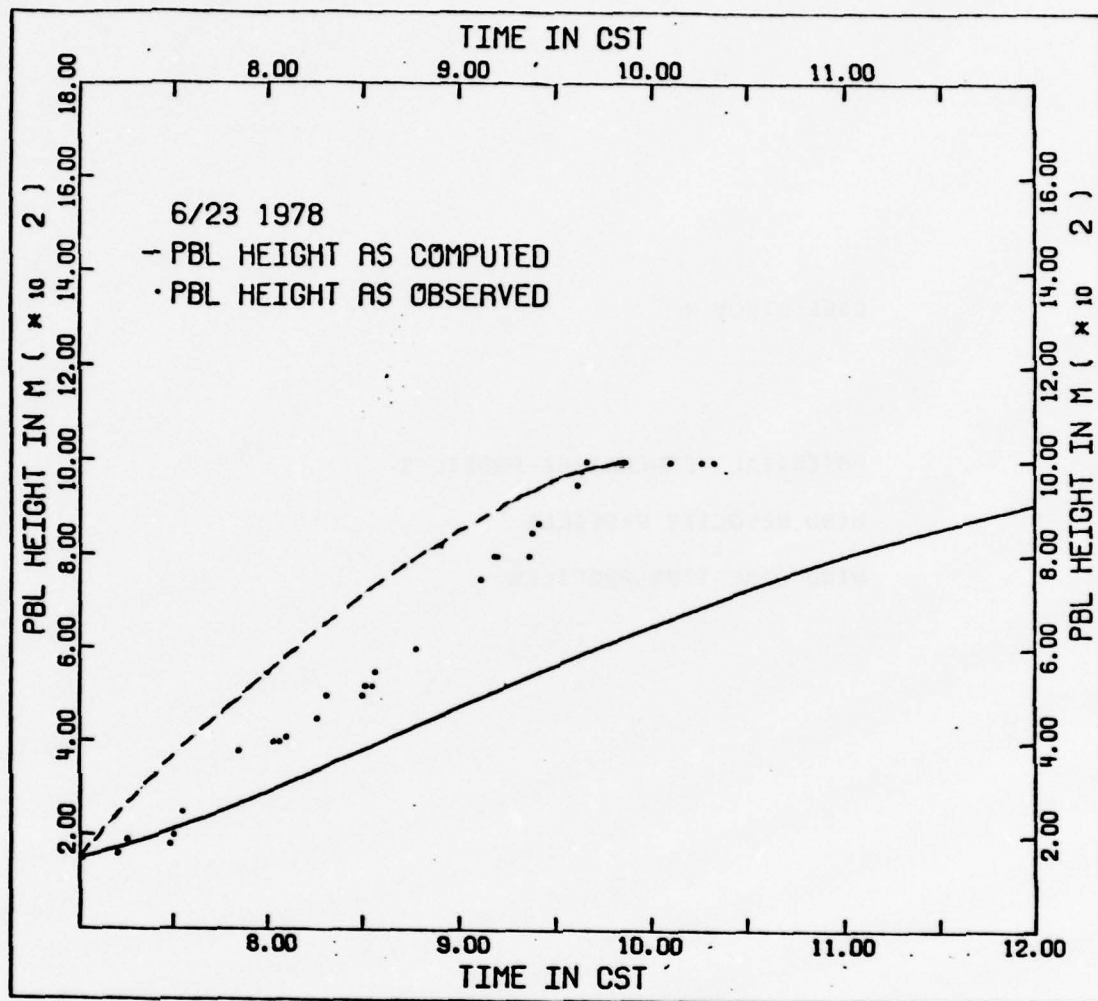


Figure 24:

The effect of η on the computation of the inversion rise on June 23.

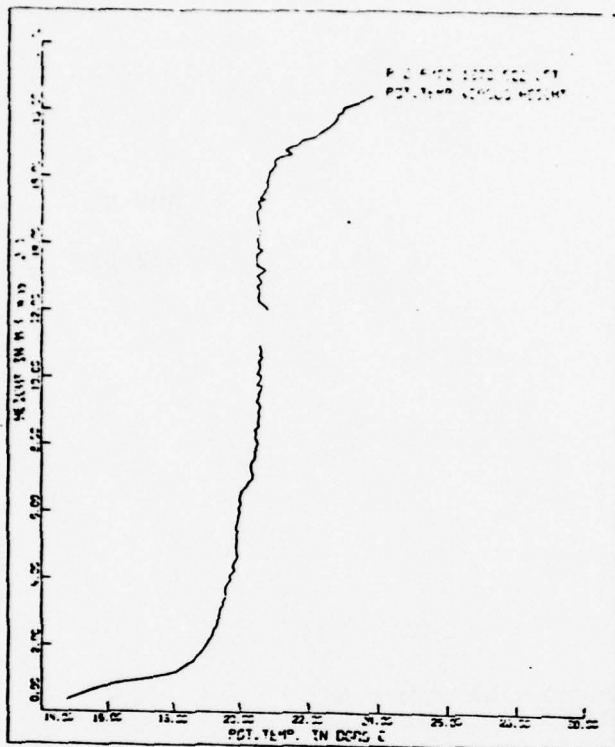
- model run with $\eta=2$
- - - model run with $\eta=4$

CASE STUDY 1

POTENTIAL TEMPERATURE PROFILES

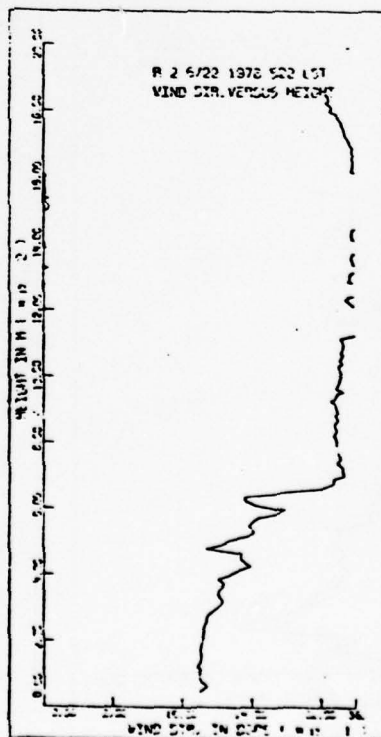
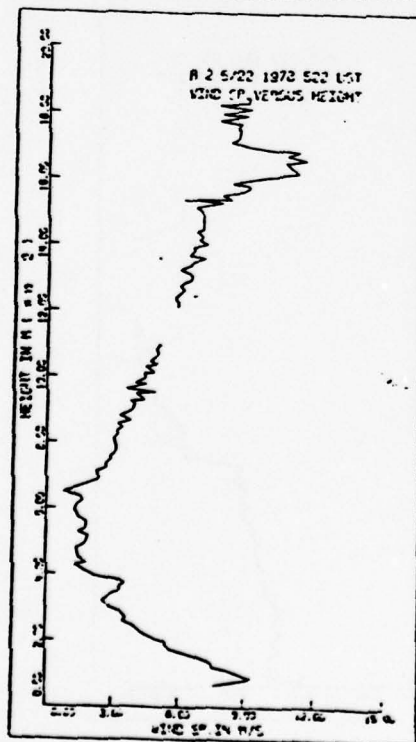
WIND VELOCITY PROFILES

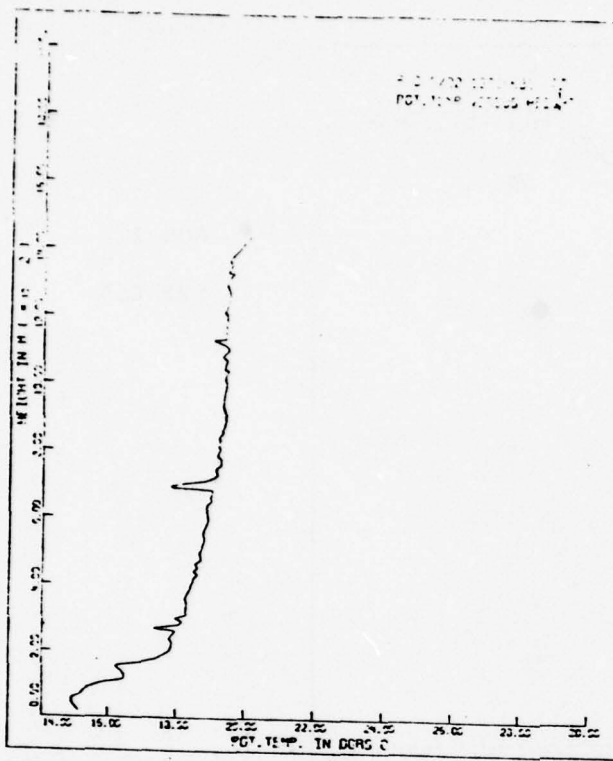
WIND DIRECTION PROFILES



RUN 2

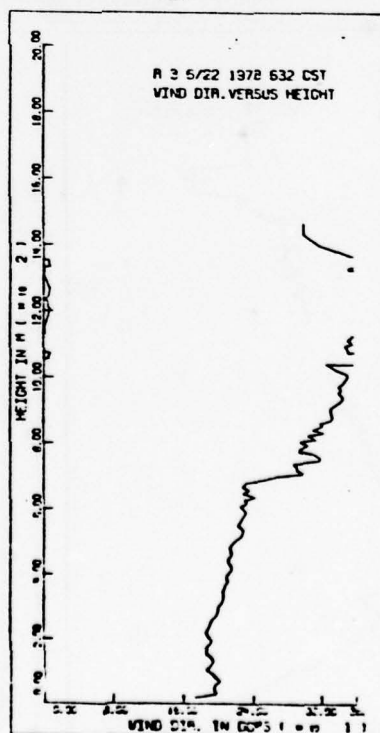
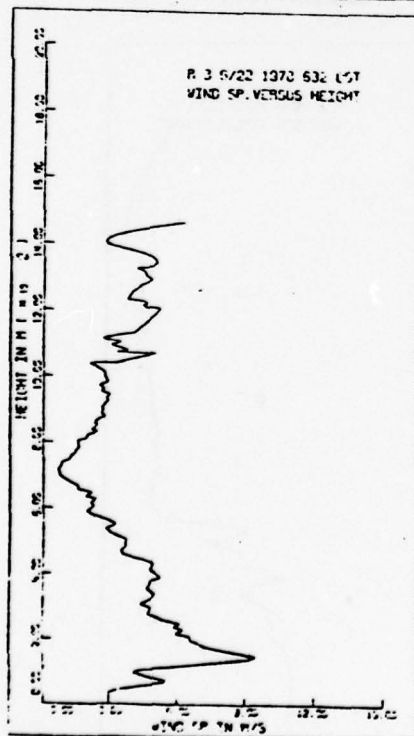
522 CST

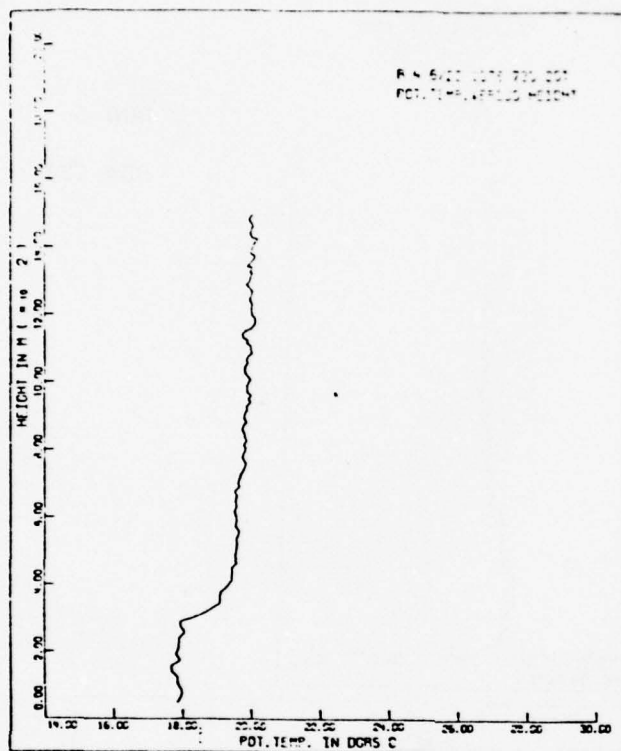




RUN 3

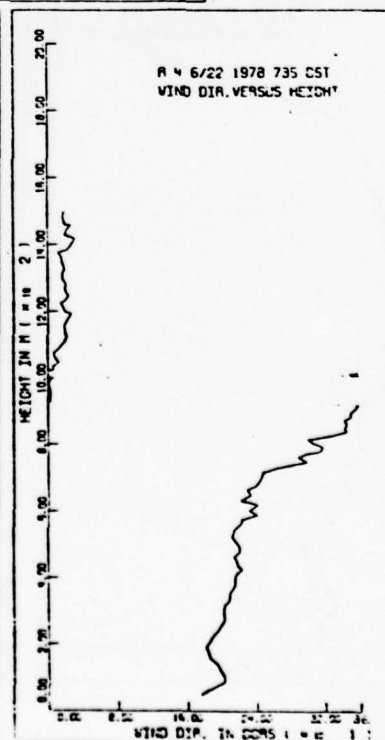
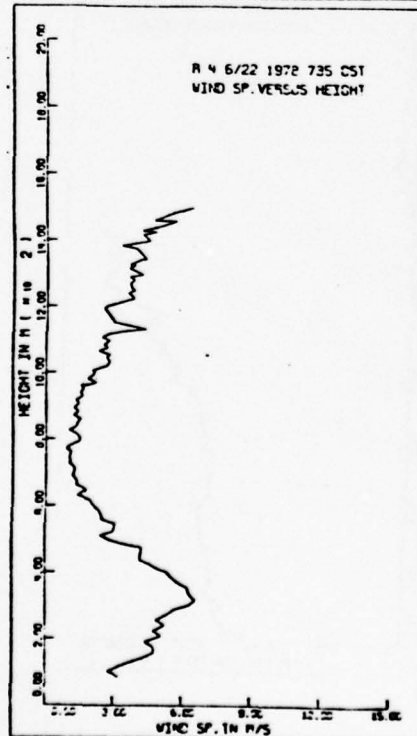
632 CST

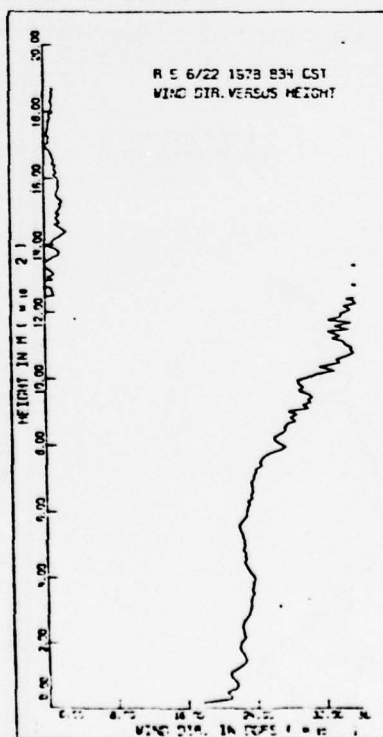
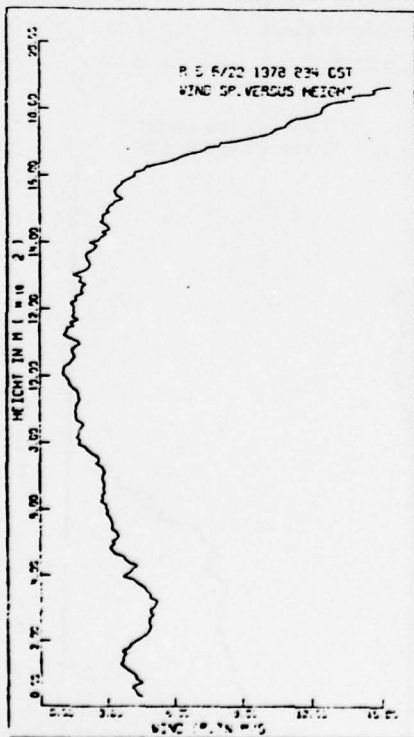
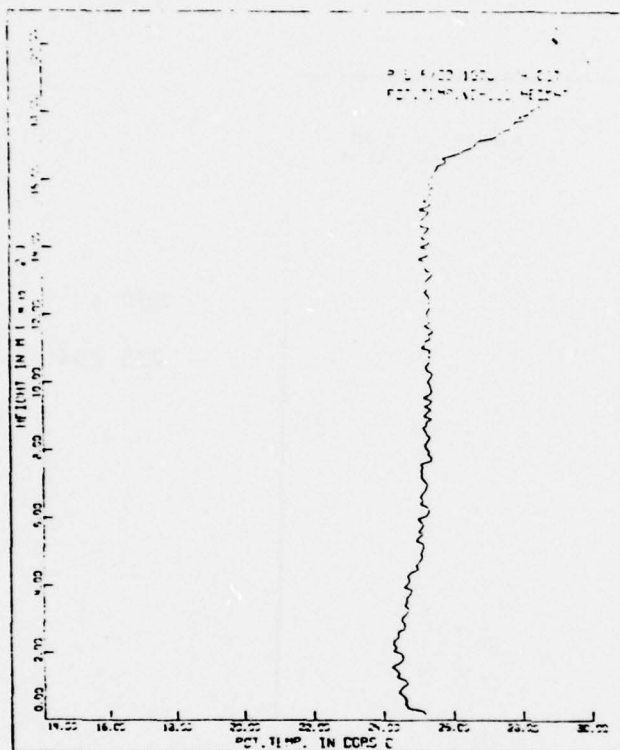


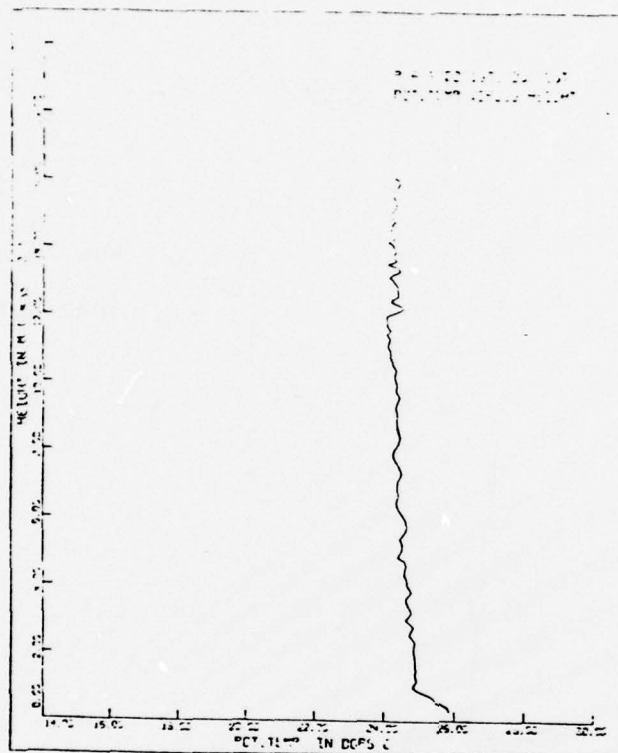


RUN 4

735 CST

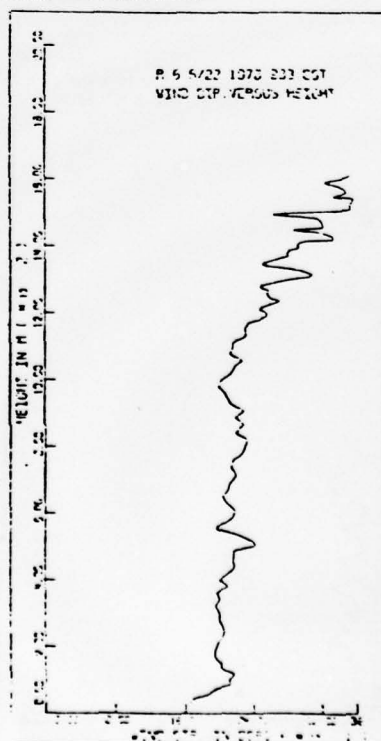
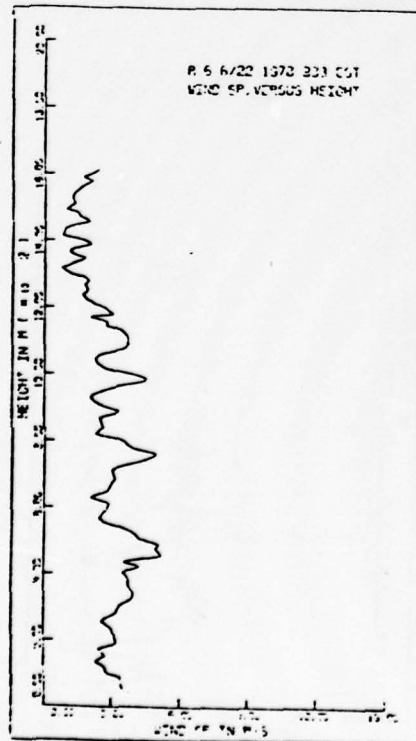


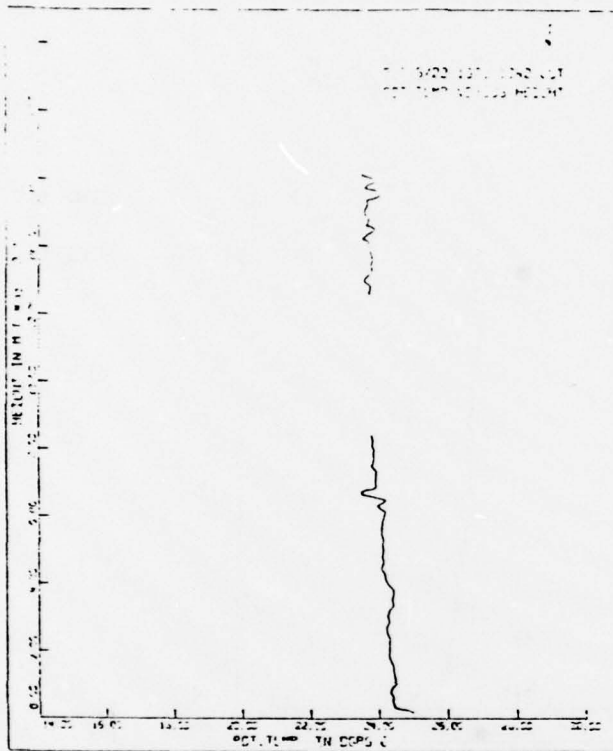




RUN 6

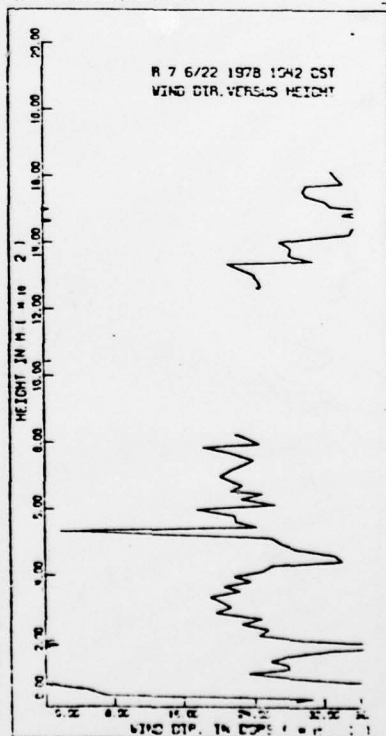
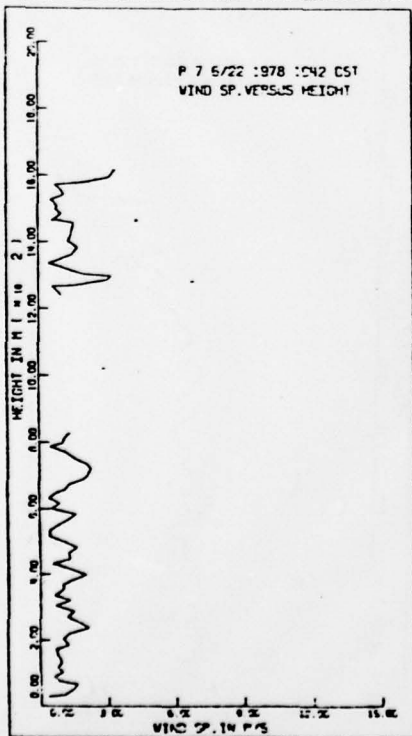
933 CST

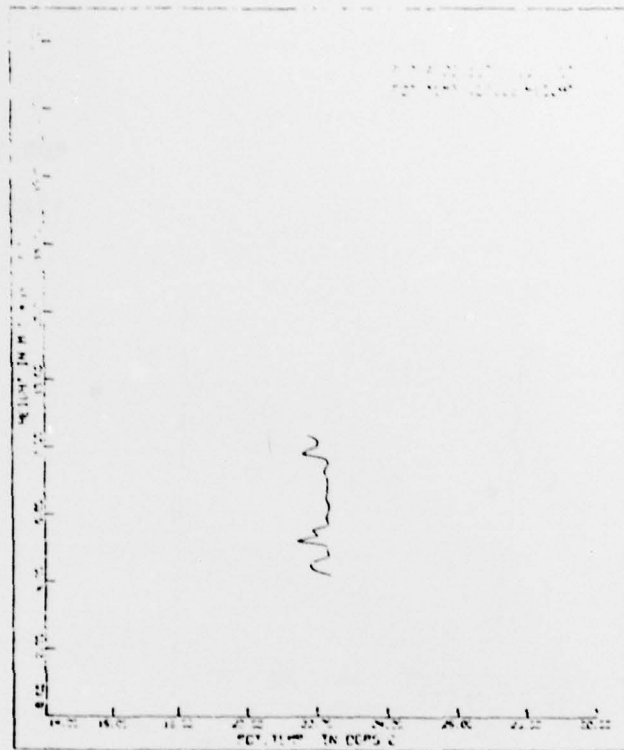




RUN 7

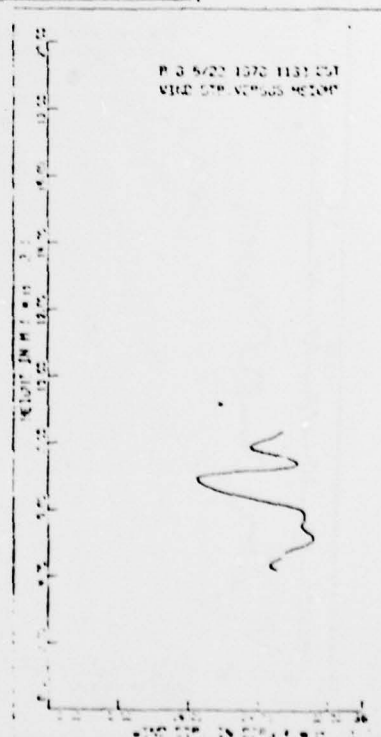
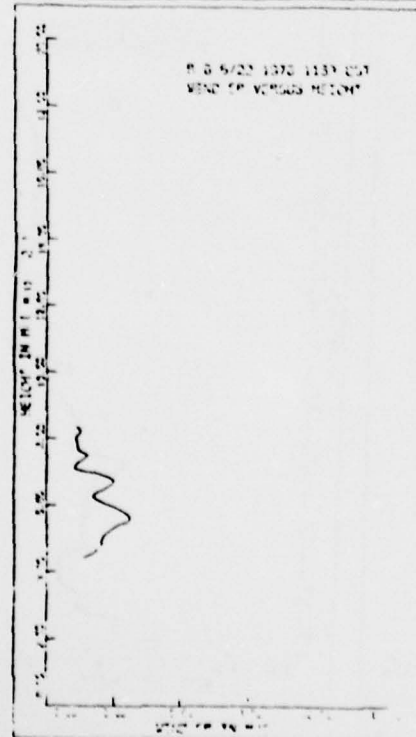
1042 CST

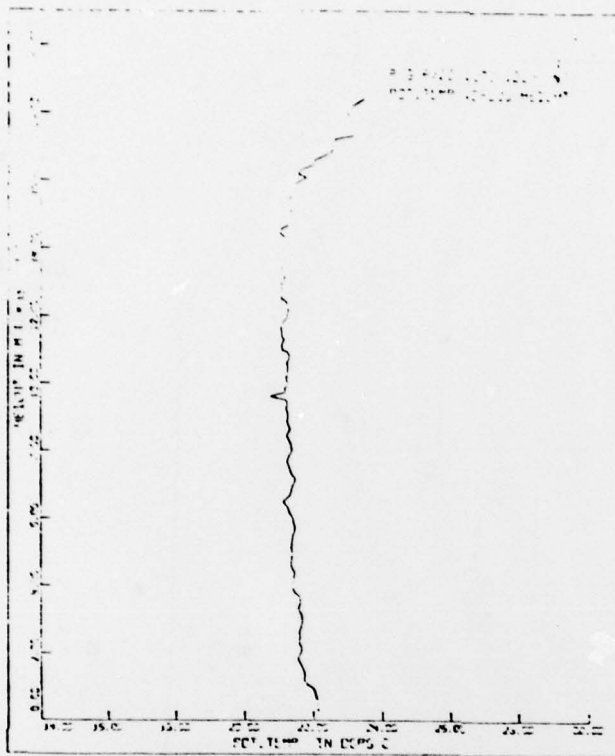




RUN 8

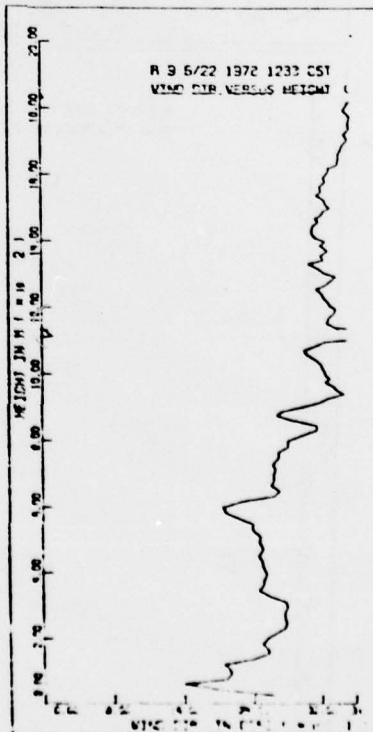
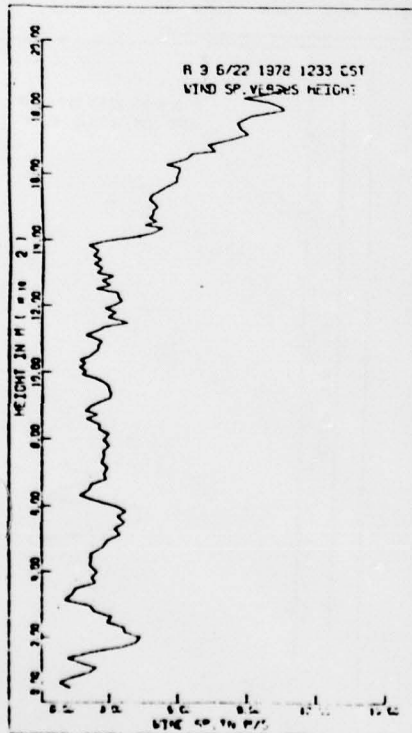
1133 CST





RUN 9

1233 CST

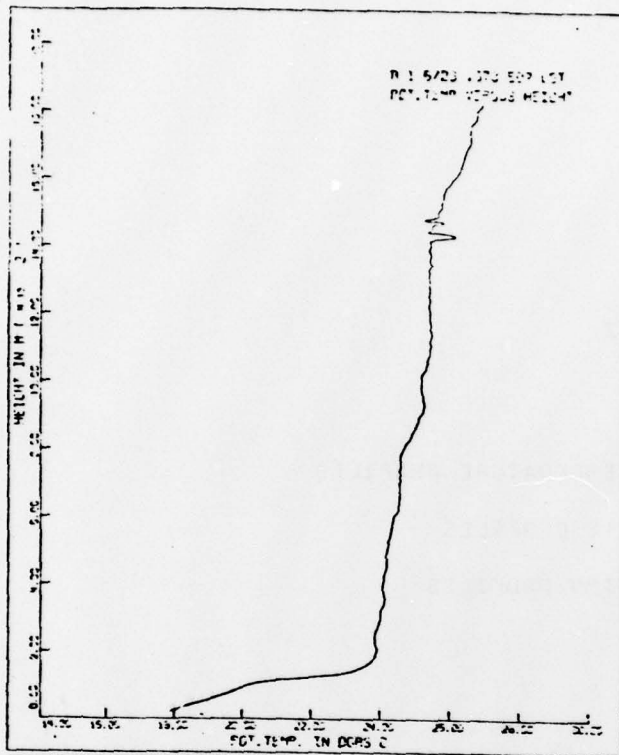


CASE STUDY 2

POTENTIAL TEMPERATURE PROFILES

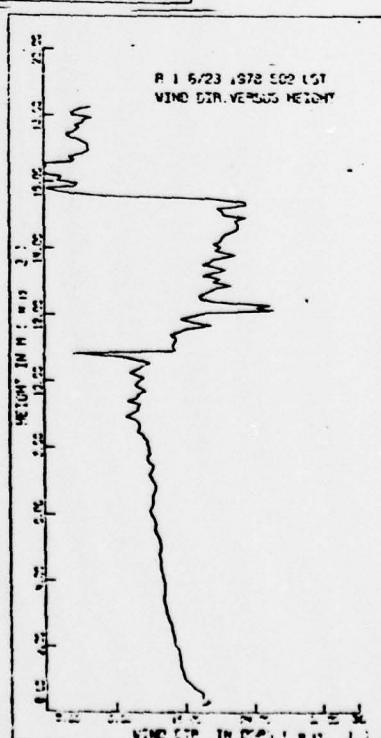
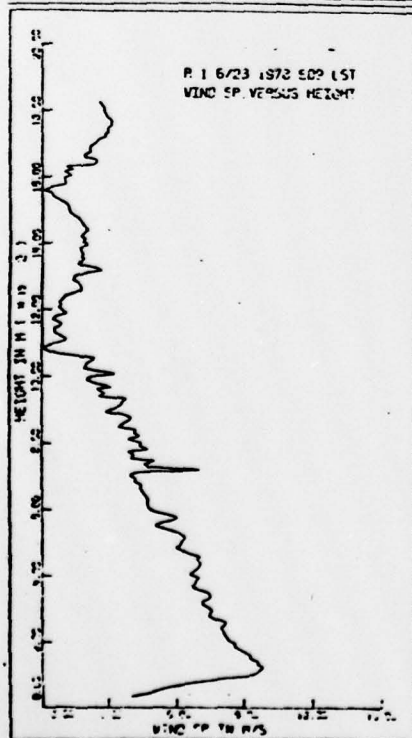
WIND VELOCITY PROFILES

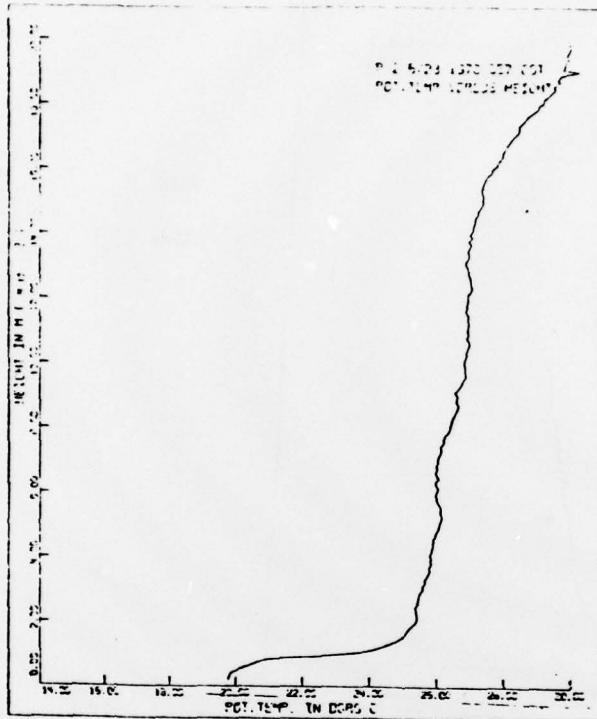
WIND DIRECTION PROFILES



RUN 1

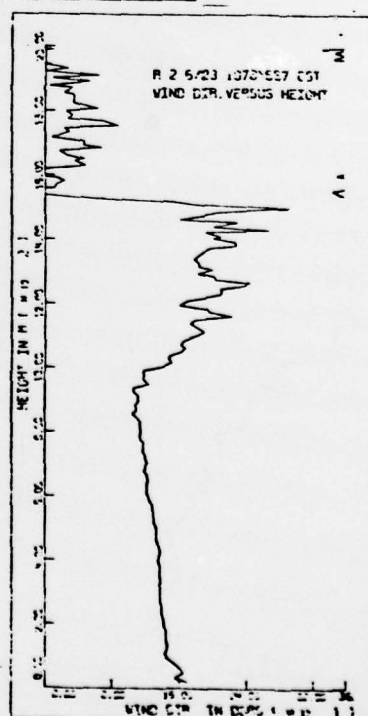
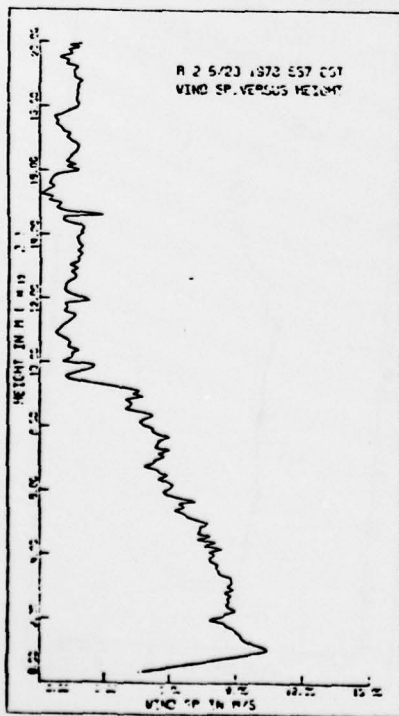
509 CST

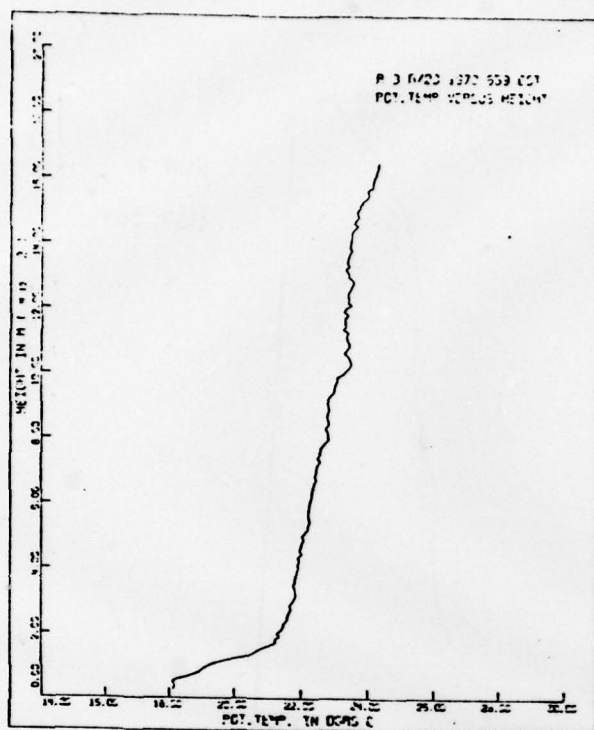




RUN 2

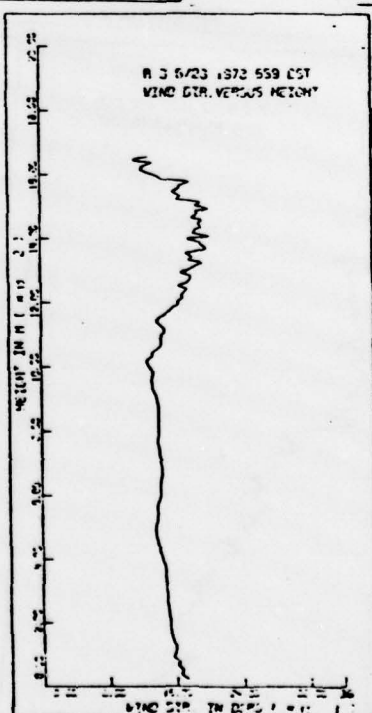
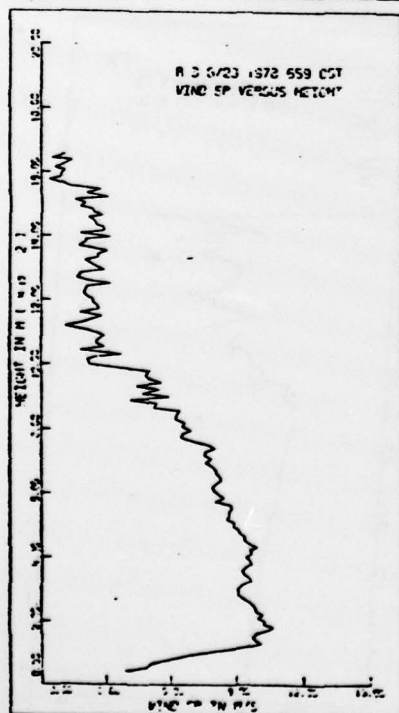
557 CST





RUN 3

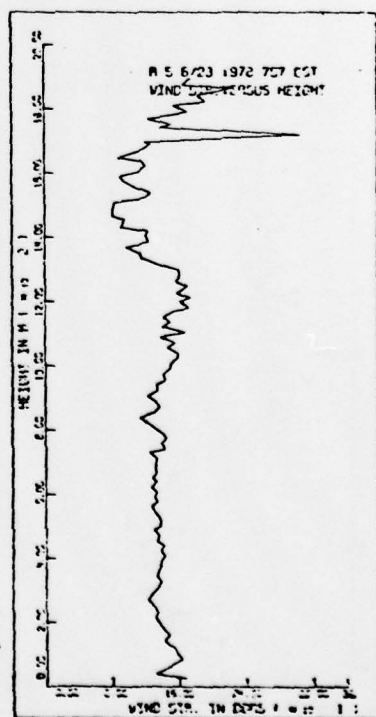
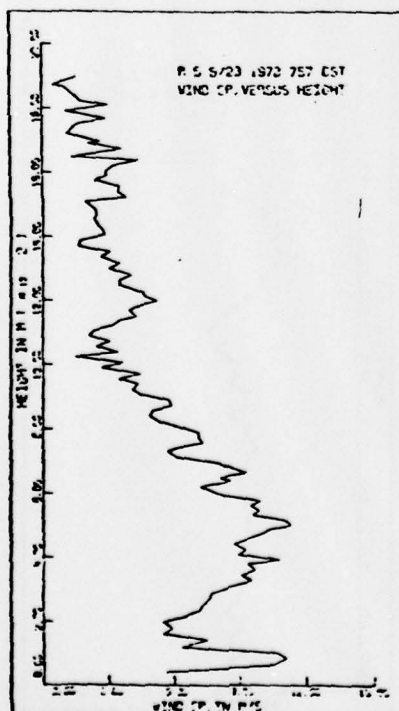
659 CST



RUN 5

757 CST

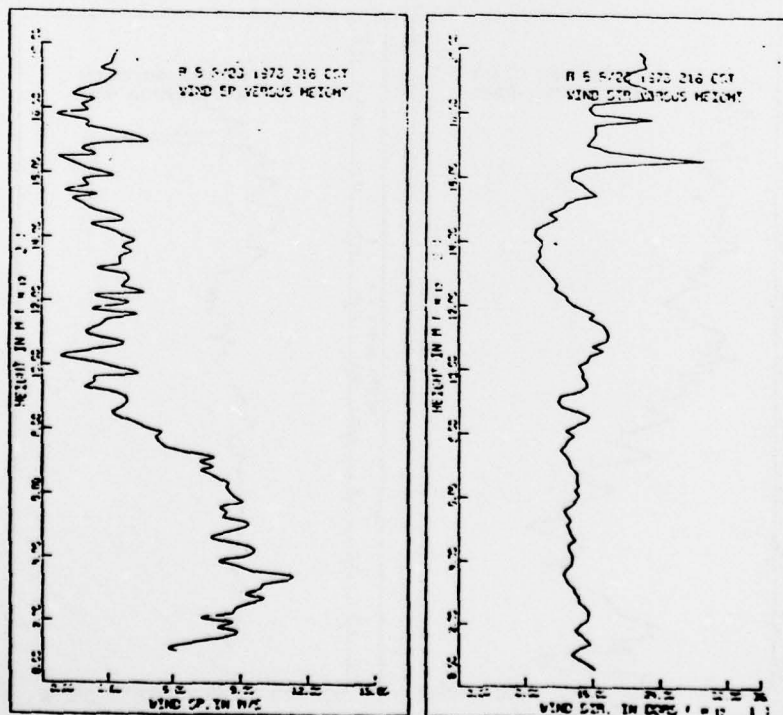
no temperature profile available

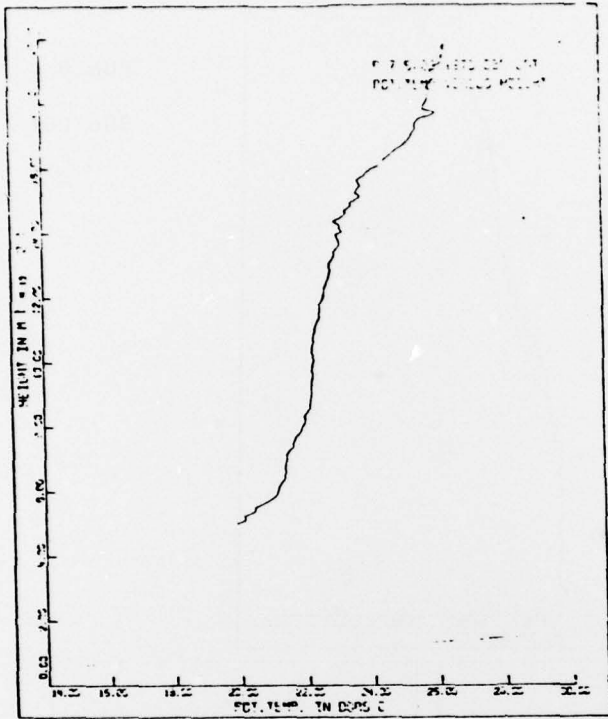
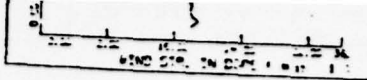
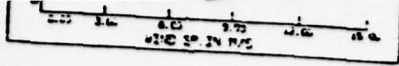


RUN 6

818 CST

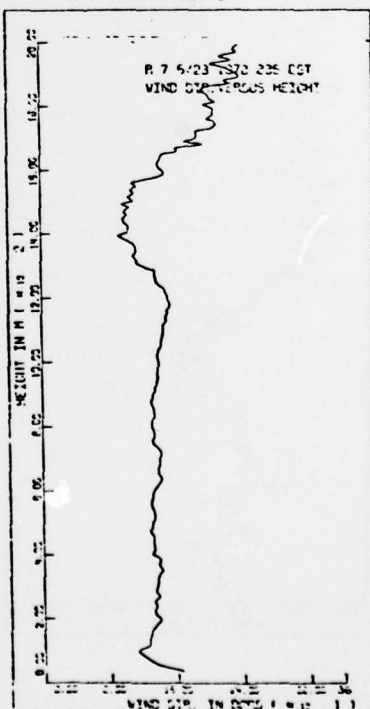
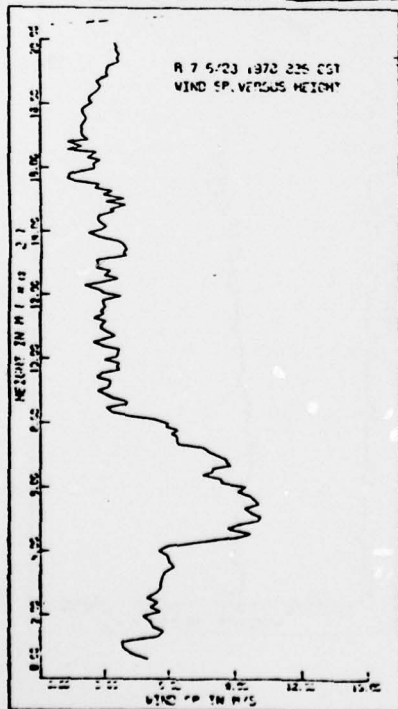
no temperature profile available

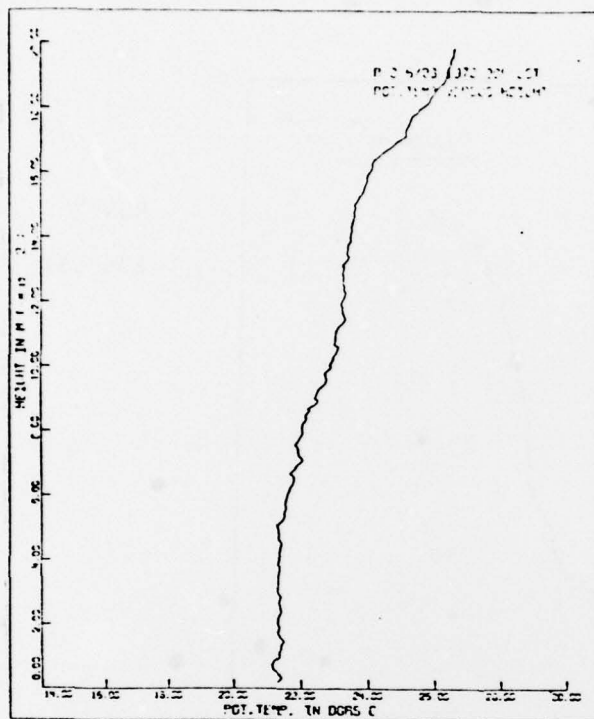
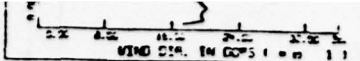
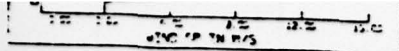




RUN 7

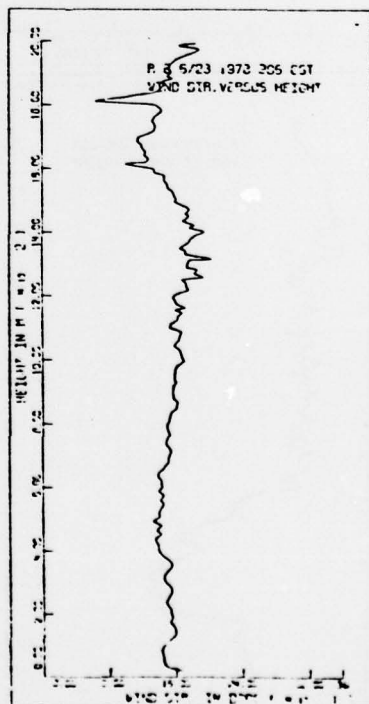
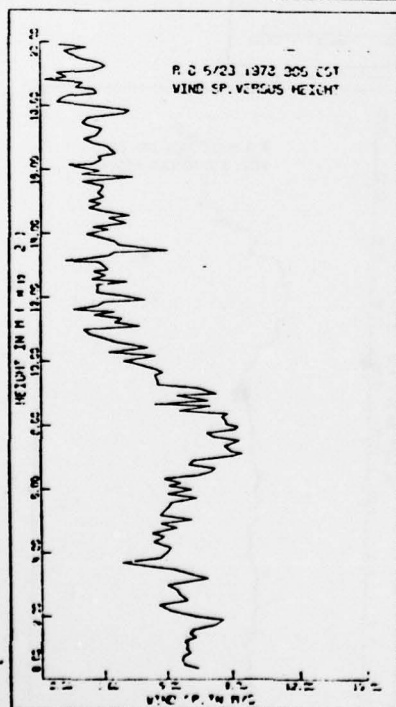
836 CST

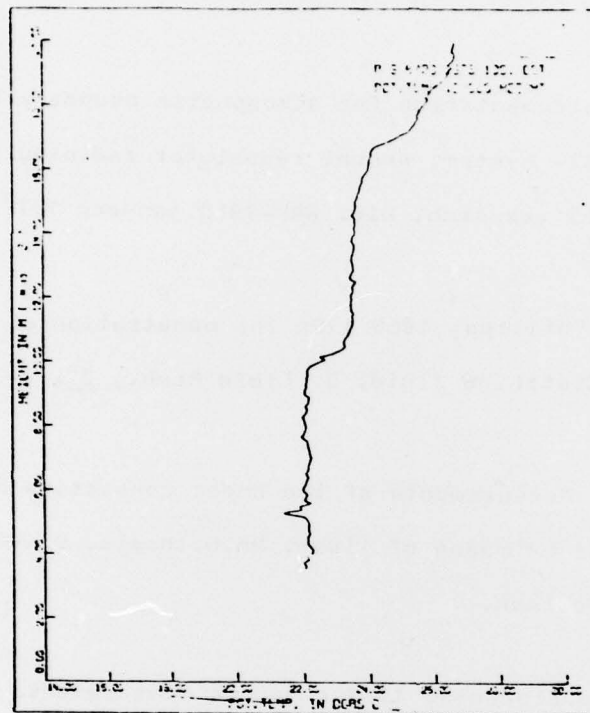
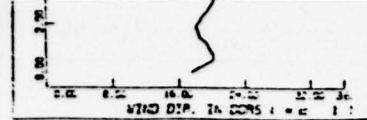
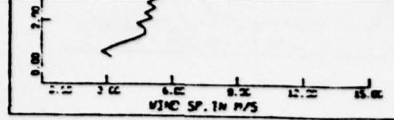




RUN 8

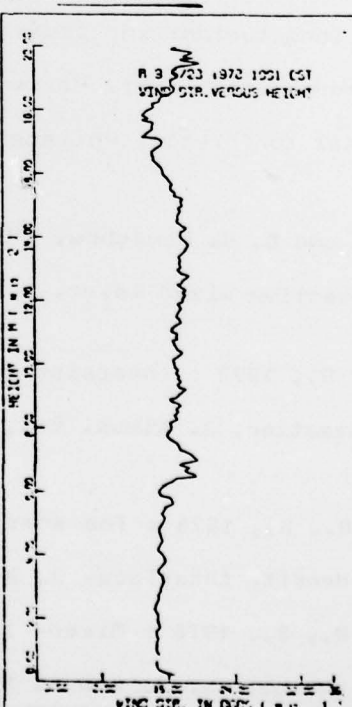
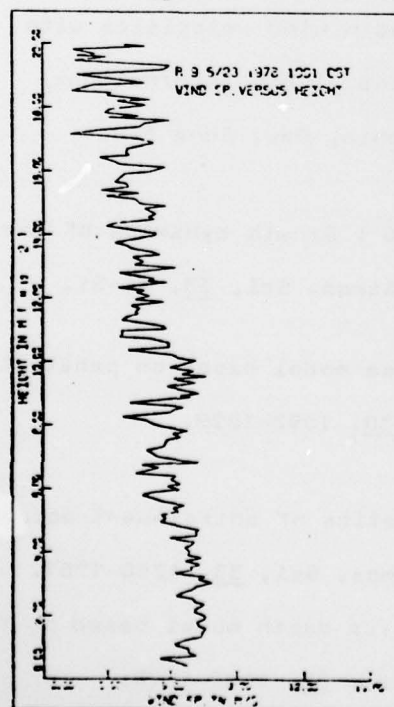
906 CST





RUN 9

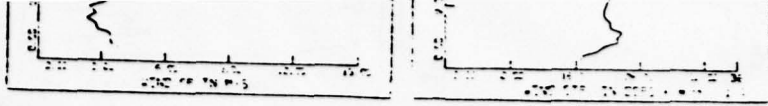
1001 CST





REFERENCES

- Frenzen, P., 1972 : Instrumentation for atmospheric boundary layer studies: the WHAT- system. Annual report for radiological and environmental research, div. ANL-7960 jan-dec 1972.
- Kato, H., and O. M. Phillips, 1969 : On the penetration of a turbulent layer into stratified fluid. J. Fluid Mech., 37, 643-655.
- Kunkel, K., E., 1978 : Measurements of the upper convective boundary layer parameters by means of lidar. Ph.D.thesis, University of Wisconsin, Madison.
- Leuthner, T.G. and E.W.Eloranta, 1977 : Remote measurements of longitudinal and cross path wind velocities with a monostatic lidar. Presented at 8th International Laser conference, Philadelphia, Pa., June 6-9.
- Mahrt, L., and D. H. Lenschow, 1976 : Growth dynamics of the convective mixed layer. J. Atmos. Sci, 33, 41-51.
- Stull, R., B., 1973 : Inversion-rise model based on penetrative convection. J. Atmos. Sci, 30, 1092-1099.
- Stull, R., B., 1976 : The energetics of entrainment across a density interface. J. Atmos. Sci, 33, 1260-1267.
- Stull, R., B., 1976 : Mixed- layer depth model based on turbulent energetics. J. atmos. Sci., 33, 1268-1278.



Tennekes, H., 1970 : Free convection in the turbulent Ekman layer
of the atmosphere. J. Atmos. Sci., 27, 1027-1034.

Tennekes, H., 1973 : A model for the dynamics of the inversion above
a convective boundary layer. J. Atmos. Sci., 30, 558-567.

Willis, G., E., and J. W. Deardorff, 1974 : A laboratory model
of the unstable planetary boundary layer. J. Atmos. Sci. ,
31, 1297-1307.

Zeman, O., 1975 : The dynamics of entrainment in the planetary
boundary layer: a study in turbulence modeling and
parameterization. Ph. D. thesis, the Pennsylvania State
University.

Zeman, O., and H. Tennekes, 1977 : Parameterization of the
turbulent energy budget at the top of the daytime
atmospheric boundary layer. J. Atmos. Sci., 34, 111-123.

Zilitinkevich, S., S., 1975 : Comments on a paper by H. Tennekes.
J. atmos. Sci., 32, 991-992.